12-2014

Toward Understanding the Thermodynamics and Mechanisms of Actinide Sorption Reactions

Shanna Estes
Clemson University, sestes@g.clemson.edu

Toward Understanding the Thermodynamics and Mechanisms of Actinide Sorption Reactions

---

A Dissertation
Presented to
the Graduate School of
Clemson University

In Partial Fulfillment
of the Requirements for the Degree
Doctor of Philosophy
Environmental Engineering and Science

---

by
Shanna L. Estes
December 2014

Accepted by:
Dr. Brian A. Powell, Committee Chair
Dr. Yuji Arai
Dr. Timothy A. DeVol
Dr. Mark A. Schlautman
Dr. Lindsay Shuller-Nickles

Abstract

The environmental fate of actinides is greatly influenced by interfacial reactions, including sorption onto solid surfaces. Because changes in the primary hydration sphere of the actinide are expected to greatly influence the thermodynamics (i.e., reaction enthalpy and entropy) of these reactions, examining actinide sorption thermodynamics may provide insight into actinide sorption mechanisms. Additionally, examining actinide sorption thermodynamics may enhance the ability to model or predict these reactions in environmental or engineered systems where variable or elevated temperatures are expected. However, few researchers have studied actinide sorption thermodynamics. Therefore, this research examined the thermodynamics of Eu(III) (a trivalent actinide analog), Th(IV), Np(V), U(VI), and Pu(IV) sorption onto hematite ($\alpha-Fe_2O_3$) using a combination of macroscopic techniques, including multiple-temperature batch sorption experiments, surface complexation modeling, and isothermal titration calorimetry (ITC).

Batch sorption data collected at 15, 25, 35, and 50 ℃ (and 65 or 80 ℃ in some experiments) at I = 0.01 M NaCl indicate that sorption of both Eu(III) and U(VI) increases with increasing temperature. Np(V) and Th(IV) sorption onto hematite was independent of temperature. Pu(IV) sorption onto hematite appeared to increase with increasing temperature, but significant changes in Pu oxidation state during the experiments complicated interpretation of the data. The diffuse layer model (DLM) was employed for all batch sorption data. Modeling results suggested that both Eu(III) and U(VI) form bidentate inner-sphere surface complexes, in agreement with data from extended X-ray absorption fine structure (EXAFS) spectroscopy either collected in this work (for Eu(III)) or referenced from available literature. Surface complexation modeling of the Np(V) and Th(IV) sorption edge data suggested the preferential formation of monodentate surface complexes, which was in disagreement with the speciation suggested from referenced EXAFS and Fourier-transform infrared (FT–IR) spectroscopies. For Eu(III) sorption onto hematite, a van't Hoff analysis indicated

that the reaction enthalpy and entropy for the formation of $(\equiv \mathrm{FeO})_2\mathrm{Eu}^+$ (the best fit surface complex) were 131 ± 8 kJ mol^{-1} and 439 ± 26 J K^{-1} mol^{-1}, respectively; the sorption enthalpy determined from ITC experiments was in excellent agreement. For U(VI) sorption onto hematite, several surface complexes were proposed from the surface complexation modeling results, depending on reaction temperature. However, the reaction enthalpy and entropy for the formation of $(\equiv \mathrm{FeOH})_2\mathrm{UO}_2^{2+}$ were less than the enthalpy and entropy determined for the Eu(III)-hematite complex. These results, in combination with collected and referenced EXAFS data that suggest a greater U−Fe distance compared with Eu−Fe, support that the interaction between U(VI) and the hematite surface is thermodynamically weaker than the interaction between Eu(III) and the hematite surface. The enthalpies approximated for Np(V) and Th(IV) sorption onto hematite were ≈ 0 kJ mol^{-1}, possibly indicating the formation of a combination of outer- and inner-sphere complexes on the hematite surface. This work presents the first systematic study on the thermodynamics of actinide sorption reactions, and provides the framework needed to understand the thermodynamics and mechanisms of actinide sorption onto other minerals, soils, or sediments under other experimental conditions.

Dedication

To Kiona, who finally found her groove

Acknowledgments

Thinking back to my teenage years, I never imagined that my educational path would lead me here . . . to this point where I have the privilege of investigating the chemistry of the most unique elements on the periodic table in the most complex system imaginable – the environment. Although many, many individuals have inspired, guided, and challenged me along this path, I must first thank my advisor, Dr. Brian Powell, who has given me innumerable opportunities to explore actinide chemistry using new and fascinating techniques, to visit new locations around the globe, and to meet fellow actinide scientists. Without him, I would not have acquired as much knowledge or experience over the past three and a half years, nor would I have had as much fun. I am also especially grateful to each of my committee members, Dr. Yuji Arai, Dr. Tim DeVol, Dr. Mark Schlautman, and Dr. Lindsay Shuller-Nickles, for inspiring me, for giving me new perspective, and for giving me confidence that I have "the right stuff" to pursue this career further. I must especially thank Dr. Yuji Arai for the many, many interesting, thought-provoking, and, often times, entertaining conversations.

I also give special thanks to: Dr. Elizabeth Carraway for her guidance, support, and friendship, and for helping me find this path; Dr. Cindy Lee for introducing me to environmental chemistry, and for re-igniting my passion for chemistry; and Dr. Julia Brumaghim for teaching me many things about being a great teacher, and for also re-igniting my passion for chemistry. I am also thankful to all current and past group members, particularly Dr. Amy Hixon, Hilary Emerson, and Jerry Mangold, for many, many helpful and entertaining conversations, and for helping me survive this past summer.

I am most grateful to: my parents, Tim and Cindy Hackett, for always supporting and loving me; my sister, Brianne Hackett, and my brother, Jesse Hackett, for always making me smile; and my bestie, Brittanie Young, for being herself, and for always being there for me, no matter what the rain may bring. And, of course, I would not be writing this without patience and infinite love

from my husband, Jason Estes – without him, I curse the sky; with him, I shine.

I also thank the Roy G. Post Foundation and the Health Physics Society for a scholarship and fellowship, respectively, which helped me to achieve my educational goals. This research was supported by the U.S. Department of Energy Office of Biological and Environmental Research through the Nuclear Energy University Partnership Program (project number 11-3180) and the Subsurface Biogeochemical Research Program (project number DE-SC0004883). Additionally, MRCAT operations are supported by the US Department of Energy and the MRCAT member institutions.

Table of Contents

List of Tables

List of Figures

Chapter 1

Introduction

Actinide chemistry in the environment is primarily controlled by four chemical processes: (1) oxidation and reduction, (2) hydrolysis and ligand complexation, (3) precipitation and dissolution, and (4) sorption* and desorption. To understand and to possibly predict the fate and transport of actinides in the environment, each of the above processes must be thoroughly investigated over a wide range of chemical conditions simulating those expected in natural systems. However, despite decades of research exploring the chemistry of actinides, many questions remain regarding this chemistry in the environment, particularly with respect to actinide sorption and desorption processes. For example, Kersting et al. and Novikov et al. recently linked kilometer-scale subsurface plutonium transport at the U.S. Nevada Test Site[1] and the Russian Mayak Production Association[2] with irreversible plutonium sorption onto mobile colloids. This observation contradicts the previously held notion that plutonium is relatively immobile in the environment; additionally, it suggests that desorption of plutonium may be thermodynamically or kinetically hindered.

Understanding actinide sorption thermodynamics may provide insight into the transport phenomenon described above. For example, after developing a multi-temperature surface complexation model (SCM), Almazan-Torres et al.[3] used the van't Hoff relationship to estimate the enthalpy ($\Delta_r H$) and entropy ($\Delta_r S$) of uranium adsorption onto zirconium oxophosphate. They determined that both $\Delta_r H$ and $\Delta_r S$ were positive, indicating that uranium adsorption onto zirconium oxophosphate is an entropically driven reaction.[3] Furthermore, they suggested that the positive entropy term

*Throughout this document, the term *sorption* is used to describe general actinide partitioning to a solid phase, while the term *adsorption* is used specifically in reference to the formation of either inner- or outer-sphere actinide surface complexes.

was associated with the displacement of coordinating water molecules from the uranium primary hydration sphere during inner-sphere adsorption. This type of reaction mechanism could hinder actinide desorption from mineral surfaces, and may help to explain the long-distance plutonium transport observed by Kersting et al.[1] and Novikov et al.[2] However, actinide sorption thermodynamics or sorption induced changes in the actinide primary hydration sphere have not been investigated.

Therefore, this work investigated actinide sorption thermodynamics and mechanisms. Specifically, the effect of temperature on Eu(III) (as an analog for trivalent actinides), Th(IV), Np(V), U(VI), and Pu(IV) sorption onto the iron oxide mineral hematite ($\alpha-Fe_2O_3$) was examined. Similar to the work of Almazan-Torres et al.,[3] surface complexation modeling and the van't Hoff relationship were used to estimate the enthalpy and entropy of actinide sorption onto hematite. To support this, data derived from extended X-ray absorption fine structure (EXAFS) spectroscopy and other spectroscopic techniques (e.g., time-resolved laser induced fluorescence spectroscopy (TRLFS)), either from the literature or measured directly, were used to infer changes in the actinide primary hydration sphere during sorption. Additionally, isothermal titration calorimetry (ITC), was used to directly measure the reaction enthalpy for both Eu(III) and U(VI) sorption onto hematite. The results greatly expand the scientific community's knowledge of actinide chemistry at the solid-water interface.

Chapter 2

Background

2.1 Actinides in the Environment

Actinides are present in the environment as anthropogenic contamination and as naturally occurring mineral deposits. Decades of radionuclide research and production, uranium mining and milling, nuclear weapons manufacturing and testing, and the inadequate disposal practices associated with these activities have resulted in widespread environmental contamination. More than 50% of legacy U.S. Department of Energy (DOE) facilities have radionuclide contaminated soils, sediments, and groundwater.[4] Other countries with current or former nuclear energy or nuclear weapons programs (e.g., France, Germany, the former Soviet Union, the United Kingdom, etc.) also have significant contamination.[5–8] In a 1995 review, Lieser identified numerous radionuclides of importance in the environment, including Eu-155,156, Th-227,229,230,232, Pa-231,233, U-233,234,236,238, Np-236,237, Pu-239,241, Am-241,243, and many others.[6] Of these, plutonium and uranium are of particular concern at legacy DOE facilities, where soil and sediment concentrations can exceed 1×10^6 pCi kg^{-1}.[4]

Of the naturally occurring actinides, both thorium and uranium exist in the Earth's crust in significant concentrations (9.6 mg kg^{-1} and 2.7 mg kg^{-1}, respectively),[9] and weathering processes can result in the contamination of ground or surface water. Thorium generally remains immobilized in the environment due to its low aqueous solubility as Th(IV). However, in slightly oxidizing aqueous environments, dissolution of the highly mobile uranyl ion, UO_2^{2+}, from uranium rich deposits can lead to aqueous concentrations exceeding regulatory limits. For example, some private wells in upstate South Carolina have measured aqueous uranium concentrations exceeding ~3,300 pCi L^{-1}.[10]

Additionally, in certain areas of Finland, oxidative dissolution from surrounding granitoid bedrock has resulted in high uranium groundwater concentrations, sometimes exceeding 7,900 pCi L^{-1}.*[11,12]

The presence of actinides in the environment represents a significant risk to human health due to the inherent radio- and chemical toxicity of these elements. Although the majority of U.S. actinide contamination is currently contained within the boundaries of government owned land, there is concern that these elements will migrate through the environment, thereby increasing the risk of human exposure. Understanding the chemistry of actinides in the natural environment, particularly understanding the chemical processes that may immobilize actinides in the environment, is therefore important for predicting and perhaps eliminating environmental actinide migration which will decrease the potential for human actinide exposure.

2.2 Environmental Actinide Chemistry

Although environmental actinide transport can occur by a variety of mechanisms (e.g., atmospheric advection and diffusion, physical dispersion, etc.), transport is most typically associated with the movement of ionic or colloid-sized species within ground or surface water. To understand and possibly predict this transport, a working knowledge of the conditions expected in natural aqueous systems and of the four processes dominating environmental actinide chemistry – (1) oxidation and reduction, (2) hydrolysis and ligand complexation, (3) precipitation and dissolution, and (4) sorption and desorption – is necessary. Each of these processes will be briefly discussed in the following sections merely to provide a basis for the proposed research. The reader is referred to several excellent reviews for additional information.[13–17]

2.2.1 Oxidation and Reduction

Actinides can exist with oxidation states ranging from +3 to +6 in natural systems. The light actinides (Th, Pa, U, Np, and Pu) exhibit the most variation in oxidation state due to the presence of delocalized f-electrons in their valence shells. It is this characteristic that makes the chemistry of light actinides so complex. The remaining actinides exhibit chemistry more similar to the lanthanide elements, and typically are only present in natural systems as trivalent cations. The range of possible

*Aqueous uranium concentrations in upstate S.C. and Finland converted from μg L^{-1} to pCi L^{-1} assuming natural isotopic abundance for uranium (99.275% ^{238}U, 0.720% ^{235}U, 0.005% ^{234}U). Reported concentrations exceeded $\sim 5,000$ μg L^{-1} in S.C.[10] and 12,000 μg L^{-1} in Finland.[11,12]

oxidation states and the oxidation state most common in natural systems for each of the light actinides is given in Table 2.1.

Table 2.1: Light actinide oxidation states.[a]

Atomic #	90	91	92	93	94
Element	Th	Pa	U	Np	Pu
Oxidation States[b]					
	(+3)	(+3)	+3	+3	+3
	+4	+4	+4	+4	**+4**
		+5	+5	**+5**	+5
			+6	+6	+6
				+7	+7

[a] Adapted from Silva and Nitsche.[14]
[b] **bold** = most dominant ox. state in natural systems; ( ) = unstable.

The redox chemistry of plutonium is particularly complex. Under certain conditions, plutonium can exist in three or four oxidation states simultaneously.[15,16] This is illustrated in Fig. 2.1 as triple points (red dots), where three oxidation states of plutonium are in equilibrium. This is also evident from the reduction potentials given in Table 2.2, which suggest that under acidic conditions, Pu(III), Pu(IV), Pu(V), and Pu(VI) may co-exist. Also from Table 2.2, it is apparent that although the co-presence of Pu(III) is possible at low pH, Pu(III) is less favorable at higher pH values as evident by the negative reduction potentials. Pu redox chemistry is even further complicated by the possibility of disproportionation reactions (given as Eqs. 2.1 and 2.2) and α-particle induced oxidation or reduction.[16] However, these reactions are typically only important when aqueous plutonium concentrations exceed $\sim 10^{-6}$ M,[16] which is unlikely, even in contaminated environments.[1,18]

$$3Pu^{4+} + 2H_2O \rightleftharpoons 2Pu^{3+} + PuO_2^{2+} + 4H^+ \tag{2.1}$$

$$2PuO_2^+ + 4H^+ \rightleftharpoons Pu^{4+} + PuO_2^{2+} + 2H_2O \tag{2.2}$$

Because plutonium redox chemistry is so complex, experiments hoping to elucidate specific reaction mechanisms are quite difficult. For this reason, many scientist's choose to use analogs that are chemically similar to plutonium, but are much less redox sensitive. Although thorium, uranium, and neptunium can exist in multiple oxidation states, these elements are generally more difficult to oxidize or reduce, and therefore exist primarily as Th(IV), Np(V), and U(VI), which are commonly used as analogs for Pu(IV), Pu(V), and Pu(VI), respectively.[17] Eu(III) is often used as an analog

for Pu(III) and other trivalent actinides.[17]

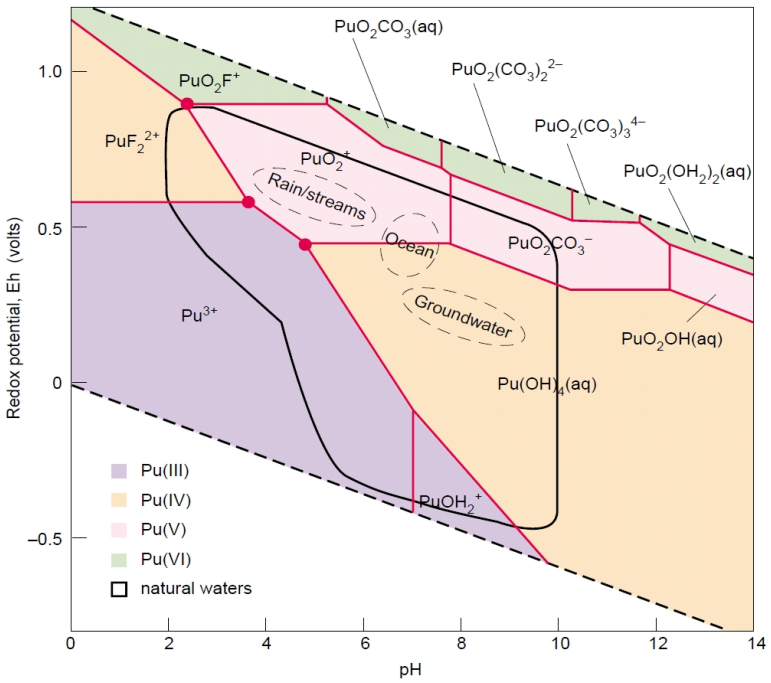

Figure 2.1: Pourbaix diagram for plutonium, modeled in the presence of carbonate and fluoride. The red dots indicate triple points where three plutonium oxidation states can co-exist. The solid black outline denotes Eh-pH values found in natural systems, and the dashed ovals denote Eh-pH ranges common to rainwater, groundwater, and seawater. Adopted from Runde.[15]

2.2.2 Hydrolysis and Ligand Complexation

Actinides exist in water as hydrated ions (i.e., $An(H_2O)_x^{n+}$), where the oxidation state of the actinide determines the number and geometry of coordinating water molecules. The high charge of pentavalent and hexavalent actinides results in immediate hydrolysis in water to give trans dioxo cations. As representative of the different hydrated actinide ions, the molecular structures for the plutonium aqua ions are shown in Fig. 2.2. It should be noted that aqueous An−O coordination numbers measured for An(III) and An(IV) cations have ranged from 8 to 10 and 8 to 12, respectively.[16]

The actinide aqua ions are subject to both hydrolysis and complexation with other species prevalent in natural aqueous systems. Hydrolysis occurs with the loss of one or more protons from

Table 2.2: Reduction potentials for plutonium at pH 0, 8, and 14 versus the standard hydrogen electrode (SHE).[a]

Reduction Reaction	pH 0	pH 8[b]	pH 14[c]
$Pu^{4+} + e^- \rightleftharpoons Pu^{3+}$	+0.982	−0.39	−0.96
$PuO_2^+ + 4H^+ + e^- \rightleftharpoons Pu^{4+} + 2H_2O$	+1.170	+0.70	−0.67
$PuO_2^{2+} + e^- \rightleftharpoons PuO_2^+$	+0.913	+0.60	+0.12
$PuO_2^{2+} + 4H^+ + 2e^- \rightleftharpoons Pu^{4+} + 2H_2O$	+1.043	+0.65	+0.34
$PuO_4(OH)_2^{3-} + 2H_2O + e^- \rightleftharpoons PuO_2(OH)_4^{2-} + 2OH^-$	—	—	+0.85

[a] Adapted from *The Chemistry of the Actinide and Transactinide Elements*.[16]
[b] Estimated by Allard et al.[19]
[c] 1 M NaOH, Peretrukhin et al.[20]

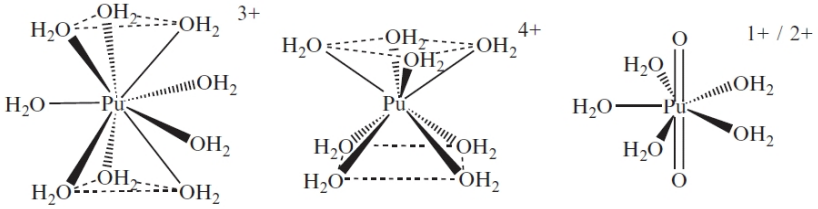

Figure 2.2: Molecular structure of the plutonium aqua ions. Adopted from Morss et al.[16]

the actinide primary hydration sphere via the reaction,

$$An(H_2O)_x^{n+} \rightleftharpoons An(OH)_y(H_2O)_{x-y}^{n-y} + yH^+. \tag{2.3}$$

As a result, a distribution of actinide hydrolysis products is expected with increasing pH as illustrated in Fig. 2.3. The extent of hydrolysis at any particular pH is dependent on the acidity of the actinide cation. However, due to the presence of two doubly bound oxygen atoms within the coordination spheres of An(VI) and An(V) ions, the effective charge on these species is increased to ~ 3.3 and ~ 2.3, respectively.[13] Therefore, the strength of actinide hydrolysis decreases in the order

$$An^{4+} > AnO_2^{2+} \approx An^{3+} > AnO_2^+. \tag{2.4}$$

As an example of this trend, the stability constants for the first hydrolysis products of Th(IV), U(VI), Eu(III), and Np(V) are given in Table 2.3. These $\log {}^*\beta^\circ$ values decrease in order of the trend shown in Eq. 2.4, and indicate that the first hydrolysis product of Np(V) is not significantly present until above approximately pH 9. This is one reason that An(V) ions are expected to have the greatest mobility in the environment.

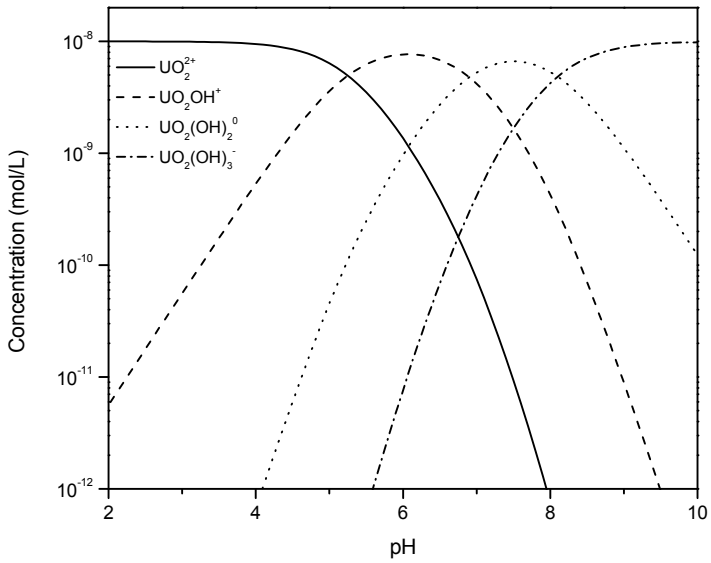

Figure 2.3: Aqueous uranium speciation over the pH range $0 - 12$ in the absence of CO_2 as modeled using Visual MINTEQ with equilibrium constants given by Guillaumont et al.[21] The total U concentration was 1×10^{-8} M and the ionic strength was fixed at 0.001 M NaCl.

The actinides also readily form complexes with various ligands common to the aqueous environment. The strength of these complexes also generally follows the trend shown in Eq. 2.4. Additionally, for a given actinide oxidation state, the complexation affinity with different inorganic ligands decreases in the order[14]

$$\mathrm{OH^-, CO_3^{2-}} > \mathrm{F^-, HPO_4^{2-}, SO_4^{2-}} > \mathrm{Cl^-, NO_3^-}. \tag{2.5}$$

Table 2.3: Representative hydrolysis constants for actinides in different oxidation states.[a]

Reaction	$\log {}^*\beta^\circ$
$\mathrm{Th^{4+} + H_2O \rightleftharpoons Th(OH)^{3+} + H^+}$	-3.20
$\mathrm{UO_2^{2+} + H_2O \rightleftharpoons UO_2(OH)^+ + H^+}$	-5.25
$\mathrm{Eu^{3+} + H_2O \rightleftharpoons Eu(OH)^{2+} + H^+}$	-7.76[b]
$\mathrm{NpO_2^+ + H_2O \rightleftharpoons NpO_2(OH)^0 + H^+}$	-8.98[c]

[a] Values from Guillaumont et al.[21]
[b] Klungness and Byrne.[22]
[c] Rao et al.[23]

Therefore, one would expect that An(IV) ions form a stronger complex with, for example, fluoride, than An(VI) ions, and that An(VI) ions form a stronger complex with carbonate than with fluoride, etc. Indeed, the equilibrium constants shown in Table 2.4 confirm the expected trend. This ability of actinides to form a wide range of aqueous complexes could potentially increase transport in systems where the environmental conditions would otherwise favor precipitation or sorption of the actinide. As an example, Zhao et al. recently investigated the effect of dissolved organic matter (DOM) on the sorption of Am(III), Pu(IV), Np(V), and U(VI) to tuff samples collected from the Nevada Test Site.[24] Their results suggested that the presence of DOM decreased americium and plutonium sorption affinities, but had little effect on the sorption affinities of neptunium and uranium.[24]

Table 2.4: Formation constants for several aqueous actinide complexes.[a]

Reaction	$\log K^\circ$
$Th^{4+} + F^- \rightleftharpoons ThF^{3+}$	8.65
$U^{4+} + F^- \rightleftharpoons UF^{3+}$	9.42
$UO_2^{2+} + F^- \rightleftharpoons UO_2F^+$	5.16
$UO_2^{2+} + CO_3^{2-} \rightleftharpoons UO_2CO_3^0$	9.94
$Np^{4+} + F^- \rightleftharpoons NpF^{3+}$	8.96
$NpO_2^{2+} + F^- \rightleftharpoons NpO_2F^+$	4.57
$NpO_2^{2+} + CO_3^{2-} \rightleftharpoons NpO_2CO_3^0$	9.32
$NpO_2^{+} + F^- \rightleftharpoons NpO_2F^0$	1.20
$Pu^{4+} + F^- \rightleftharpoons PuF^{3+}$	8.84
$PuO_2^{2+} + F^- \rightleftharpoons PuO_2F^+$	4.56
$PuO_2^{2+} + CO_3^{2-} \rightleftharpoons PuO_2CO_3^0$	9.50

[a] Values from Guillaumont et al.[21]

2.2.3 Precipitation and Dissolution

The precipitation or dissolution of actinide mineral phases can also greatly affect actinide transport in the environment. The amorphous solids, $An(OH)_x^0$ or $AnO_2(OH)_z^0$, where $x = 3$ or 4 and $z = 1$ or 2 depending on the actinide oxidation state, generally control actinide solubility. With time, precipitated actinide phases may convert to more ordered, less soluble hydroxide phases or

oxides with the stoichiometry AnO_x, where $x \geq 2$. As a general rule, An(IV) species are considerably less soluble than An(V/VI) species. This is illustrated by the uraninite ($U(IV)O_2$) and schoepite ($U(VI)O_3 \cdot H_2O$) solubility curves shown in Fig. 2.4. Therefore, it is conceivable that mechanisms which reduce An(V/VI) species to An(IV) species may result in An(IV) precipitation and, subsequently, actinide sequestration. For this reason, a considerable amount of research has been dedicated to examining both biotic and abiotic mechanisms of reduction, particularly in relation to UO_2^{2+}.[25–28] However, precipitation of solid phases may enhance transport if nanosized precipitates, which can remain suspended in water for long periods of time, are formed. This is a particular concern for plutonium, which is expected to exist in groundwater primarily as Pu(IV) (see Fig. 2.1), and which readily forms intrinsic colloids ranging in size from $1 - 100$ nm.[14,15,29]

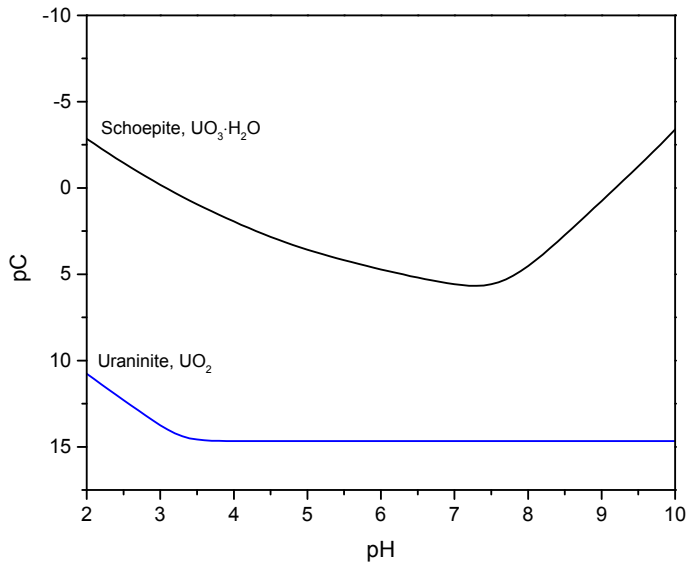

Figure 2.4: Solubility comparison between the mineral phases uraninite and schoepite in the presence of atmospheric CO_2 ($P_{CO_2} = 10^{-3.4}$ atm), as modeled using Visual MINTEQ with equilibrium constants given by Guillaumont et al.[21] The ionic strength was fixed at 0.01 M NaCl.

The precipitation of actinide solids on the surfaces of naturally occurring mineral phases also represents a potential mechanism for either retarded or enhanced environmental transport. On one hand, surface-mediated precipitation on bulk mineral phases, which are typically immobile in the environment, could limit actinide transport. However, surface-mediated precipitation on naturally occurring colloids (e.g., mineral colloids, natural organic matter), which can remain suspended in

the water column for long periods of time, could increase the potential for long-distance transport. Powell et al. recently examined plutonium colloid formation in the presence of geothite and quartz.[29] Although plutonium colloids ($\sim 2-5$ nm) were identified in association with both the goethite and quartz surfaces, the crystal structure of the precipitates associated with the goethite surface differed from the crystal structure of the intrinsic colloids (formed in the absence of additional solid phases) and the crystal structure of the precipitates associated with the quartz surface.[29] Powell et al. suggested that the presence of Pu_4O_7 on the geothite surface, rather than PuO_2, was the result of a structural alignment between the goethite and plutonium crystal faces.[29] This type of reaction could increase the ability of plutonium to migrate through the environment with goethite (or other mineral) colloids.

2.2.4 Sorption and Desorption

There are several mechanisms by which actinides can partition to solids. These include: (1) outer-sphere adsorption, (2) inner-sphere adsorption, (3) surface precipitation or colloid attachment, (4) and co-precipitation.[30] Outer-sphere adsorption should proceed without the loss of water molecules from the actinide primary hydration sphere, while inner-sphere adsorption should proceed with the loss of water,[30,31] yet this has not been extensively investigated. For actinides, the sorption mechanism can vary depending on solution conditions, actinide concentration, and the mineral phase available for partitioning. As an example, uranyl partitioning to montmorillonite, a 2-1 naturally occurring clay mineral, at low pH and low ionic strength is dominated by outer-sphere sorption.[32] However, at higher pH and ionic strength, inner-sphere surface complexes on the montmorillonite surface were identified using EXAFS spectroscopy. For metal oxide and hydroxide minerals, e.g., hematite ($\alpha-Fe_2O_3$), goethite ($\alpha-FeOOH$), gibbsite ($\gamma-Al(OH)_3$), etc., actinide sorption is dominated by inner-sphere mechanisms.[30]

Although significant progress on understanding the sorption behavior of actinides has been made in recent years, many questions remain unanswered. As an example, Pu(V) reduction to Pu(III/IV) has been observed in the presence of goethite,[33–35] magnetite,[36] hematite,[35] manganite,[37] and other non-reducing pure[38,39] and mixed[38,40] mineral phases. Five proposed mechanisms which may contribute to this reduction are: (1) dispropotionation of Pu(V), (2) reduction by trace Fe(II) (or other reduced species), (3) α radiolysis, (4) electron shuttling within semi-conducting solids, or (5) thermodynamic stability of Pu(IV). Recently, Hixon et al. investigated the interaction of

Pu with quartz using two different isotopes, ^{238}Pu and ^{242}Pu, such that the reaction systems had equal molar Pu concentrations, but different Pu radioacitivities.[41] Significant differences in total sorption or kinetics between the different reaction systems were not observed. Therefore, the results suggested that α radiolysis did not contribute to Pu(V) reduction to Pu(IV) on the quartz surface. Additionally, the use of high purity quartz decreased the potential for Pu(V) reduction by trace reductants, and eliminated the potential for Pu(V) reduction due to electron shuttling within the solid phase since quartz is not a semi-conductor. The other proposed mechanisms, disproportionation and stability of Pu(IV), need further investigation.

Decreased kinetics for actinide desorption from various pure and mixed mineral phases have also been observed. Lu et al. studied the interaction of plutonium with hematite, silica, and montmorillonite in J-13 well water from the Yucca Mountain site.[42] Although greater than 95% sorption to hematite and greater than 55% sorption to silica and montmorillonite was observed in less than 500 hours, desorption kinetics were considerably slower, and after nearly one year, less than 1% of the plutonium was removed from the hematite, and only $\sim$ 20% plutonium was removed from the silica and montmorillonite.[42] Of course, due to the likely reduction of plutonium on the hematite, silica, and montmorillonite surfaces, interpretation of this kinetic data is complicated. However, it is evident that sorption hysteresis may enhance colloid-facilitated transport of actinides and that additional research is needed to understand this behavior.

2.3 The Thermodynamics of Sorption Reactions

Understanding the thermodynamics of sorption reactions in greater detail, by defining the enthalpy and entropy of sorption reactions, may help to elucidate the mechanisms responsible for some of the observed phenomena described above – i.e., sorption/desorption hysteresis, and long-distance subsurface transport. To define enthalpy and entropy, sorption reactions need to be investigated at variable temperatures. Additionally, investigating actinide sorption thermodynamics is important because: (1) a wide range of temperatures is expected in the natural environment; and (2) elevated temperatures are expected in future subsurface nuclear waste repositories as demonstrated in Fig. 2.5 for the proposed Yucca Mountain Repository. However, few researchers have investigated the effect of temperature on actinide sorption.

To understand the thermodynamics of sorption reactions, one must also be aware that

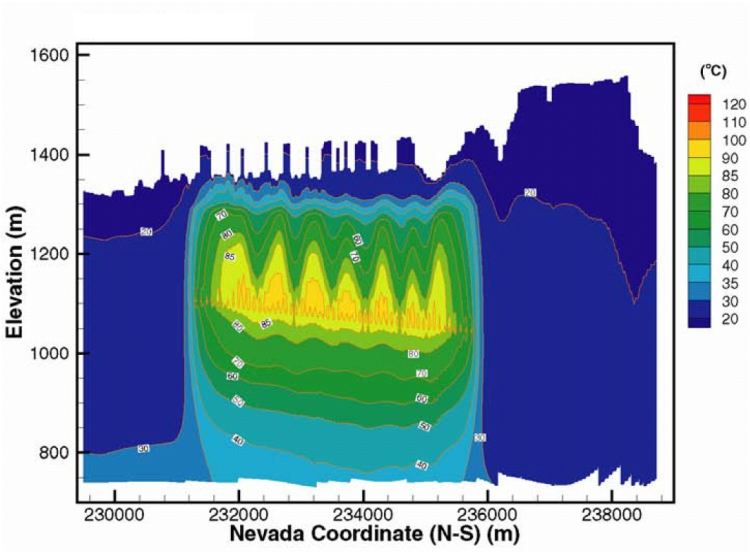

Figure 2.5: Expected temperature distribution after 1,000 years in the Yucca Mountain repository with ventilation. Adopted from the U.S. DOE Office of Civilian and Radioactive Waste Management.[43]

temperature influences all chemical reactions, and therefore, a detailed understanding of the effect of temperature on aqueous phase processes is also necessary. Fortunately, most of this data is compiled in thermodynamic databases. As an example, the expected distribution of Eu(III) aqueous complexes is shown in Fig. 2.6 from 15 to 50 °C in the absence and presence of atmospheric carbon dioxide. From Fig. 2.6, it is evident that the importance of hydrolysis products increases with increasing temperature. Similar changes in aqueous speciation are expected for the actinides with increasing temperature.

2.3.1 Theory

Choppin described the thermodynamics of aqueous actinide complexation reactions as having competing thermodynamic parameters.[13] To form an inner-sphere aqueous complex, dehydration of the actinide is necessary to allow room within the coordination environment for the complexing anion. Because dehydration results in an increase in system disorder, a positive entropy ($+\Delta S$) is expected. Additionally, because dehydration requires breaking the bond between the actinide and the water molecule, one can also expect that dehydration will be endothermic ($+\Delta H$). However, the formation of complexes between cations and anions is expected to decrease system disorder ($-\Delta S$) and be exothermic ($-\Delta H$). Ignoring the electrostatics of interfacial reactions, the same concepts can be

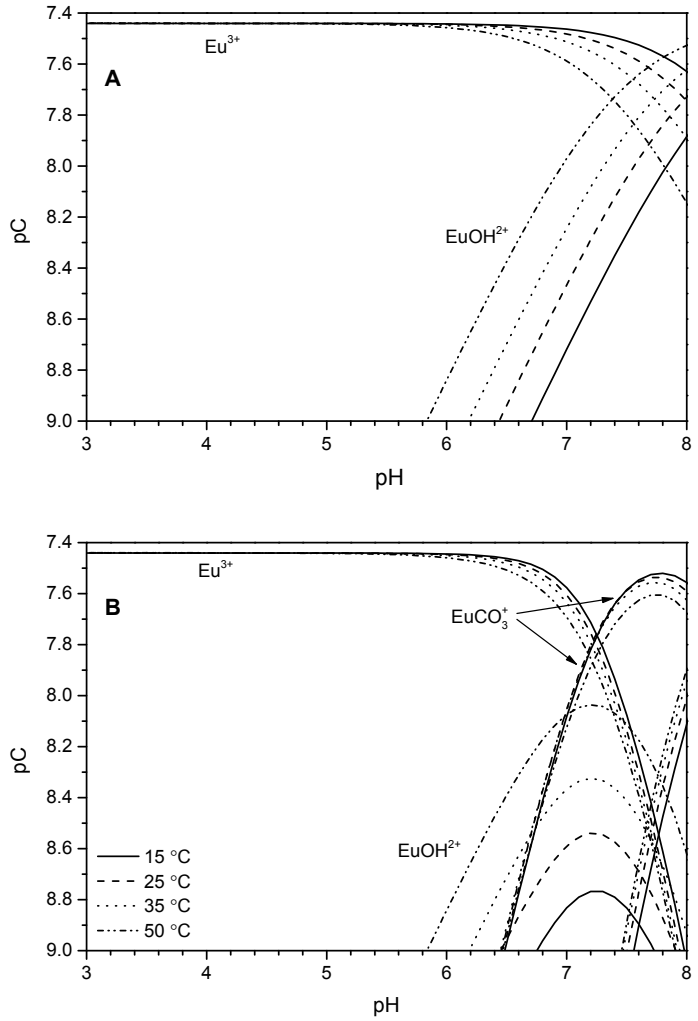

Figure 2.6: Aqueous speciation of Eu(III) in the absence (A) and presence of atmospheric CO_2 ($P_{CO_2} = 10^{-3.4}$ atm) (B) as modeled using Visual MINTEQ, with equilibrium constants given by Klungness and Byrne[22] and Luo and Byrne.[44] The modeling conditions were $[\text{Eu(III)}]_{\text{tot}} = 3.7\times10^{-8}$ M in 0.01 M NaCl. Oversaturated solids were not allowed to precipitate.

used to describe the thermodynamics of actinide surface complexation, such that

$$\begin{aligned}\Delta G &= \Delta G_{dehyd.} + \Delta G_{complex.} \\ &= \Delta H_{dehyd.} + \Delta H_{complex.} - T\Delta S_{dehyd.} - T\Delta S_{complex.}\end{aligned} \tag{2.6}$$

From Eq. 2.6, it is easy to see how measuring the enthalpy and entropy of sorption reactions can help elucidate reaction mechanisms. For example, if an inner-sphere adsorption reaction occurs, one would expect perturbation in the actinide primary hydration sphere. Therefore, the $\Delta H_{dehyd.}$ and $\Delta S_{dehyd.}$ would be > 0, with the extent of dehydration greatly affecting the overall reaction thermodynamics. If an outer-sphere sorption reaction occurs, where no perturbation of the actinide hydration sphere is expected, $\Delta H_{dehyd.}$ and $\Delta S_{dehyd.}$ should be ≈ 0. Of course, interpreting the overall reaction thermodynamics is somewhat more complicated because of the expected competition between dehydration and complexation. However, if the overall reaction enthalpy and entropy were both positive, this would suggest that dehydration of the actinide, to some degree, is occurring during sorption. Actinide sorption reactions that proceed with extensive dehydration (i.e., large entropy gains), may demonstrate decreased desorption kinetics due to the expected high activation energy required to rehydrate the actinide.

2.3.2 Observations with Metal Sorption

Although the thermodynamics of actinide sorption reactions have not been greatly studied, many researchers have investigated the sorption thermodynamics of several transition metals and lanthanides. Rodda et al. observed an increase in Zn(II) and Pb(II) adsorption onto goethite with increasing temperature.[45] By fitting their isotherm data with several different empirical models, they estimated the enthalpy and entropy of Zn(II) and Pb(II) adsorption onto goethite to range from 4 to 30 kJ mol^{-1} and -160 to $+160$ J mol^{-1} K^{-1}, respectively. However, because Rodda et al. described their data using empirical sorption models, it is difficult to discern the reaction mechanisms important for Zn(II) and Pb(II) sorption to goethite.

Angove et al. examined Co(II) and Cd(II) adsorption onto kaolinite at variable temperatures, and also observed an increase in adsorption with increasing temperature.[46] They estimated the enthalpy and entropy of adsorption to be ≈ 72 kJ mol^{-1} and 90 to 105 J mol^{-1} K^{-1}, respectively. Eu(III) sorption onto Na-montmorillonite and kaolinite[47], U(VI) adsorption onto zirconium

oxophosphate[3], and Pu(V) adsorption onto hematite, silica, and montmorillonite[42] were also reported to increase with increasing temperature. Quinn et al. also examined the sorption of yttrium and the rare earth elements on amorphous ferric hydroxide and also determined that sorption increased with increasing temperature and that the reactions were likely driven by the displacement of hydrating water from the lanthanide primary hydration sphere.[48]

2.3.3 Quantifying Sorption Enthalpy and Entropy

Two methods are available for quantifying the enthalpy and entropy of chemical reactions.[49] The first is the van't Hoff method, where the enthalpy and entropy are indirectly determined by measuring the temperature dependence of the equilibrium constant and fitting the data using the equation[49]

$$\log K = -\frac{\Delta_r H}{\ln 10 \cdot RT} + \frac{\Delta_r S}{\ln 10 \cdot R} \tag{2.7}$$

where $\log K$ is the measured equilibrium constant, $\Delta_r H$ is the reaction enthalpy, $\Delta_r S$ is the reaction entropy, R is the universal gas constant, and T is the temperature in Kelvin. The second method uses calorimetry to directly determine the reaction thermodynamics by measuring the generation or loss of heat over time.

Care must be taken when using the van't Hoff method, as it depends on the reaction enthalpy and entropy being independent of temperature, which is a rare condition. However, for a fairly narrow temperature range (e.g., $\Delta T \sim\leq 50$ ℃), the reaction enthalpy is often constant, making the van't Hoff method suitable for use under limited conditions. Yet, for these reasons, it can be beneficial to determine reaction thermodynamics directly using calorimetry.

Isothermal titration calorimetry (ITC) allows the measurement of equilibrium constants and thermodynamic constants simultaneously, provided the initial reactant concentrations are defined. For the reaction (as an example)

$$\mathrm{A} + \mathrm{B} \rightleftharpoons \mathrm{AB}$$

the simultaneous determination of $\log K_{\mathrm{AB}}$, ΔH, and ΔS is accomplished by titrating a known mass of reactant A into reactant B. The reaction enthalpy is then determined from the equation

$$Q_{c,t} = \Delta n_t \cdot \Delta H, \tag{2.8}$$

where $Q_{c,t}$ is the corrected total heat for the formation of product AB, and Δn_t is the total moles of product AB formed.[50] The equilibrium and mass balance expressions are used to calculate Δn_t. In a similar manner, Eq. 2.8 can be used to determine the enthalpy for surface complexation reactions.

As mentioned previously, the van't Hoff method has been used to determine the reaction enthalpy of uranyl adsorption onto zirconium oxophosphate,[3] europium sorption onto kaolinite and Na-montmorillonite,[47] and cadmium and cobalt sorption onto kaolinite.[46] Although few researchers have used ITC for sorption reactions, Fang et al.[51] have successfully used ITC to quantify the enthalpy and entropy of Cu(II) adsorption onto bacterial-mineral composites, suggesting that this technique could also be applied to investigate the thermodynamics of actinide sorption onto hematite.

Chapter 3

Objectives

It is evident that the fate and transport of actinides in the environment is dependent on not only aqueous phase reactions, but also on reactions at the solid-water interface. Despite numerous studies investigating actinide sorption onto various mineral phases, there are still many unanswered questions, particularly related to the mechanisms of and the effect of temperature on these reactions. For example:

(a) How does temperature affect actinide sorption onto mineral phases? (i.e., are these reactions endothermic, entropically favorable)?

(b) Does the actinide primary hydration sphere change during sorption, and if it does, how does this change affect the thermodynamics of actinide sorption reactions?

(c) Does the effect of temperature on actinide sorption follow the actinide trend, such that a larger temperature effect will be observed for An(IV) ions, etc.?

(d) Do the sorption mechanisms differ for different actinides (i.e., inner-sphere, outer-sphere surface complexation, surface precipitation, mono- or multi-dentate surface binding, etc.)?

(e) Do the commonly used Pu oxidation state analogs, Eu(III), Th(IV), Np(V), and U(VI), accurately describe the effect of temperature on Pu sorption?

In order to answer these questions, the following research objectives have been identified. The relationship between each of the objectives and the research questions identified above is given in parentheses.

1. Evaluate the effect of temperature on the sorption behavior of several actinides (Th(IV), Np(V), U(VI), Pu(IV), and Eu(III)) (a, c, d, e);

2. Use surface complexation modeling (SCM) to describe the actinide sorption behavior and to derive reaction specific equilibrium constants (c, d);

3. Derive sorption reaction enthalpies and entropies using the van't Hoff relationship (a, b, c);

4. Compare the surface complexes proposed from SCM with the results of extended X-ray absorption fine structure (EXAFS) spectroscopy and other spectroscopic techniques (either directly measured or compared with literature data), and evaluate changes in the actinide coordination environment before and after sorption (b, d);

5. Relate the thermodynamics of the sorption reactions with the coordination environments of actinides before and after sorption to elucidate possible sorption mechanisms (b, c, d);

6. Compare directly measured actinide sorption reaction enthalpies with those derived using the van't Hoff relationship (a, f).

To meet these objectives, this work was divided into four main tasks, as listed in Table 3.1. Each task represents self-contained work, which has been or will be submitted for peer-reviewed publication.

Table 3.1: Experimental Task Summaries

#	*Description* (Target Objectives)
1	*A Self-Consistent Model Describing the Thermodynamics of Eu(III) Adsorption onto Hematite* (1, 2, 3, 4, 5)
2	*Calorimetric Determination of the Enthalpy of Eu(III) Sorption onto Hematite* (3, 6)
3	*The Thermodynamics of U(VI) Sorption onto Hematite* (1, 2, 3, 4, 5, 6)
4	*A Comparison of the Thermodynamics of Np(V), Th(IV), and Pu(IV) Sorption onto Hematite* (1, 2, 3, 4, 5)

Chapter 4

A Self–Consistent Model Describing the Thermodynamics of Eu(III) Adsorption onto Hematite*

Abstract

The environmental fate of actinides is greatly influenced by interfacial reactions, including adsorption onto solid surfaces where the adsorption of trivalent and tetravalent actinides is generally a very strong and potentially irreversible reaction. Changes in the primary hydration sphere of the actinide during inner-sphere adsorption could greatly influence the thermodynamics of these reactions. However, few researchers have studied actinide adsorption thermodynamics. Therefore, using Eu(III) as an analog for trivalent actinides, we examined the thermodynamics of Eu(III) adsorption onto

*The contents of this chapter are reproduced from: Estes, S. L.; Arai, Y; Becker, U.; Fernando, S.; Yuan, K.; Ewing, R. C.; Zhang, J.; Shibata, T.; and Powell, B. A. *Geochim. Cosmochim. Acta*, **2013**, *122*, 430–447. Note that all computational modeling portions of the published manuscript are excluded because they do not represent the intellectual work of Shanna L. Estes. Individual authors contributed the following to the published manuscript: (1) Shanna L. Estes performed all batch sorption experiments and associated data analyses, prepared all EXAFS samples with assistance from Yuji Arai and Brian A. Powell, wrote the complete manuscript, except where noted here, and completed the majority of journal requested revisions; (2) Yuji Arai assisted with EXAFS sample preparation, collected EXAFS spectra, completed all EXAFS fitting and analyses, wrote the EXAFS methods section, and reviewed the manuscript; (3) Udo Becker, Sandra Fernando, and Ke Yuan completed the computational modeling, wrote the computational methods and modeling sections, reviewed the manuscript, and completed minor journal requested revisions; (4) Rodney C. Ewing reviewed the manuscript; (5) Jiaming Zhang performed all TEM analyses and reviewed the mansucript; (6) Tomohiro Shibata collected EXAFS spectra and reviewed the manuscript; (7) Brian A. Powell developed the original research hypotheses and secured research funding, assisted with all data analyses, reviewed the manuscript, and completed minor journal revisions.

hematite, with particular emphasis on changes in the Eu(III) coordination number and the influence of temperature upon sorption. Our working hypothesis was that a decrease in hydration number upon adsorption, as indicated by a decrease in coordination number and an increase in adsorption with increasing temperature, results in energetically favorable sorption reactions, which are driven by a large, positive entropy term. To perform these studies, we applied the diffuse layer model to describe Eu(III) adsorption onto hematite at pH values ranging from $\sim$ 3 to 7 and at 15, 25, 35, and 50 ℃. Additionally, we characterized the Eu(III)-hematite surface complex and changes in the Eu(III) primary hydration sphere using extended X-ray absorption fine structure spectroscopy (EXAFS) and computational modeling. High-resolution transmission electron microscopy (HRTEM) was used to identify possible europium surface precipitates or morphological changes in the hematite. The data indicate that the adsorption reaction (1) is endothermic, (2) proceeds with a decrease in the Eu(III) coordination number, and (3) results in the formation of a bidentate mononuclear surface complex, $(\equiv FeO)_2Eu^+$. The enthalpy and entropy values for the formation of this surface complex, which were estimated using a van't Hoff plot, were 131 ± 8 kJ mol^{-1} and 439 ± 26 J K^{-1} mol^{-1}, respectively, indicating that adsorption of Eu(III) onto hematite is entropically driven. Additionally, we suggest that the decrease in Eu(III) coordination number and the large entropy term are due to the loss of coordinating water molecules from the Eu(III) hydration sphere.

4.1 Introduction

Chemistry at the solid-water interface plays an important role in the environmental fate and transport of actinides. However, despite numerous investigations describing the adsorption of plutonium and other actinides onto various clay, iron, titanium, and other minerals (reviewed in Geckeis et al.[30]), many questions remain regarding actinide interfacial chemistry in the environment. For example, kilometer-scale transport of plutonium in the subsurface at the U.S. Nevada Test Site[1] and the Russian Mayak Production Association[2] has been linked to the irreversible adsorption of plutonium onto mobile colloids, despite competing chemical processes (e.g., adsorption to bulk immobile mineral phases, precipitation). Although many studies have demonstrated that this strong and possibly irreversible adsorption may result from the stabilization of Pu(IV) surface species formed via reduction of Pu(V),[33–36,38,52,53] the mechanism or mechanisms driving this reduction have not yet been identified.

Investigating the thermodynamics of actinide adsorption reactions, with particular emphasis on the entropy and enthalpy of these reactions, may provide insight into the mechanisms driving the phenomena described above; yet, only a few researchers have probed this topic. Almazan-Torres et al. used multiple techniques to examine uranium adsorption onto zirconium oxophosphate, including variable–temperature studies which indicated that uranium adsorption increased with increasing temperature.[3] Other researchers have observed a similar relationship with temperature for transition metal ion adsorption onto goethite[45] and kaolinite,[46] and for europium adsorption onto clay minerals.[47,54] Almazan-Torres et al. also used equilibrium constants derived from surface complexation modeling (SCM) and the van't Hoff relationship to estimate the enthalpy and entropy for uranium adsorption onto zirconium oxophosphate.[3] Their results indicated that the reaction was endothermic and had a positive entropy change. They suggested that the positive entropy change for the adsorption reaction was associated with the release of coordinating water molecules from the primary hydration sphere of the metal ion during adsorption. In other words, the positive entropy change was due to the increased disorder achieved in the system as water molecules moved from a fully coordinated state into the more disordered state of bulk water.

Changes in the primary hydration sphere of metal ions are known to occur for inner-sphere adsorption onto mineral surfaces.[31] Specifically, the release of coordinating water molecules from the hydration sphere of the metal ion is expected in order to accommodate space within the coordination shell for direct bonding to the mineral surface. The extent of water loss could greatly impact the favorability or reversibility of metal ion adsorption onto mineral surfaces, with increased water losses possibly yielding larger entropy changes. Additionally, the loss of hydrating waters from the actinide and mineral surface may provide an energetic barrier which limits plutonium desorption and may help to explain the long-distance environmental transport of plutonium observed by Kersting et al.[1] and Novikov et al.[2] However, directly observing changes in the hydration sphere of a metal ion is not possible with conventional macroscopic experimental techniques. Fortunately, extended X-ray absorption fine structure spectroscopy (EXAFS) provides a means for examining the coordination environment of an adsorbed metal ion in situ, and numerous researchers have already demonstrated success analyzing the coordination environment of actinides adsorbed onto several iron minerals.[e.g.,55–57] Additionally, advances in computational modeling make it possible to simulate actinide adsorption onto mineral surfaces, providing a means to compare theory with experiment.

Although not an actinide, we investigated the sorption behavior of Eu(III) for two reasons. First, Eu(III) is a stable oxidation state[58] analog for Pu(III) and other trivalent actinide ions (e.g., Am, Cm, and higher actinides), and as shown in Fig. 2.6, Eu(III) remains present in aqueous systems as the free hydrated ion over a broad pH and temperature range, even in the presence of atmospheric carbon dioxide. Using Eu(III) therefore provides a somewhat simplified system that is not subject to complex aqueous and redox chemistry, unlike plutonium. Second, the aqueous coordination environment of Eu(III) (i.e., the number of water molecules in the Eu(III) primary hydra-tion sphere) is well defined,[59] thereby simplifying spectroscopic data analyses, and allowing us to more accurately examine changes in the europium coordination environment after sorption.

The objectives of this study were to investigate the thermodynamics of actinide surface interactions, using complementary techniques, with specific focus on understanding changes in the hydration sphere of the actinide during adsorption. In this work, we have estimated the reaction enthalpy and entropy of Eu(III) adsorption onto hematite. Furthermore, by combining SCM, EXAFS, computational modeling, and electron microscopy, we have successfully developed a robust and self-consistent description of the Eu(III)–hematite surface complex. The combined data suggest that Eu(III) adsorption onto hematite results in the formation of a bidentate mononuclear inner-sphere surface complex, and that the adsorption reaction is thermodynamically favorable due to a large positive entropy change, which we propose is due to the loss of coordinating water from the Eu(III) primary hydration sphere during adsorption.

4.2 Experimental Methods

4.2.1 Chemicals

Europium working solutions and calibration standards were prepared in 2% HNO_3 by diluting a plasma standard (1,000 μg mL^{-1} in 2% HNO_3, High Purity Standards). Europium oxide (99%, Alfa Aesar), iron(III) nitrate nonahydrate (98–101%, Alfa Aesar), nitric acid (67–70%, BDH Aristar Plus), perchloric acid (70%, EMD), potassium bicarbonate (100%, Sigma), potassium hydroxide (88.5%, J.T. Baker), sodium chloride (99%, BDH), and standardized sodium hydroxide (0.01, 0.1 N, Metrohm) and hydrochloric acid (0.01, 0.1 N, Metrohm) were used as received. Distilled de-ionized (DDI) water with resistivity >18 MΩ cm was obtained from a Millipore SuperQ water filtration system.

4.2.2 Hematite Synthesis and Characterization

Hematite ($\alpha-Fe_2O_3$) was synthesized by transformation of ferrihydrite using a method adapted from Schwertmann and Cornell.[60] In brief, 80 g of $Fe(NO_3)_3 \cdot 9H_2O$ were dissolved in 1 L of DDI H_2O at 90 ℃ and mixed with 1 L of 1 M KOH (heated to 90 ℃) in a 2 L polycarbonate bottle (PC). Then, 100 mL of 1 M $KHCO_3$ was mixed with the solution to give a pH of approximately 8. The solution was then heated to 100 ℃ in the PC bottle for 48 h to allow complete transformation to $\alpha - Fe_2O_3$. After the incubation period, the resulting bright red solid was washed with DDI H_2O six times to remove residual salts. After drying at approximately 105 ℃, the hematite was gently ground using a mortar and pestle and stored in a high-density polyethylene vial (HDPE). The synthesis yielded 16 g of $\alpha-Fe_2O_3$.

Hematite was identified as the sole product by X-ray powder diffraction using a Rigaku Ultima IV diffractometer (Cu $K_{\alpha 1}$ radiation). Surface area analysis by N_2 adsorption using a Micrometrics ASAP 2010 gave a BET surface area of 30.7 $m^2\ g^{-1}$, and transmission electron microscopy identified the material as having a rhombohedral morphology with a primary crystal size of $60 - 80$ nm.

The enthalpy of proton adsorption was determined using a "ΔT titration" as described by Fokkink et al.[61] This method requires equilibrating the mineral suspension at the point of zero charge (*pzc*), which was first determined using a mass titration.[62,63] Cristiano et al. have previously demonstrated that a mass titration yields an equivalent *pzc* as potentiometric titrations for goethite.[63] During the mass titration, weighed aliquots of hematite were added to a vacuum degassed 0.01 M NaCl solution at 25 ℃. The initial pH of the solution and the pH after equilibration with each hematite aliquot (equilibration defined as a stable pH, and generally achieved after $10-20$ min.) were recorded and plotted as a function of hematite concentration (g L^{-1}) (Fig. A.1). The mass titration was completed through a hematite concentration of ~ 7 g L^{-1}. During mass titrations, it is expected that with each addition of pure mineral, the pH will be buffered toward the mineral's *pzc*, until a constant pH (i.e., the *pzc*) is achieved. In our case, a clear plateau in the measured pH values was not observed. However, an exponential fit to the data indicated that a constant pH, or the hematite *pzc*, would be reached at ~ 7.36. From the exponential fit, we determined that a hematite concentration of 10 g L^{-1} would give a suspension pH of ~ 7.34, which is less than 0.5% different from the expected *pzc* (7.36). Therefore, 10 g L^{-1} solutions of $\alpha-Fe_2O_3$ were used for the

"ΔT titration" and the potentiometric titrations described below.

The "ΔT titration" was completed by vacuum degassing a 10 g L^{-1} solution of $\alpha-Fe_2O_3$ in 0.01 M NaCl for 30 min. The degassed hematite suspension was then equilibrated by mixing overnight under Ar flow at 15 ℃ in a water-jacketed reaction vessel. After equilibration, a combination glass body pH electrode (Metrohm) was used to record the suspension pH (i.e., *pzc*). A temperature probe was used in conjunction for automatic temperature compensation. The suspension temperature was then increased by 3 to 10 ℃, and the suspension was allowed to equilibrate before recording the new pH. An electrode potential drift equal to or less than 0.1 mV min^{-1} was defined as equilibrium. This process was repeated to obtain the *pzc* at temperatures ranging from 15 to 60 ℃. The *pzc* was then plotted as a function of inverse temperature to determine the enthalpy of proton adsorption.

After completing the temperature titration, the hematite suspension was returned to 25 ℃ and titrated using 0.1 M NaOH and 0.1 M HCl. The hematite site density and surface acidity constants at 25 ℃ were determined by fitting the potentiometeric titrations with a surface complexation model (described below). Then, the surface acidity constants at 15, 35, and 50 ℃ were calculated using the van't Hoff equation, the surface acidity constants determined for 25 ℃, and the enthalpy of proton adsorption determined from the "ΔT titration."

4.2.3 Variable-Temperature Batch Sorption

Adsorption of Eu(III) as a function of pH and temperature was studied in batch systems prepared in 50 mL polypropylene (PP) centrifuge tubes. Each tube initially contained 0.5 g L^{-1} $\alpha-Fe_2O_3$, 3.7×10^{-8} M Eu(III), and 0.01 M NaCl in DDI H_2O. The pH of the suspension in each tube was adjusted using NaOH and HCl to obtain 26 tubes with pH ranging from approximately 3 to 7.8. No additional pH adjustments were necessary after setting the initial pH.

Reaction tubes were placed horizontally within a temperature controlled orbital shaker (VWR) initially at 15 ℃. After 3 days of reaction, each tube was sampled by measuring the pH using a combination electrode with automatic temperature compensation (Thermo 9157BNMD) and by removing a 1.5 mL homogeneous aliquot. Each aliquot was centrifuged at 18,700g for 30 min to sediment particles larger than approximately 60 nm, and 1 mL of the resulting supernatant was diluted to 10 mL in 2% HNO_3. Total Eu concentrations were measured using a Thermo X Series 2 inductively-coupled plasma mass spectrometer (ICP-MS) with ^{242}Pu as the internal standard. Mea-

sured concentrations were corrected for dilution and plotted as a function of pH. After 2 to 4 additional days of reaction, the tubes were sampled a second time, as above, to confirm reaction equilibrium. If no significant difference between sorption edges measured from the first and second sampling events was observed, the reaction temperature was increased. The procedure was repeated to give data at 15, 25, 35, and 50 ℃.

4.2.4 Surface Complexation Modeling

Hematite potentiometric titrations and sorption-edge data were modeled using a modified version of the program FITEQL.[64] The FITEQL code was modified to allow: (1) a database link; (2) code stability for cases with large species matrices; and, (3) activity corrections using several ionic strength models beyond the Davies equation (although, in this work the Davies equation was used for all activity corrections). Although more sophisticated models are available (e.g., the CD-MUSIC model[65,66]), the adsorption data here were fit using the diffuse layer model (DLM),[67] which was chosen because it is effective, accurate, and simple, only requiring the hematite surface area, concentration, site density, and surface acidity constants. Additionally, using the DLM allowed us to independently build the surface complexation model in order to compare the results with those from the EXAFS and computational modeling. To determine the surface site density and surface acidity constants, the potentiometric titration data were modeled as the net proton concentration versus the logarithm of proton activity. For the sorption data, molar adsorbed Eu(III) concentrations were calculated as the difference between the initial and measured aqueous Eu(III) concentrations, and were then modeled as a function of proton activity. FITEQL was set to allow 5% relative error in all experimental data, and the ratio of the weighted sum of squares to the degrees of freedom (WSOS/DF) was used as an indication of fit quality. The Davies equation A values were adjusted for temperature according to Langmuir.[9] It should be noted that FITEQL uses the 1.0 M standard state, and equilibrium constants derived in this work are referenced to this standard state. However, to facilitate comparison between our work and the work of others, we also provided equilibrium constants referenced to both a mole fraction standard state as suggested by Wang and Giammar,[68] and the new site-occupancy standard state as suggested by Sverjensky.[69]

4.2.5 EXAFS Sample Preparation, Data Collection, and Analysis

Hematite was chosen as the solid phase because it is ubiquitous in nature and has been extensively studied.[35,52,61,70,71] Additionally, hematite is an end member iron corrosion product that is expected to occur in future repositories where nuclear waste will be stored in iron-based canisters. However, using hematite as the solid phase posed a significant challenge for our EXAFS studies. Europium L_{II}- and L_{III}-edge EXAFS measurements have been conducted on Eu(III) reacted Al- and Si-based adsorbents.[e.g.,72] However, few researchers have attempted EXAFS measurements on Eu(III) adsorbed onto iron-based solids because of the closely located Fe K and Eu L edges, which are separated by less than 200 eV, and because of the proximity of the $K_{\alpha 1}$ fluorescence line for Fe (7,112 eV) and the $L_{\alpha 1}$ fluorescence line for Eu (6,977 eV). To overcome this analytical limitation, we used Eu K-edge (48,519 eV)[73] absorption spectra to elucidate the local structural environment of Eu(III) at the hematite-water interface as a function of pH and surface coverage. Eu K-edge EXAFS spectra yield Fourier-transform data comparable to deconvoluted Eu L-edge spectra data,[74] and Eu K-edge high-energy measurements provide better EXAFS spectra quality than Eu L_{II}-edge measurements.[75]

EXAFS hematite samples were prepared in 50 mL PP centrifuge tubes and initially contained $\sim 2 \times 10^{-4}$ M Eu(III), 3.5 g L^{-1} $\alpha-Fe_2O_3$, and 0.01 M NaCl in a total volume of 40 mL. The suspension pH was adjusted using NaOH and HCl to obtain an approximate pH of 6 and 8. The final pH was measured after reaction and before recovery of the hematite. The samples were reacted for several days in equilibrium with the partial pressure of carbon dioxide in air. Using aqueous speciation calculations, the final aqueous conditions were calculated to be undersaturated with respect to amorphous $Eu(OH)_3$ for the sample at pH 6.3, but slightly oversaturated with respect to $Eu(OH)_3$ for the sample at pH 8.2. The hematite paste samples were recovered via centrifugation for 10 min at 20,190g. Total dissolved Eu concentrations in the supernatant were analyzed as above. The samples were loaded in 3 mm PC sample holders, which were then sealed with Mylar tape and wrapped with moist tissues to prevent drying prior to EXAFS data collection.

Crystalline europium oxide (Eu_2O_3), amorphous europium hydroxide ($Eu(OH)_3$), and aqueous Eu(III) were used as references for the EXAFS analysis. To prepare the aqueous Eu(III) reference sample, Eu_2O_3 was dissolved in excess perchloric acid and diluted with DDI H_2O to give a final Eu(III) concentration of $\sim$ 0.5 M at a pH of 0.2. An aliquot of this solution was shipped to the

Advanced Photon Source (APS) for analysis. The pH of the remaining solution was increased to ~ 11 using NaOH to precipitate amorphous $Eu(OH)_3$. The resulting white solid was recovered via centrifugation and loaded into a PC sample holder (as above) for EXAFS analysis.

Europium K-edge (48,519 eV) X-ray absorption spectroscopy measurements were performed at the APS 10ID MRCAT beamline. We previously conducted the measurements at 77 K to minimize thermal disorder. However, we found negligible beam-induced damage and negligible improvement in the spectra quality (i.e., no thermal disorder). Therefore, measurements reported here were conducted at room temperature. The X-ray beam reflected from the Si(333) plane of a double crystal monochromator was used and optics were set to eliminate low-energy and high-energy harmonic X-rays from the monochromator crystal. The incident beam was monitored using a nitrogen-filled ion chamber and fluorescence X-rays were measured with a Kr-filled ion chamber with Stern Heald geometry. The program FEFF 6[76] was used to estimate backscattering phases and amplitude functions of single scattering (SS) Eu−O and Eu−Eu, and multiple scattering (MS) Eu−O−O paths, which were derived from structural refinement data for Eu_2O_3.[77] The amplitude reduction factor ($S_\circ{}^2$) used was 0.57. XAS data reduction and analyses were performed using the IFEFFIT engine-based interface, SixPACK.[78] k^3-weighted Fourier-transformed EXAFS spectra were fit in R-space over the range of $0-4.5$ Å. The coordination number (CN), inter-atomic distance (R), Debye-Waller factor (σ^2) and $\Delta E_\circ$ for all samples were allowed to float and were linked to all shells during the fit unless otherwise mentioned. σ^2 of the 1st and 2nd Eu−Eu shells were fixed at 0.002 and 0.01 Å^2, respectively. To reduce the uncertainties of the fit parameters, the Best Integer Fit method was used to constrain the coordination number 6 for the Eu−O shell in crystalline Eu_2O_3 (s).

4.2.6 High–Resolution Transmission Electron Microscopy

An aliquot of each of the solid EXAFS samples prepared above was washed in DDI H_2O and then dispersed onto a lacey-carbon coated Cu TEM grid. The samples were then imaged using a high–resolution transmission electron microscope (JEOL 3011), and further analyzed by means of selected area electron diffraction, and energy-dispersive X-ray (EDX) spectroscopy.

4.3 Results and Discussion

4.3.1 Hematite Characterization

To develop the surface complexation model for Eu(III) adsorption onto hematite, it was first necessary to determine the enthalpy of proton adsorption ($\Delta_{\text{ads}}H^{\circ}_{\text{H}^+}$) for the hematite surface, which was needed to calculate the hematite surface acidity constants at each temperature. A "ΔT titration" as described by Fokkink et al.[61] was used to determine $\Delta_{\text{ads}}H^{\circ}_{\text{H}^+}$. For the "$\Delta T$ titration," the initial *pzc*, at 15 ℃, was defined as the pH of the 10 g L^{-1} hematite suspension in 0.01 M NaCl after overnight equilibration. Although surface acidity constants can be determined from potentiometric titrations at each of the experimental temperatures, we chose to use the ΔT approach because it (1) is experimentally less challenging, (2) eliminates potential artifacts which can arise from potentiometric titrations (i.e., hysteresis), and (3) provides a more accurate assessment of the *pzc* dependence on temperature.[61] Assuming no specific adsorption of background electrolyte ions, $\Delta_{\text{ads}}H^{\circ}_{\text{H}^+}$ was then derived from the equation

$$pzc = \frac{\Delta_{\text{ads}}H^{\circ}_{\text{H}^+}}{\ln 10 \cdot R} \cdot \frac{1}{T} \tag{4.1}$$

where T is the temperature in Kelvin, and R is the universal gas constant.[†61] Although Eq. 4.1 is a variant of the van't Hoff relationship, it relates the *pzc*, rather than the $\log K$ values of individual reactions, to inverse temperature. However, the enthalpy derived from Eq. 4.1 represents the enthalpy of proton adsorption for both the reaction give as K_+ and for the reverse of the reaction given as K_- (Table 4.1), with the assumption that $\Delta_{\text{ads}}H^{\circ}_{\text{H}^+}$ is equivalent for protonation of either $\equiv$FeOH or $\equiv\text{FeO}^-$, as suggested by Fokkink et al.[61] and Sverjensky and Sahai.[71] A simple derivation of Eq. 4.1 is given in Appendix A. However, we refer readers to Fokkink et al.[61] for the complete derivation of Eq. 4.1 from the Gibbs equation.

As shown in Fig. 4.1, the hematite *pzc* decreased linearly with increasing temperature. The $\Delta_{\text{ads}}H^{\circ}_{\text{H}^+}$ calculated from the slope of the linear fit was -32.2 ± 0.9 kJ mol^{-1}, which is similar to the experimentally derived values of -36.3 kJ mol^{-1} reported by Fokkink et al.[61] and -25 kJ mol^{-1} reported by Kosmulski et al.[79] Additionally, the calculated $\Delta_{\text{ads}}H^{\circ}_{\text{H}^+}$ is close to the theoretical value ($-45 \pm \sim 4 - 8$ kJ mol^{-1}) determined by Sverjensky and Sahai[71] for a single-site model (i.e.,

[†]Eq. 4.1 is the integrated form of $(\partial \text{pH}^{\circ}/\partial T)_{C_s} = \Delta_{\text{ads}}H^{\circ}_{\text{H}^+}/(2.303 \cdot RT^2)$ originally published by Fokkink et al.[61] This equation should not be directly used to calculate the *pzc* at a single temperature.

≡FeOH) using Born solvation and crystal chemical theories.

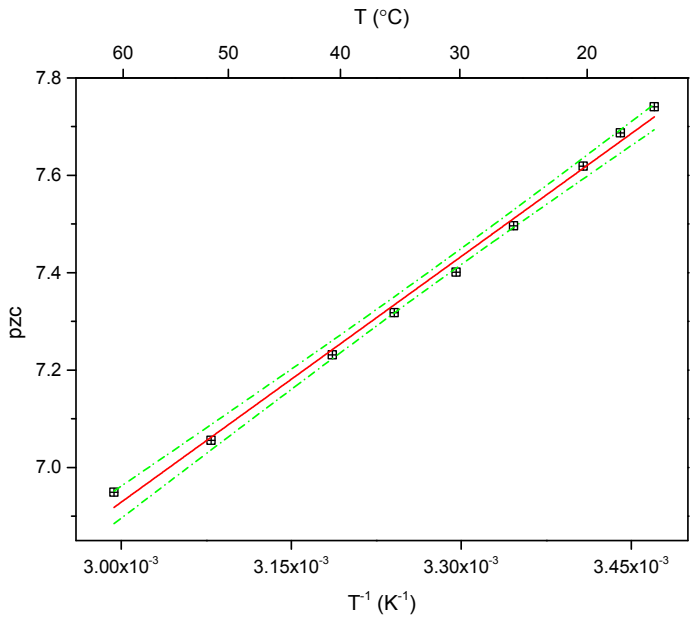

Figure 4.1: Point of zero charge as a function of temperature ("ΔT titration")[61] for a 10 g L^{-1} $\alpha-Fe_2O_3$ suspension in 0.01 M NaCl. The solid line is the linear fit with an adjusted R^2 equal to 0.994, and the dashed lines are the 95% confidence intervals.

Potentiometric titrations were performed only at 25 ℃ to determine the hematite site density and surface acidity constants, K_+ and K_-. The equilibrium expressions for surface protonation (K_+) and de-protonation (K_-) are given by

$$K_+ = \frac{[\equiv \mathrm{FeOH}_2^+]}{[\equiv \mathrm{FeOH}]\{\mathrm{H}\}^+} \cdot \exp \frac{F\psi}{RT} \tag{4.2}$$

$$K_- = \frac{[\equiv \mathrm{FeO}^-]\{\mathrm{H}\}^+}{[\equiv \mathrm{FeOH}]} \cdot \exp -\frac{F\psi}{RT} \tag{4.3}$$

where F is the Faraday constant and ψ is the surface potential. The 25 ℃ titration and resulting FITEQL model are shown in Fig. 4.2. The surface site density, $\log K_+$, and $\log K_-$ values determined from the fitting routine were 4.28 sites nm^{-2}, 6.19 $\pm$ 0.04, and -8.11 $\pm$ 0.04, respectively. The hematite *pzc* calculated from the surface acidity constants is 7.2, which is comparable to the *pzc* of 7.5 as measured at 25 ℃ during the "ΔT titration," and the *pzc* of $\sim$ 7.36 originally determined from the mass titration. Although the hematite *pzc* measured here is lower than *pzc* values commonly reported and lower than the value of 9.5 suggested by Sverjensky,[80] our *pzc* value is within the range

of $\sim 6.2 - 8.8$ given by Kosmulski[81,82] for other synthetic hematites. Furthermore, our surface site density and surface acidity constants are similar to those of Zeng et al.,[83] even though a different synthesis method was used (aerosolization of $Fe(CO)_5$). They reported a site density of 4.2 sites nm^{-2} and average surface acidity constants of approximately 6.5 and -8.9 for synthetic hematite with particle sizes ranging from 12 to 50 nm.[83] The surface acidity constants for 15, 35, and 50 ℃ were then calculated using the van't Hoff equation and the $\Delta_{ads}H^{\circ}_{H^+}$ determined above. These constants are given in Table 4.1 as $\log K$ values. The surface acidity constants referenced to the new site-occupancy standard state suggested by Sverjensky[69] are also given in Table 4.1 as $\log K^{\ddagger}$.

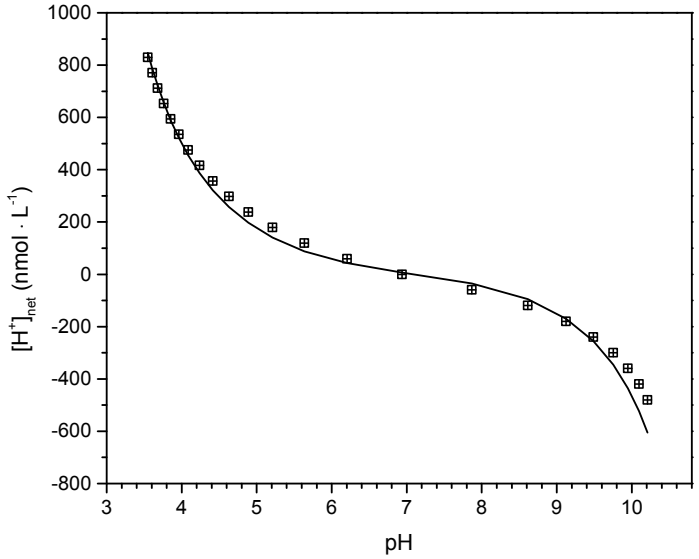

Figure 4.2: Potentiometric titration of a 10 g L^{-1} $\alpha-Fe_2O_3$ suspension in 0.01 M NaCl at 25 ℃. The solid line is the surface complexation model calculated using FITEQL.[64] The WSOS/DF for the fit was 13.2.

4.3.2 Variable-Temperature Adsorption and Surface Complexation Modeling

Europium adsorption onto hematite at 15 ℃ is shown for the first and second sampling events in Fig. 4.3. Because there was not a significant difference between the two sorption edges, we considered the Eu-hematite system at equilibrium and increased the experimental temperature to 25 ℃. Similar to the results at 15 ℃, differences between the first and second sampling events for Eu(III) adsorption onto hematite at 25, 35, and 50 ℃ were not observed (data not shown).

Rabung et al. studied the adsorption of Eu(III) onto a natural hematite (ground to give par-

Table 4.1: Equilibrium constants used for surface complexation modeling with FITEQL.

	Reaction	T ℃	$\log K$	$\log K^{\ddagger}$
K_w°	$H_2O \rightleftharpoons H^+ + OH^-$	15	-14.34^a	
		25	-13.99^a	
		35	-13.68^a	
		50	-13.26^a	
${}^*\beta_1^{\circ}$	$Eu^{3+} + H_2O \rightleftharpoons EuOH^{2+} + H^+$	15	-8.04^a	
		25	-7.76^a	
		35	-7.49^a	
		50	-7.13^a	
K_+	$\equiv FeOH + H^+ \rightleftharpoons \equiv FeOH_2^+$	15	6.39 ± 0.04^c	6.51^d
		25	6.19 ± 0.04^b	6.31^c
		35	6.01 ± 0.04^c	6.13^c
		50	5.75 ± 0.05^c	5.87^c
K_-	$\equiv FeOH \rightleftharpoons \equiv FeO^- + H^+$	15	-8.30 ± 0.04^c	-8.18^c
		25	-8.11 ± 0.04^b	-7.99^c
		35	-7.92 ± 0.04^c	-7.80^c
		50	-7.67 ± 0.05^c	-7.55^c

[a] The density of water[84] was used to calculate K_w° at each temperature according to Bandura and Lvov,[85] and the formation constant for $EuOH^{2+}$ (${}^*\beta_1^{\circ}$) was calculated according to Klungness and Byrne.[22] Note that both K_w° and ${}^*\beta_1^{\circ}$ are for $I = 0$.

[b] Surface acidity constants were determined from the potentiometric titration (Fig. 4.2) at $I = 0.01$ M, and are referenced to the 1.0 M standard state.

[c] Constants were determined from the van't Hoff equation, the enthalpy of proton adsorption (-32.2 kJ mol^{-1}), and the K_+ and K_- values derived from the 25 ℃ potentiometric titration.

[d] Equilibrium constants referenced to the site-occupancy standard state as suggested by Sverjensky[69] and calculated using the equation $K^{\ddagger} = K\frac{N_s A_s}{N^{\ddagger} A^{\ddagger}}$. N_s and A_s are the surface site density and surface area measured in this work, 4.28×10^{18} sites m^{-2} and 30.7 m^2 g^{-1}, respectively. $N^{\ddagger}$ and $A^{\ddagger}$ are the hypothetical values suggested by Sverjensky,[69] 10×10^{18} sites m^{-2} and 10 m^2 g^{-1}, respectively.

ticle sizes < 100 μm) in 0.1 M $NaClO_4$ at ambient temperature, and observed a large increase in the percent of Eu(III) adsorbed, from $\sim 0\%$ to 100%, over a narrow pH range ($1-1.5$ units).[70] Although their results are not directly comparable to our results because of many experimental differences between the two studies, a sharp increase in the fraction of Eu(III) adsorbed onto hematite over a narrow pH range was also observed in this work. This observation is common for metal sorption edge data, and has also been observed for Eu(III) adsorption onto kaolinite,[47,86] Na–montmorillonite,[47] and goethite.[87] Rabung et al.[70] also reported greater adsorption for a higher Eu to hematite site

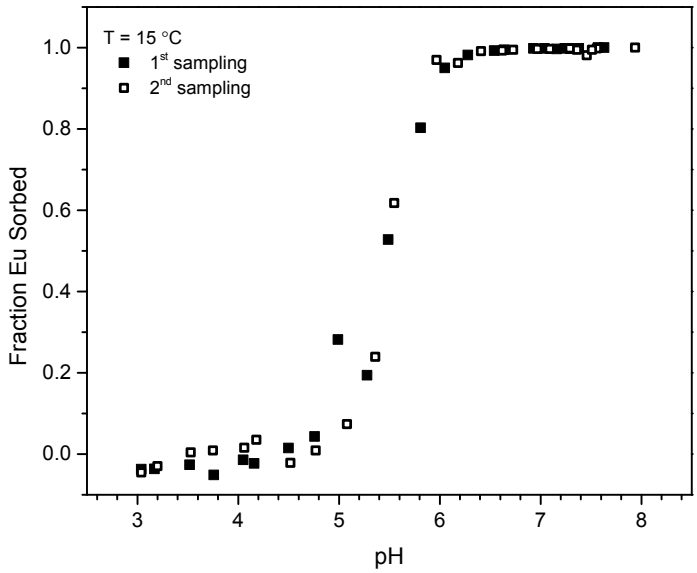

Figure 4.3: Fraction of Eu(III) adsorbed onto hematite as a function of pH at 15 ℃ for the first and second sampling events. Error bars representing $\pm$ 2σ are within each data point. No significant difference between the two sampling events was observed.

ratio than used in our experiments over the same pH range (Fig. 4.4). The observed differences between the data of Rabung et al.[70] and the current work could be due to: (1) the lower *pzc* in the Rabung et al. study (i.e., 6.0 compared to $\sim$ 7.3 in this work); (2) the higher ionic strength used by Rabung et al.; or (3) the presence of impurities in their natural hematite sample.

Eu(III) adsorption onto hematite increased with increasing temperature (Fig. 4.4), indicating that the reaction is endothermic. Our results are consistent with the observation of increasing sorption with increasing temperature that was reported for Eu(III) adsorption onto Na-montmorillonite and kaolinite.[47] Additionally, increased sorption at higher temperatures is commonly reported for other metal ions. For example, Cd(II) and Co(II) adsorption onto kaolinite,[46] Pb(II) and Zn(II) adsorption onto goethite,[45] U(VI) adsorption onto zirconium oxophosphate,[3] and Pu(V) adsorption onto hematite, silica, and montmorillonite[42] were also reported to increase with increasing temperature.

Metal surface complexation depends on both the surface properties specific to the mineral and on the aqueous chemistry of the metal ion. For these experiments, a pH range was selected to avoid the formation of Eu carbonate species, which are not expected to dominate aqueous Eu chemistry until above pH 7 as shown in Fig. 2.6. Although we included the equilibrium expression for the formation of the first Eu hydrolysis product ($EuOH^{2+}$) in the surface complexation model,

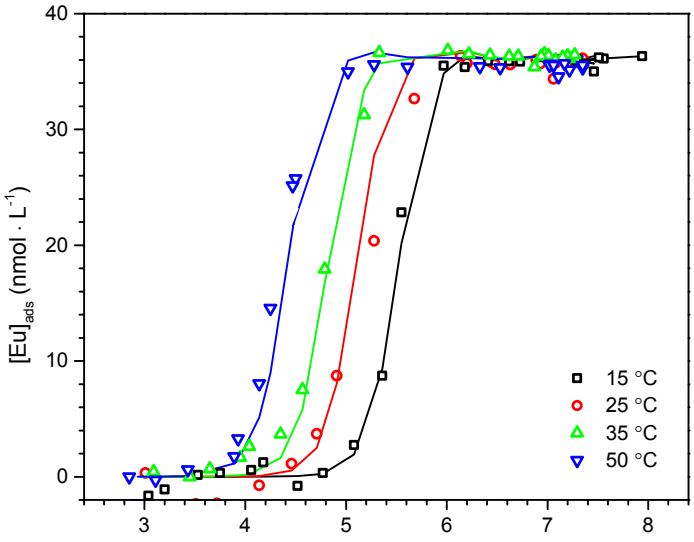

Figure 4.4: Adsorbed Eu(III) concentrations as a function of pH at 15, 25, 35, and 50 ℃, with the corresponding fits for the $(\equiv FeO)_2Eu^+$ surface complex calculated using FITEQL.[64] The WSOS/DF for each of the fits in order of increasing temperature were 109.7, 100.8, 84.7, and 50.6.

this species was also insignificant over the experimental pH range (see Fig. 2.6). Additionally, under the experimental conditions, reduction of Eu(III) to Eu(II) was not favorable,[58] and only the free hydrated Eu(III) ion was considered.

Several different surface reactions were plausible for these experimental systems. These included monodentate surface complexation with (Eq. 4.4) or without (Eq. 4.5) a single proton release, and bidentate surface complexation with (Eq. 4.6) or without (Eq. 4.7) the release of two protons. Polynuclear Eu(III) surface species were not considered due to the low aqueous europium concentrations used in our studies and, as will be discussed below, lack of Eu−Eu scattering distances in EXAFS data.

$$\equiv FeOH + Eu^{3+} \rightleftharpoons \equiv FeOEu^{2+} + H^+ \tag{4.4}$$

$$\equiv FeOH + Eu^{3+} \rightleftharpoons \equiv FeOHEu^{3+} \tag{4.5}$$

$$2 \equiv FeOH + Eu^{3+} \rightleftharpoons (\equiv FeO)_2Eu^+ + 2H^+ \tag{4.6}$$

$$2 \equiv \mathrm{FeOH} + \mathrm{Eu}^{3+} \rightleftharpoons (\equiv \mathrm{FeOH})_2\mathrm{Eu}^{3+} \tag{4.7}$$

The reaction given in Eq. 4.4 is the most prevalent in the literature, and several researchers have used a similar monodentate reaction with proton release to model Eu(III) adsorption onto kaolinite,[47,86] Na-montmorillonite,[47] natural hematite,[70] and goethite.[87] Of particular interest, Rabung et al. successfully modeled Eu(III) adsorption onto natural hematite using a monodentate surface complexation reaction (Eq. 4.4).[70] To distinguish between monodentate and bidentate surface species, Rabung et al. used a Kurbatov plot, where the slope of $\log([\mathrm{Eu}]_{\mathrm{ads}}/[\mathrm{Eu}]_{\mathrm{free}})$ vs. pH gives the number of protons released during surface complexation.[88] The Kurbatov analysis suggested that only a single proton was released during Eu(III) adsorption onto natural hematite.

To determine the surface species that best described our adsorption data, we used the equilibrium expressions given in Table 4.1 and FITEQL to model the data using each of the plausible surface reactions described above (Eqs. 4.4 – 4.7). We also attempted to model the adsorption data using variable combinations of the reactions given in Eqs. 4.4 – 4.7; however, FITEQL would not converge when using multiple surface complexation reactions due to the high degree of correlation between the reactions. Based on the WSOS/DF values, the surface species $(\equiv \mathrm{FeO})_2\mathrm{Eu}^{+}$ (Eq. 4.6), gave the best fit to our data at each temperature. As will be described in the next sections, the results of the surface complexation modeling were in excellent agreement with the bidentate mononuclear surface complex proposed from the EXAFS analysis and computational simulations. Additionally, a Kurbatov analysis for the adsorption data gave an average slope of 2.2 $\pm$ 0.1 over the temperature range studied, indicating that approximately two protons were released during Eu(III) adsorption onto hematite. The discrepancy between this work and the Rabung et al.[70] SCM is likely due to experimental differences between the two studies as stated previously. However, other reports of bidentate mononuclear surface coordination are available in the literature, e.g., U(VI) adsorption onto ferrihydrite[89] and Th(IV) adsorption onto magnetite and ferrihyrite.[90] Additionally, and more comparable to our work, Dardenne et al. observed bidentate mononuclear coordination for Lu(III) (also a rare earth element with chemistry similar to Eu(III)) adsorbed onto ferrihydrite.[91]

Eu(III) adsorption edges for 15, 25, 35, and 50 ℃ are shown in Fig. 4.4 with the resulting FITEQL models, and the equilibrium constants for the formation of $(\equiv \mathrm{FeO})_2\mathrm{Eu}^{+}$ at each temperature are given in Table 4.2 as $\log K$ values. We should note that these $\log K$ values were derived

using the following mass action expression in FITEQL:

$$K = \frac{[(\equiv \mathrm{FeO})_2\mathrm{Eu}^+][\mathrm{H}^+]^2}{[\equiv \mathrm{FeOH}]^2[\mathrm{Eu}^{3+}]} \tag{4.8}$$

Because Eq. 4.8 uses an exponent of 2 for the species $\equiv$FeOH, the $\log K$ values given in Table 4.2 are not applicable for systems with hematite concentrations other than that used in this work. Therefore, we converted our $\log K$ values to $\log K_3$ values using the equation

$$K_3 = K[\equiv \mathrm{FeOH}]_{\mathrm{tot}} = K(N^\dagger A C_s) \tag{4.9}$$

where $N^\dagger$ is the molar site density (7.11×10^{-6} mol m^{-2}), A is the specific surface area (30.7 m^2 g^{-1}), and C_s is the solid phase concentration (0.5 g L^{-1}) used in this work. K_3 is the equilibrium constant for model 3 as described by Wang and Giammar,[68] which defines the mass action expression using the mole fraction (rather than molarity) standard state with the equation

$$K_3 = \frac{([(\equiv \mathrm{FeO})_2\mathrm{Eu}^+]/[\equiv \mathrm{FeOH}]_{\mathrm{tot}})[\mathrm{H}^+]^2}{([\equiv \mathrm{FeOH}]/[\equiv \mathrm{FeOH}]_{\mathrm{tot}})^2[\mathrm{Eu}^{3+}]} \tag{4.10}$$

The $\log K_3$ values are also given in Table 4.2. Because the $\log K_3$ values are not dependent on solid phase concentration, surface area, or site density, the $\log K_3$ values can be directly input into software programs that implement the mole fraction standard state in order to model bidentate mononuclear Eu(III) surface complexation for reaction systems with other hematite properties and concentrations. However, to use the equilibrium constants determined here in software programs that use the 1.0 M standard state, e.g., FITEQL, practitioners should apply Eq. 4.9 to convert the $\log K_3$ values reported in Table 4.2 to $\log K$ values, using the molar site density ($N^\dagger$), specific surface area (A), and solid phase concentration (C_s) specific to their reaction systems. We have also reported the $\log K$ values referenced to the new site-occupancy standard state[69] in Table 4.2 as $\log K^\ddagger$.

Ridley et al. recently studied the influence of temperature on Y and Nd adsorption onto rutile.[92,93] Their initial results suggested that hydrolysis of Nd surface complexes was important at temperatures greater than 100 ℃ and at pH values greater than the pH at which complete adsorption was observed.[92] However, a more recent study using a more advanced modeling approach, suggested that hydrolysis of Y and Nd surface complexes may be important at lower temperatures and at

Table 4.2: Equilibrium constants for Eu adsorption to hematite calculated using FITEQL.

Reaction	T °C	$\log K$	$\log K_3$	$\log K^{\ddagger}$
$2 \equiv \mathrm{FeOH} + \mathrm{Eu}^{3+} \rightleftharpoons (\equiv \mathrm{FeO})_2\mathrm{Eu}^{+} + 2\mathrm{H}^{+}$	15	-0.98 ± 0.04^{a}	-4.94^{b}	18.96^{c}
	25	0.05 ± 0.04^{a}	-3.91^{b}	19.97^{c}
	35	0.71 ± 0.04^{a}	-3.25^{b}	20.65^{c}
	50	1.67 ± 0.03^{a}	-2.29^{b}	21.61^{c}

[a] The exponent for $\equiv$ FeOH was defined as 2 in both the FITEQL mass balance and mass action expressions (Eq. 4.8). Constants are for $I = 0.01$ M, and referenced to the 1.0 M standard state.
[b] Calculated using Eq. 4.9. Constants are referenced to the mole fraction standard state.
[c] Equilibrium constants referenced to the site-occupancy standard state as suggested by Sverjensky.[69] These were calculated using the equation $K^{\ddagger} = K(\frac{(N_s A_s)^2}{N^{\ddagger} A^{\ddagger}})C_s$, where C_s is the solid phase concentration used in this work, 0.5 g L^{-1}.[69] N_s and A_s are the surface site density and surface area measured in this work, 4.28×10^{18} sites m^{-2} and 30.7 m^2 g^{-1}, respectively. $N^{\ddagger}$ and $A^{\ddagger}$ are the hypothetical values suggested by Sverjensky,[69] 10×10^{18} sites m^{-2} and 10 m^2 g^{-1}, respectively.

somewhat lower pH values.[93] The reactions for Y and Nd adsorption onto rutile used by Ridley et al. do not include the release of one or more protons from the rutile surface during adsorption.[93] Instead, only reactions with hydrolyzed surface species include a net proton release. Ridley et al. previously stated that hydrolysis of an adsorbed Y atom was more probable than the release of a surface proton during Y adsorption due to increased distances between Y and surface oxygens as compared to the Y−O distance in aqueous complexes.[92] However, it is not clear that such changes in bond lengths have been experimentally observed. The reference given to Zhang et al.[94] indicates that the distance between Y and the coordinated rutile terminal oxygens (the surface site available to release a proton) is 2.4 Å, which does not seem significantly different than the 2.37 Å Y−O distance determined for aqueous complexes. Additionally, Tan et al. studied Eu(III) adsorption onto rutile using EXAFS, and determined that the Eu−O distances for the inner-sphere surface complexes were very close to those for an aqueous Eu(III) reference sample ($\sim$ 2.4 Å compared to 2.43 Å, respectively). Therefore, the hydrolysis mechanism suggested by Ridley et al.[93] may not be applicable for our study of Eu adsorption onto hematite. Without further evidence of hydrolysis, the current work maintains the working hypothesis that Eu(III) adsorbs as a free ion and that adsorption is energetically driven by the entropy associated with dehydration of the Eu^{3+} ion upon sorption.

4.3.3 EXAFS Analysis

In an effort to verify the surface complexation mechanism proposed above, we also collected Eu K-edge X-ray absorption spectra for two sorption and several reference Eu(III) samples. To achieve high quality EXAFS data, we prepared the sorption samples to yield a loading of 5,000 – 10,000 mg

of Eu(III) per kg of hematite. To do this, high concentrations of Eu(III) were added to hematite suspensions. However, because higher concentrations of Eu(III) could result in precipitation rather than adsorption, the pH of the sorption samples was set at $\sim$ 6 and 8 to bracket the pH where Eu(III) solid phases (pH $\sim$ 8) and Eu(III)-carbonate complexes become favorable (Fig. 2.6). It should be noted, however, that because the ratio $[\mathrm{Eu(III)}]_{\mathrm{tot}}/[\equiv \mathrm{FeOH}]_{\mathrm{tot}}$ is much higher for the EXAFS samples (0.3) than for the batch experiments (0.0003), the adsorption edges shown in Figs. 4.3 and 4.4 are not directly comparable to the loading levels achieved for our EXAFS studies.

The k^3-weighted EXAFS spectra and corresponding Fourier-transforms (FTs) for three reference samples, Eu_2O_3, $Eu(OH)_3$, and Eu(III) (aq), are shown in Fig. 4.5, with fitting and structural parameters for these data given in Table 4.3. The structural parameters obtained for the reference samples Eu_2O_3 and $Eu(OH)_3$ are in agreement with the literature.[72,77] For the aqueous Eu(III) reference sample, the fit indicated a coordination number (CN) and a Eu$-$O distance of 8 $\pm$ 1 and 2.20 $\pm$ 0.01 Å, respectively. Allen et al. suggested a Eu$-$O CN of 9.3 $\pm$ 0.4 and a Eu$-$O distance of 2.430 $\pm$ 0.003 Å.[95] Our values are slightly smaller than those determined by Allen et al., which might be attributed to different reaction conditions used by their and our studies (i.e., 0.25 M HCl compared to $\sim$ 0.3 M $HClO_4$, respectively). However, the CN of 8 $\pm$ 1 determined in this work for the aqueous Eu(III) sample agrees with the study conducted by Kimura and Kato,[96] who reported a decrease in the number of coordinating H_2O molecules from 9 to 8 in the lanthanide series between Eu and Tb. Additionally, an equilibrium between 8 and 9 coordinating H_2O molecules for aqueous Eu(III) has been suggested by other researchers.[59,97]

EXAFS spectra with FTs for two Eu-hematite samples and the corresponding structural parameters are also shown in Fig. 4.5 and Table 4.3, respectively. For both mineral samples, the first main peak in the FTs occurs at approximately 2 Å, which we attribute to scattering from O atoms in the first hydration sphere of the Eu complex. Note that the peaks usually appear at shorter distances than the actual bond lengths due to the phase shift of the photoelectrons. Although $Eu(CO_3)^+$ was a favorable aqueous species in the sorption sample prepared at pH 8 (Fig. 2.6), including this species in the EXAFS fitting routine did not improve the fit quality, and we conclude that Eu(III)-carbonate surface complexes were not predominant in our samples. Unlike the FTs for the reference samples Eu_2O_3 and $Eu(OH)_3$, a second scattering frequency at approximately 3.6 Å was not observed in either mineral sample, indicating the absence of neighboring Eu atoms. This suggests that Eu oxide or hydroxide precipitates are not predominant surface species in either of our sorption samples,

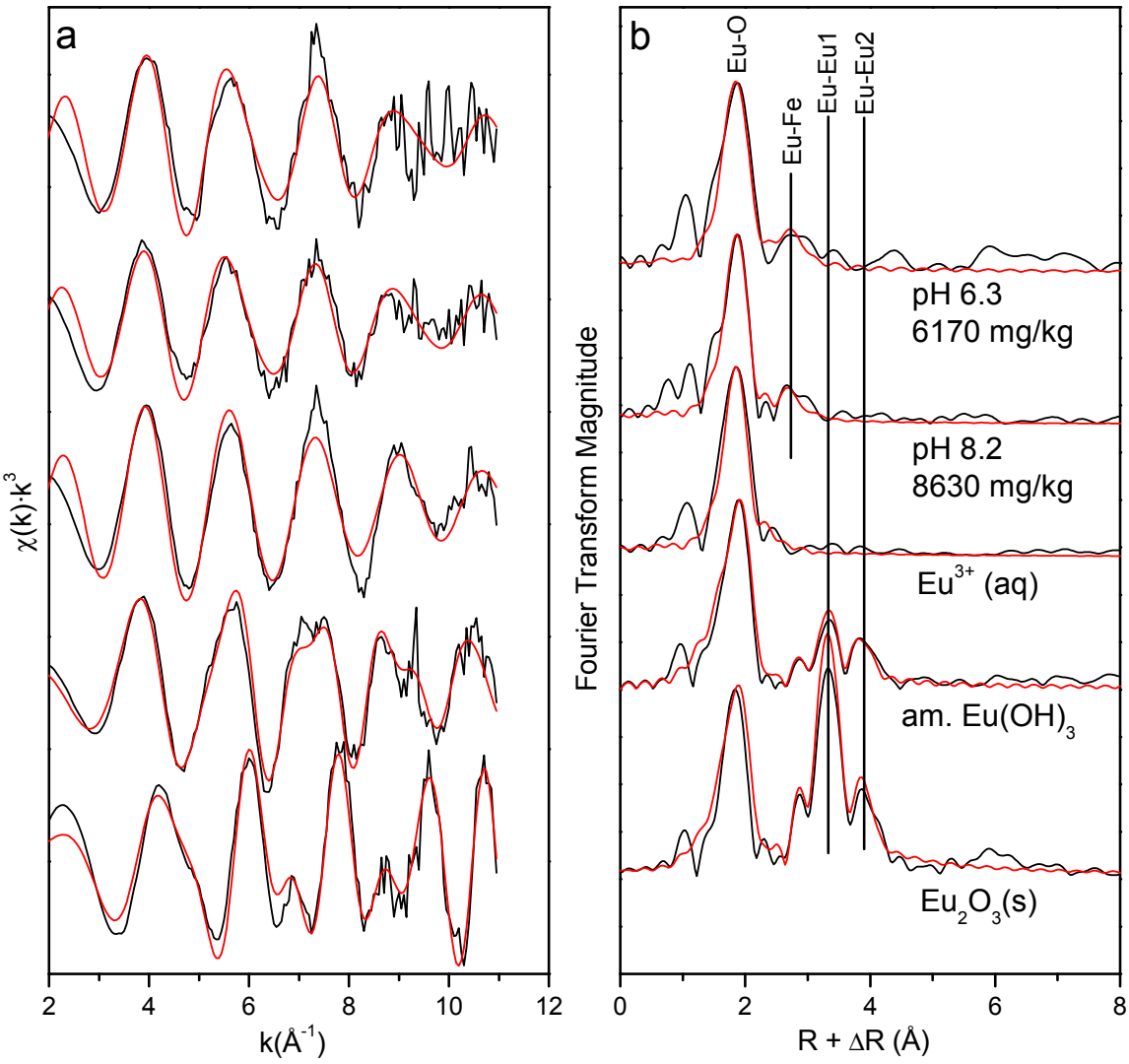

Figure 4.5: (a) Normalized, background-subtracted k^3-weighted Eu K-edge EXAFS spectra of Eu(III)-reacted hematite samples in air, aqueous Eu(III) in perchloric acid, am. $Eu(OH)_3$ precipitate, and a reference Eu_2O_3 (s) (Aldrich). The normalized k^3-weighted spectra and non-linear least-squares fit are shown in solid black and red lines, respectively. (b) Fourier-transformed k^3-weighted Eu K-edge EXAFS spectra of respective spectra shown in (a).

Table 4.3: Local structural parameters in reference and mineral samples from least-squares analyses of Eu K-edge EXAFS.[a]

sample	parameter[b]	O[c]	Eu1[c]	Fe[c]	Eu2[c]	R-factor	log SI[f]
crystalline	CN	6[e]	3(1)	—	4(1)	0.038	—
Eu_2O_3 (s)	R (Å)	2.360(9)	3.62(8)		4.09(1)		
	σ^2 (Å^2)	0.006(1)	0.002(1)		0.01[e]		
amorphous	CN	10(1)	0.7(1)	—	4.8(9)	0.046	—
$Eu(OH)_3$ (s)	R (Å)	2.464(8)	3.630(9)		4.06(1)		
	σ^2 (Å^2)	0.008(1)	0.002[e]		0.01[e]		
pH 8.2	CN	5.3(9)	—	1.1(7)	—	0.108	3.3
$\Gamma^d = 8,630$	R (Å)	2.21(1)		3.09(4)			
	σ^2 (Å^2)	0.006(1)		0.01[e]			
pH 6.3	CN	5(1)	—	1.2(7)	—	0.139	−1.2
$\Gamma^d = 6,170$	R (Å)	2.21(1)		3.08(4)			
	σ^2 (Å^2)	0.008(2)		0.01[e]			
pH 0.2	CN	8(1)	—	—	—	0.097	—
Eu^{3+} (aq)	R (Å)	2.20(1)					
0.5 M	σ^2 (Å^2)	0.006(1)					

[a] Estimated uncertainties in the last digit of each value are given in parentheses.
[b] CN, coordination number; R, interatomic distance (Å); σ^2, Debye-Waller factor (Å^2).
[c] Fit quality confident limit for parameters: Eu−O shell, $R = \pm 0.03$ Å; Eu−Fe/Eu shell, CN = ±20%, $R = \pm 0.03$ Å.
[d] Γ, surface coverage (mg kg^{-1}).
[e] Fixed parameter.
[f] Saturation index values, log SI, for $Eu(OH)_3$ (s) were estimated using the solubility product constant ($K_{sp} = 9.38 \times 10^{-27}$).[98]

despite the slight oversaturation (with respect to $Eu(OH)_3$) of the sample at pH 8.2. Additionally, Eu precipitates were difficult to locate in HRTEM analyses of the EXAFS samples, and the majority of areas scanned did not show any precipitates. As an example, the HRTEM image in Fig. 4.6 shows no Eu precipitates even though Eu was observed in EDX analysis. However, Eu precipitates were observed in a preliminary EXAFS sample prepared at pH 8, and the particles were found to have the structure of Eu_2O_3 rather than the expected $Eu(OH)_3$ which readily forms from oversaturation of aqueous solutions. The presence of Eu_2O_3 was identified by weak electron diffraction rings as well as high-resolution imaging of individual particles (Figs. A.2, A.3). As there was no observation of Eu−Eu distances in EXAFS spectra and only limited observations of Eu particles in HRTEM images,

we conclude that the precipitates do not represent a significant fraction of Eu in samples prepared at pH 8. However, the observation of Eu_2O_3 is unique and is the subject of further examination.

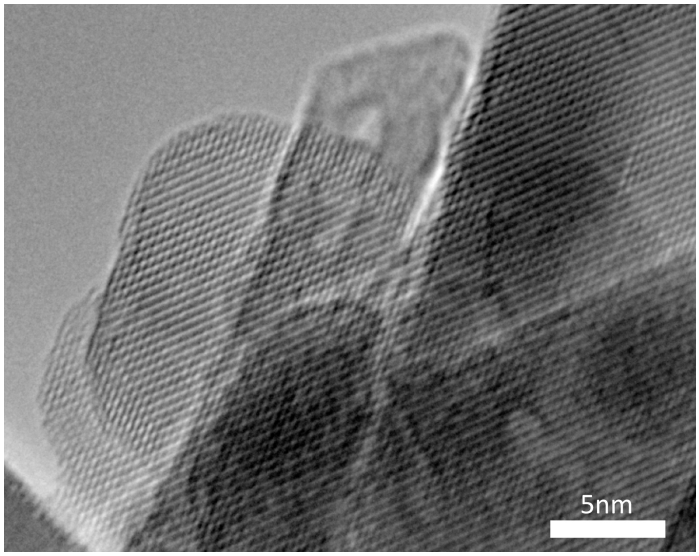

Figure 4.6: High-resolution transmission electron micrograph of Eu-hematite EXAFS sample at pH 8.2 showing the hematite edges without observable Eu precipitates.

For both mineral samples, the nearest-neighbor Fe atom was located at approximately 3 Å. Also, the Eu−O CN decreased from 8 ± 1 for the aqueous Eu(III) reference sample to approximately 5 ± 1 for both mineral samples. We attribute this change in CN to a release of coordinating H_2O molecules upon formation of a Eu(III) surface complex. The decrease in CN and the short Eu−Fe distance suggests that Eu forms an inner-sphere bidentate mononuclear surface complex, giving a Eu(III) ion coordinated to three water molecules and two oxygen atoms on the hematite surface. This surface complex is in agreement with our surface complexation modeling. Additionally, the decrease in CN supports our hypothesis that there is a loss of water from the Eu(III) primary hydration sphere during adsorption.

There are no known examples in the literature describing EXAFS data for Eu(III) reacted with hematite. However, Stumpf et al. studied the sorption of Eu(III) onto smectite and kaolinite using time-resolved laser fluorescence spectroscopy (TRLFS) and determined that Eu(III) formed primarily inner-sphere surface complexes with both clays above pH 3.5, and that above pH 7, Eu was coordinated to approximately 2.6 H_2O molecules, representing a loss of ~ 6 coordinating H_2O molecules.[99] Additionally, Dardenne et al. (2001) used TRLFS and EXAFS to study the sorption of Lu(III) onto 2-line ferrihydrite, and they also suggested the formation of an inner-sphere bidentate

surface complex. Although we attempted using TRLFS in the current work to confirm our EXAFS data, the samples yielded no Eu fluorescence indicating that the close proximity of surface Fe may be quenching the signal.

4.3.4 Enthalpy and Entropy Derivation

To describe the thermodynamics associated with the formation of the $(\equiv \mathrm{FeO})_2\mathrm{Eu}^{2+}$ surface species, we derived the enthalpy and entropy of the reaction using a van't Hoff plot which follows the relationship

$$\log K = -\frac{\Delta_r H}{\ln 10 \cdot RT} + \frac{\Delta_r S}{\ln 10 \cdot R} \tag{4.11}$$

where $\Delta_r H$ and $\Delta_r S$ are the enthalpy and entropy of the surface complexation reaction shown in Eq. 4.6.

Using the $\log K$ values derived directly from FITEQL, which are specific to our experimental system as discussed above, the van't Hoff plot (Fig. 4.7) yields a linear relationship between the equilibrium constants for the formation of $(\equiv \mathrm{FeO})_2\mathrm{Eu}^{2+}$ and inverse temperature, indicating that the enthalpy of reaction is constant over the studied temperature range. The $\Delta_r H$ calculated from the slope of the linear fit is 131 $\pm$ 8 kJ mol^{-1}; the entropy of reaction, $\Delta_r S$, calculated from the intercept, is 439 $\pm$ 26 J K^{-1} mol^{-1}. We also prepared the van't Hoff plot using the $\log K_3$ values given in Table 4.2 (Fig. A.4), and the calculated reaction enthalpy, denoted as $\Delta_r H_3$ is also 131 $\pm$ 8 kJ mol^{-1}. However, the reaction entropy calculated using the $\log K_3$ values, $\Delta_r S_3$, is 365 $\pm$ 28 J K^{-1} mol^{-1}. This reaction entropy is significantly different than the entropy calculated using the $\log K$ values.

It is not clear which equilibrium constants yield the most accurate estimate of reaction enthalpy and entropy. Because the $\log K_3$ values should be applicable for Eu(III) adsorption onto hematite at any solid phase concentration, and therefore may represent the intrinsic equilibrium constants, it is possible that $\Delta_r H_3$ and $\Delta_r S_3$ represent the best choice for estimating the reaction enthalpy and entropy for Eu(III) adsorption onto hematite. However, the $\log K_3$ values are referenced to the mole fraction standard state, which is not commonly used in chemical thermodynamics. As the $\log K$ values derived from FITEQL are referenced to the 1.0 M standard state and are most representative of our reaction system, we support that the reaction enthalpy and en-

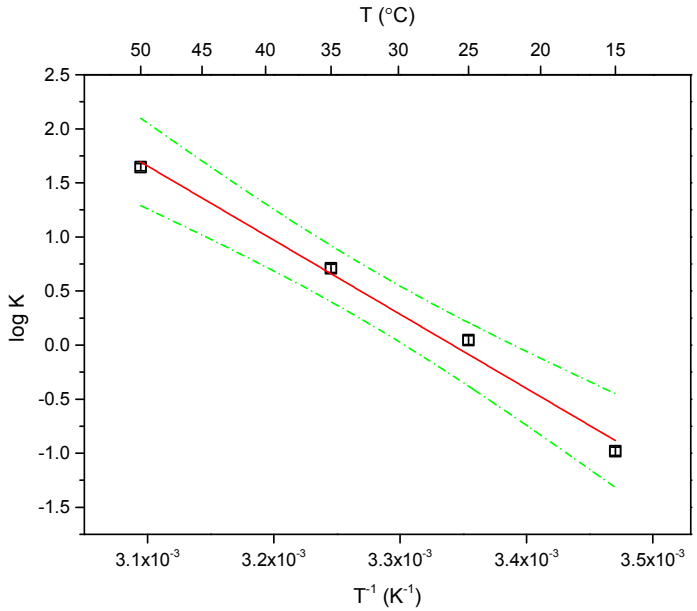

Figure 4.7: van't Hoff plot using $\log K$ values for the surface species $(\equiv \mathrm{FeO})_2\mathrm{Eu}^{+}$. The solid line is the linear fit with an adjusted R^2 equal to 0.989, and the dashed lines are the 95% confidence intervals.

tropy for Eu(III) adsorption onto hematite are best estimated as 131 $\pm$ 8 kJ mol^{-1} ($\Delta_r H$) and 439 $\pm$ 26 J K^{-1} mol^{-1} ($\Delta_r S$), respectively. Regardless, the positive values of enthalpy and entropy indicate that the formation of $(\equiv \mathrm{FeO})_2\mathrm{Eu}^{2+}$ is entropically driven. Reactions that increase system disorder, e.g. liquid to gas phase changes, and reactions that increase the total number of moles present are thermodynamically driven by positive entropy changes. Rearrangement of water within the primary hydration shell of metal ions is expected in order to accommodate space within the coordination shell for direct bonding to the mineral surface.[31] Because water in the bulk phase is less ordered than water molecules coordinated to metal ions, entropy would be gained if coordinating water molecules were lost from the hydration shell during adsorption. Additionally, as the temperature increases, the degree of disorder of bulk water increases, and thus a greater entropy contribution is possible. This phenomenon would be manifested by increased sorption with increasing temperature, as observed in this work (Fig. 4.4). Therefore, for the adsorption of Eu(III) onto hematite, we expect that the primary increase in entropy is due to the loss of coordinating H_2O molecules from the Eu(III) hydration shell upon complexation with the hematite surface.

Several researchers have used TRLFS analyses to study Eu(III) adsorption onto kaolinite[47,86,99] and smectites.[47,54] Both Stumpf et al.[99] and Ishida et al.[86] reported a decrease in the

number of water molecules coordinating Eu(III) inner-sphere surface complexes as compared to Eu(III) aqueous species. Similar to our work, Tertre et al. studied the adsorption of Eu(III) onto Na-montmorillonite and kaolinite at variable temperatures using TRLFS.[47] As mentioned above, these authors also observed an increase in Eu(III) adsorption at higher temperatures. While Tertre et al. did not specifically determine the number of water molecules coordinating Eu(III) surface complexes, they do suggest that dehydration would occur upon adsorption. Furthermore, their measurement of the fluorescence lifetime of adsorbed Eu(III) species of $\sim$ 200 μs suggests a coordination number of $\sim$ 5 according to Bauer et al.,[54] which would represent the loss of $\sim$ 4 to 5 coordinating waters in their experimental systems compared with aqueous Eu(III). Additionally, Tertre et al.[47] report a $\Delta_r H$ of $95 - 150$ kJ mol^{-1} for Eu(III) adsorption onto $\equiv$AlOH, which is close to value of 131 kJ mol^{-1} for Eu(III) adsorption onto hematite reported in the current work. Although Tertre et al.[47] studied Eu(III) adsorption to two different clays, their data not only supports our hypothesis that Eu(III) adsorption proceeds via a loss of coordinating water molecules, but also suggests that the Eu(III) adsorption mechanism may be similar for hematite, kaolinite, and Na-montmorillonite.

There is also evidence in the literature which suggests that the number of coordinating water molecules in the first hydration sphere of Eu(III) does not change over our studied temperature range (15 to 50 ℃). For example, Tian et al. studied the aqueous coordination environment of Cm(III) in variable concentrations of perchloric acid (i.e., a non-complexing medium) from 10 to 85 ℃, and determined that the Cm(III) CN did not deviate from 9 over the experimental temperature range.[100] Additionally, Kimura et al. studied the luminescence properties of Eu(III) over a wide temperature range and determined that the observed decay constant did not change over temperature ranges similar to those studied in this work, suggesting that the number of water molecules coordinated to Eu(III) is stable from 15 to 50 ℃.[101] These studies support that the calculated positive entropy change was due to the adsorption reaction and not due to changes in the aqueous Eu(III) hydration sphere with increasing temperature.

The combination of surface complexation modeling, EXAFS spectroscopy, and computational modeling presented here suggest that Eu(III) adsorption onto hematite results in the formation of a bidentate mononuclear surface complex with the loss of five coordinating H_2O molecules from the Eu(III) hydration sphere. Therefore, we propose that the reaction for Eu(III) adsorption

onto hematite is

$$2 \equiv \mathrm{FeOH} + \mathrm{Eu(H_2O)_8^{3+}} \rightleftharpoons \ (\equiv \mathrm{FeO})_2\mathrm{Eu(H_2O)_3^{+}} + 2\mathrm{H^{+}} + 5\mathrm{H_2O} \tag{4.12}$$

With the surface complexation reaction written in this manner, it becomes evident that we can approximate the entropic contribution from water. Using the standard molar entropy ($\overline{S}^{\circ}_{m}$) of liquid water (69.91 J $\mathrm{K^{-1}}$ $\mathrm{mol^{-1}}$), the entropy term associated with the release of five H_2O molecules from the Eu(III) coordination shell is approximately 350 J $\mathrm{K^{-1}}$ $\mathrm{mol^{-1}}$. This value is close to both $\Delta_r S$ and $\Delta_r S_3$ calculated above, and although we cannot account for the specific entropy terms associated with the other reaction components (e.g., hematite surface, hydrated Eu(III) ion, or the Eu(III) surface complex), it is likely that the primary contribution to the reaction entropy is due to this loss of water from the Eu(III) hydration sphere. However, as evident from the discrepancy in calculated reaction entropies described above, we highlight that the enthalpy and entropy values presented in this work are dependent on the surface complexation model used and that the reaction given in Eq. 4.12 is constrained by the diffuse layer model. More advanced modeling approaches such as the CD-MUSIC model may provide surface specific reactions and is the subject of ongoing work.

4.4 Conclusions

Changes in the hydration sphere of metal ions, such as proposed here, may have large effects on the environmental fate and transport of metals. For example, sorption reactions are not always completely reversible, and future studies may demonstrate that the desorption and the subsequent rehydration of metal ions may be kinetically or thermodynamically limited due to the high activation energy required to rehydrate the sorbed metal ions. Our results present a unique step toward understanding the thermodynamics and reaction mechanisms of Eu(III) and, by analogy, trivalent actinide adsorption at the solid-water interface by incorporating macroscopic, spectroscopic, and theoretical findings. However, it is still evident that additional studies are needed to fully understand these adsorption mechanisms, particularly studies that utilize complementary techniques (e.g., microcalorimetry) to measure the enthalpy and entropy of surface complexation reactions.

Chapter 5

Calorimetric Determination of the Enthalpy of Eu(III) Sorption onto Hematite*

Abstract

Modeling or predicting actinide sorption processes in the environment requires both a fundamental understanding of actinide sorption mechanisms, and the availability of thermodynamic constants which are valid over a wide range of conditions. Reaction enthalpies are not only important for modeling actinide sorption at temperatures other than 25 ℃ but also provide information regarding the fundamental sorption mechanism. However, few researchers have quantified this thermodynamic parameter. In this work, we demonstrate the combined use of isothermal titration calorimetry and surface complexation modeling to quantify the enthalpy of Eu(III) (a trivalent actinide analog) sorption onto hematite. The cumulative measured heat from four titrations, in which 0.01 M NaOH was injected into a hematite suspension containing Eu(III), was combined to quantify the sorption enthalpy. The calculated enthalpy for Eu(III) sorption onto hematite (I = 0.01 M NaCl) was

*This chapter has been prepared for submission to *Environmental Science & Technology Letters* with authors Shanna L. Estes and Brian A. Powell. Each author contributed the following: (1) Shanna L. Estes performed all calorimetric experiments and associated data analyses, and wrote the complete manuscript; (2) Brian A. Powell secured research funding, assisted with all data analyses, and reviewed the manuscript.

127.81 ± 2.84 kJ mol^{-1}, which agrees well with our previously reported value of 131 kJ mol^{-1} determined using the van't Hoff expression.

5.1 Introduction

Sorption onto soils, sediment, and rock surfaces is a primary control of radionuclide migration in the environment. For this reason, a fundamental understanding of actinide sorption mechanisms over a wide range of environmentally relevant conditions must be developed. Although many researchers have made significant progress toward this goal (reviewed by Geckeis et al.[30]), most have studied radionuclide sorption at only ambient laboratory temperatures ($\sim 20 - 25$ ℃). Consequently, the thermodynamic parameters needed to model actinide sorption processes at the various temperatures expected in natural systems, or the elevated temperatures (~ 80 ℃) expected in future geologic nuclear waste repositories,[43] are not available in the literature.

Recently, we demonstrated that sorption of Eu(III) (a trivalent lanthanide element and trivalent actinide analog) onto hematite ($\alpha-Fe_2O_3$) increases with increasing temperature (i.e., the reaction was endothermic).[102] Such endothermic sorption behavior has also been observed for several transition metals,[45,46] actinides,[3,42] and for other lanthanide/mineral systems,[47,54,92,93] and suggests that in the near-field of geologic nuclear waste repositories, sorption processes may be more favorable than previously expected. Additionally, although sorption behavior is generally endothermic, the overall sorption free energy tends to increase with increasing temperature, suggesting that sorption is driven by a favorable entropy change, which we previously hypothesized was due to the displacement of hydrating water molecules from the cation and mineral surface upon sorption.[102]

In many studies,[3,45,46,92] including our study of the Eu(III)-hematite system,[102] the slopes of van't Hoff plots ($\log K$ vs. T^{-1}) were used to determine sorption enthalpies. Although these van't Hoff enthalpies provide the means to predict cationic radionuclide sorption at temperatures not previously studied, van't Hoff enthalpies are inherently indirect and can have large uncertainties.[103] Isothermal titration calorimetry (ITC) measures the evolution of heat during a chemical reaction, allowing one to directly quantify reaction enthalpies ($\Delta_r H$),[50,104] and has been used to study uranium[105] and neptunium[23] hydrolysis. It has been demonstrated that, when combined with batch sorption studies, ITC can be effectively used to study cation sorption thermodynamics.[51,106–108] Therefore, the objective of this study was to quantify the enthalpy of Eu(III) sorption onto hematite

using ITC and the surface complexation model (SCM)[102] we developed previously.

5.2 Materials and Methods

5.2.1 Reagents

Hematite ($\alpha-Fe_2O_3$) was synthesized and characterized by Estes et al.[102] Standardized HCl (0.01, 0.1 N, Metrohm), HNO_3 (67–70%, BDH Aristar Plus), and NaCl (99%, BDH) were used as received. Standardized NaOH (0.01, Metrohm) was opened and stored in an anoxic glove box ($\sim$ 1% H_2, 99% N_2, Coy) during use to limit CO_2 dissolution. Eu(III) working solutions ($\sim$ 1 mM in 0.01 M NaCl) were prepared from $EuCl_3 \cdot xH_2O$ (98%, Alfa Aesar) – actual concentrations were measured using inductively-coupled plasma mass spectrometry (Thermo X Series 2). All solutions and suspensions were prepared in de-gassed (boiled and cooled under N_2 purge) ultrapure H_2O ($>$ 18 MΩ cm, ELGA Purelab).

5.2.2 Isothermal Titration Calorimetry

Calorimetric titrations were performed at 25 ℃ with an isothermal microcalorimeter (TA Instruments TAM III). This calorimeter measures the difference in heat flow (i.e., power) between sample and reference ampoules (1 mL stainless steel) as a function of time. For all titrations, the reference ampoule contained a hematite suspension identical to that in the sample ampoule, and the titrant was delivered to the sample ampoule through a stainless steel needle from a 250 μL glass syringe. The calorimeter setup did not permit active purging of the ampoule headspace with an inert gas, so some CO_2 dissolution during the titrations cannot be excluded. Additionally, pH measurement during the titrations was not possible. Therefore, only initial and final suspension pH values were measured (Ross semi-micro, Thermo) and are reported as the average $\pm$ 1σ.

To minimize the number of adjustable parameters during the non-linear regression analysis (see below), the enthalpies for protonation ($\Delta_r H_2$) and de-protonation ($\Delta_r H_3$) of the hematite surface were determined separately from the enthalpy of Eu(III) sorption onto hematite. To quantify $\Delta_r H_2$ and $\Delta_r H_3$, a total of nine titrations were performed. For each titration, 800 μL of a 7.77 or 7.91 g L^{-1} hematite suspension in 0.01 M NaCl (pH 6.65 $\pm$ 0.18) was titrated with $\sim$ 200 μL (9.98 μL increments) of either 0.01 N HCl (acid titration) or 0.01 N NaOH (base titration). Average

pH values at the end of the acid and base titrations were 2.79 ± 0.05 and 10.83 ± 0.15, respectively. Measured initial and final pH values for individual titrations are given in Table B.1. Similarly, several titrations were completed to determine the enthalpy of Eu(III) sorption onto hematite ($\Delta_r H_4$). In each of these titrations, 810 μL of a 6.71 g L^{-1} hematite suspension in 0.01 M NaCl and containing 1.56×10^{-4} M $EuCl_3$ at pH 3.09 ± 0.09 (adjusted with 0.1 N HCl) was titrated with $\sim$ 150 μL (4.97 μL increments) of 0.01 N NaOH. Titrant injection intervals were set at either 25 or 45 min., which allowed sufficient time for heat flow to return to baseline conditions between each injection (i.e., sorption and other reactions reached apparent equilibrium). Throughout all titrations, ionic strength (0.01 M NaCl) and mixing (150 rpm with gold impeller) were constant. Thermogram peaks were automatically integrated using TAM Assistant software (TA Instruments) to give the measured heat (Q) for each titrant injection. The heat due to dilution and mixing ($Q_{dil.}$) was determined from separate experiments in which a hematite suspension was titrated with 0.01 M NaCl. The net heat (Q_{net}) for each injection was calculated as the difference between Q and $Q_{dil.}$. In most cases, $Q_{dil.}$ was negligible.

5.2.3 Enthalpy Quantification

The enthalpies for hematite protonation and de-protonation and for Eu(III) sorption onto hematite were calculated using the equation

$$Q_{T,calc.} = \sum_{i=1}^{j} \Delta n_i \cdot \Delta_r H_i \tag{5.1}$$

where Q_T is the cumulative heat evolved after each injection from all chemical reactions i to j, Δn_i is the cumulative moles of product formed from reaction i, and $\Delta_r H_i$ is the enthalpy of reaction i. The moles of each reaction product formed were calculated by modeling the titration conditions using a modified version of FITEQL[64] and our previously developed diffuse layer SCM.[102] Details of the SCM are given in Table 5.1. Enthalpy values for each reaction were either obtained from the literature or calculated by fitting the measured cumulative heat ($Q_{T,meas.}$) with a multiple independent-variable non-linear regression (user defined from Eq. 5.1) using the graphical analysis software package Origin (OriginLab, Northhampton, MA). A block diagram (Fig. B.1) is given in Appendix B to illustrate the steps needed to calculate sorption enthalpies from ITC data.

5.3 Results and Discussion

5.3.1 Quantification of Hematite Protonation and De-protonation Enthalpies

Five acid and four base titrations were used to quantify the enthalpies of hematite protonation ($\Delta_r H_2$) and de-protonation ($\Delta_r H_3$). Changes in surface speciation during the titrations were simulated with FITEQL using the parameters and reactions given in Table 5.1. Because it is not possible to separate the hematite surface reactions by experiment, we simultaneously determined $\Delta_r H_2$ and $\Delta_r H_3$ for each titration by fitting $Q_{T,meas.}$ as a function of moles of $\equiv\mathrm{FeOH_2^+}$, $\equiv\mathrm{FeO^-}$, and $\mathrm{OH^-}$ formed or consumed. The resulting fits and enthalpies for individual titrations are shown in Appendix B (Figs. B.2, B.3; Table B.1).

Table 5.1: Hematite characteristics, surface complexation model reactions and constants, and reaction enthalpies from the literature or calculated in this work.

i		parameter reaction	value $\log K$	calculated $\Delta_r H_i$ [a,b]	referenced $\Delta_r H_i$ [b]
		pzc	7.36[c]		
		BET surface area ($m^2\ g^{-1}$)	30.7[c]		
		site density (sites nm^{-2})	4.28[c]		
1	K_w°	$H_2O \rightleftharpoons H^+ + OH^-$	−13.99[d]		55.8[e]
2	K_+	$\equiv FeOH + H^+ \rightleftharpoons \equiv FeOH_2^+$	6.19[f]	3.1 ± 7.2	−32.2[c], −41.4[g]
3	K_-	$\equiv FeOH \rightleftharpoons \equiv FeO^- + H^+$	−8.11[f]	38.6 ± 8.7	32.2[c], 48.5[g]
4	K_{SC}	$2 \equiv FeOH + Eu^{3+}$ $\rightleftharpoons (\equiv FeO)_2Eu^+ + 2H^+$	−1.08[h]	127.81 ± 2.84	131 ± 8[c]

[a] Calculated enthalpies are reported $\pm\ 1\sigma$.
[b] kJ mol^{-1}
[c] Estes et al.[102]
[d] $I = 0$ M, $T = 25$ °C; calculated according to Bandura and Lvov.[85]
[e] From Martell et al.[109]
[f] Calculated by Estes et al.[102] using a single-site diffuse layer model (DLM); $I = 0.01$ M NaCl, $T = 25$ °C, referenced to the 1.0 M standard state.
[g] Sverjensky and Sahai[71]
[h] Calculated from values given by Estes et al.[102] for a single-site DLM and the equation from Wang and Giammar[68]: $\log K_{SC} = \log K_3 - \log(N^\dagger A_s C_s)$, where $\log K_3$ is −3.91, $N^\dagger$ is the molar site density (7.11×10^{-6} mol m^{-2}), A_s is the specific surface area (30.7 $m^2\ g^{-1}$, and C_s is the solid phase concentration used in this work (6.71 g L^{-1}); $I = 0.01$ M NaCl, $T = 25$ °C, referenced to the 1.0 M standard state.

Calculated average enthalpies for protonation ($\Delta_r H_2$) and de-protonation ($\Delta_r H_3$) of the hematite surface are given in Table 5.1. Hematite deprotonation, $\Delta_r H_3$, agrees well with the theoretical value (48.5 kJ mol^{-1}) proposed by Sverjensky and Sahai[71] and with our previously estimated value (32.2 kJ mol^{-1}).[102] However, $\Delta_r H_2$ is significantly different from values reported in the literature (Table 5.1). Additionally, $\Delta_r H_2$ calculated here is slightly endothermic, whereas in all other reports, the protonation enthalpy, for hematite and other metal oxides, is exothermic.[61,71,79,102,107] Several explanations for this disagreement were considered : (1) CO_2 dissolution during the titrations; (2) inability of the SCM to accurately predict the hematite chemistry during the titrations; or (3) formation of unidentified chemical species during the titrations. Incorporating CO_2 dissolution and the subsequent formation of aqueous carbonate species in the SCM significantly worsened our fit results, suggesting that CO_2 dissolution during the titrations did not significantly affect $Q_{T,meas.}$. Furthermore, predicted final hematite suspension pH values agreed within $\pm$ 3% of all measured values, suggesting that CO_2 dissolution was insignificant (see Table B.1). The formation of unidentified chemical species, perhaps due to impurities present on the hematite surface, is also a possible explanation for the disagreement between calculated and reported protonation enthalpies. However, this too seems unlikely because the SCM was developed from accurately predicted potentiometric titrations of the same hematite at 25 °C.[102] For the purposes of the current work, the calculated values of $\Delta_r H_2$ and $\Delta_r H_3$ adequately described the calorimetric acid and base titrations and will therefore be used for quantification of the Eu(III) sorption enthalpy. However, it is clear that additional investigation is needed to verify the hematite protonation and de-protonation enthalpies.

5.3.2 Quantification of Eu(III) Sorption Enthalpy

Four calorimetric base titrations were completed to quantify the enthalpy of Eu(III) sorption onto hematite. To achieve measurable sorption heat during the titrations, high concentrations of Eu(III) ($\sim 10^{-4}$ M) were necessary. Despite these elevated Eu(III) concentrations, equilibrium modeling with Visual MINTEQ indicated that $Eu(OH)_3$ remained undersaturated over the course of each titration. Including CO_2 dissolution and the formation of aqueous carbonate species (including $EuCO_3^+$) worsened our fit results, again suggesting that CO_2 dissolution during the titrations was negligible. Furthermore, formation of $EuOH_2^+$ during the titrations was also negligible and was therefore excluded. The final SCM included only the four reactions shown in Table 5.1.

A typical titration thermogram and the corresponding simulated changes in surface speci-

ation are shown in Fig. 5.1. Results from the SCM indicated that both pH and concentration of adsorbed Eu(III) increased as the titrations progressed, with the greatest amount of Eu(III) sorption occurring during the second half of each titration (Fig. 5.1). The final average measured pH at the end of each titration (8.2 ± 1.1) differed from the final predicted pH (9.4), and was more variable than for the hematite acid and base titrations. However, this discrepancy was likely due to small variations in the initial pH (3.09 ± 0.09) of each suspension.

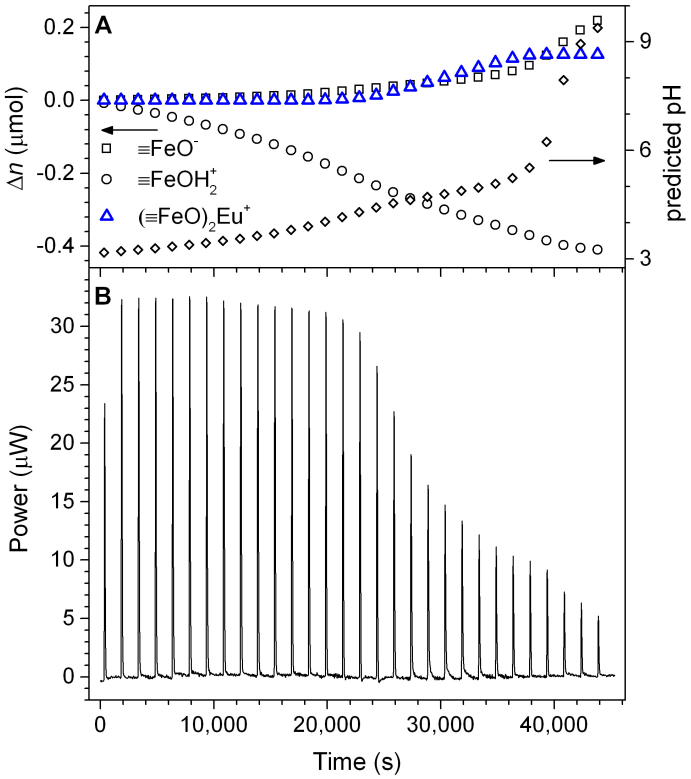

Figure 5.1: Change in pH (right y-axis) and hematite surface species (left y-axis) as a function of titration progress (A), and typical titration thermogram for Eu(III) sorption onto hematite (B). Titration prarameters: $[\text{Eu(III)}]_0 = 1.56 \times 10^{-4}$ M, $[\alpha\text{–Fe}_2\text{O}_3] = 6.71$ g L^{-1}, $I = 0.01$ M NaCl, $T = 25$ ℃, titrant = 0.01 M NaOH, injection volume = 4.97 μL.

The enthalpy of Eu(III) sorption onto hematite ($\Delta_r H_4$) was calculated by simultaneously fitting $Q_{T,meas.}$ for each titration as a function of moles of $(\equiv\text{FeO})_2\text{Eu}^+$, $\equiv\text{FeOH}_2^+$, $\equiv\text{FeO}^-$, and OH^- formed. The resulting fit and the measured cumulative heat for each titration are shown in Fig. 5.2 as a function of $(\equiv\text{FeO})_2\text{Eu}^+$, and the calculated $\Delta_r H_4$ is given in Table 5.1. Although the cumulative heat evolved during the Eu(III) titrations was reproducible (Fig. 5.2), the cumulative heat evolved during titration 3 appeared artificially low. Therefore, we also calculated the Eu(III) sorption

enthalpy for each titration individually (Table B.2). However, the sorption enthalpy calculated from titration 3 was not statistically different (95% confidence level via Q-test[110,111]) than the sorption enthalpies calculated from the other three titrations (see Fig. B.4, Table B.2), and, therefore, could not be excluded from our calculations. There was no statistical difference in $\Delta_r H_4$ calculated from the two fitting methods.

Previously, we used a van't Hoff analysis to approximate the enthalpy of Eu(III) sorption onto hematite.[102] Although the enthalpy value from that work was derived from batch sorption experiments at much lower Eu(III) and hematite concentrations, the $\Delta_r H_4$ calculated here is in excellent agreement with the value we previously reported (Table 1), suggesting that the SCM adequately describes Eu(III) sorption onto hematite even at these much higher concentrations. Additionally, the Eu(III) coordination environment at the hematite surface (inner-sphere bidentate mononuclear) determined from extended x-ray absorption fine structure (EXAFS) spectroscopy agreed with surface complexation modeling results,[102] further supporting that this SCM can be used for a wide range of Eu(III) and hematite concentrations.

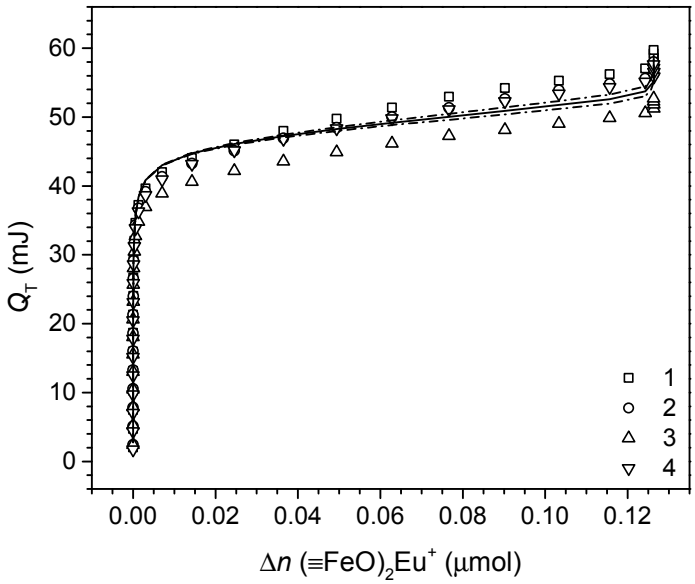

Figure 5.2: Cumulative enthalpy plot as a function of $(\equiv FeO)_2Eu^+$ formation. Titration parameters: $[Eu(III)]_0 = 1.56 \times 10^{-4}$ M, $[\alpha\text{–}Fe_2O_3] = 6.71$ g L^{-1}, $I = 0.01$ M NaCl, $T = 25$ ℃, titrant = 0.01 M NaOH, injection volume = 4.97 μL. Open symbols are the measured cumulative heat for each titration 1 – 4; the solid line is the cumulative heat simultaneously calculated from all titration data (adjusted $R^2 = 0.987$); the dashed lines are the 95% upper and lower confidence limits.

Although we ultimately used a calorimetric base titration to quantify the enthalpy of Eu(III)

sorption onto hematite, we initially attempted to directly measure the Eu(III) sorption heat by titrating hematite (at pH ~ 6) with a Eu(III) solution (Fig. B.5). However, very little heat evolved during these titrations, making the signal to noise ratio in the thermograms too poor for confident peak integration and enthalpy quantification. We hypothesized that this minimal heat evolution was due to competition between the endothermic Eu(III) sorption reaction and exothermic acid neutralization due to changes in suspension pH as Eu(III) sorption increased. Similar to the work by Morel et al.[108] for Eu(III) sorption onto alumina ($\gamma-Al_2O_3$), increasing the Eu(III) concentration in the titrant may have improved the signal to noise ratio, but it would have also eliminated our ability to maintain an ionic strength of 0.01 M NaCl throughout the titration. Therefore, we used the alternative base titration method described above. However, because these Eu(III) titrations were quite interesting, displaying both exothermic and endothermic peaks in the thermograms (Fig. B.5), we further analyzed the data. Analysis details are given in Appendix B. Although we have less confidence in this value, the Eu(III) sorption enthalpy calculated from this titration was 127.5 ± 1.5 kJ mol^{-1} (Fig. B.6), which is in excellent agreement with both the enthalpy calculated above and the van't Hoff enthalpy[102] we reported previously.

We have used isothermal titration calorimetry to quantify the enthalpy of Eu(III) sorption onto hematite. Our results clearly indicate that the reaction is endothermic, which agrees well with several other studies,[47,108] and which indicates that Eu(III) sorption onto hematite occurs via an inner-sphere mechanism in which some dehydration of the Eu(III) ion occurs.[31] The ITC methods applied in this work provide a direct measure of sorption enthalpy through a self-consistent surface complexation model. Such data can populate databases for understanding radionuclide geochemical speciation and facilitate an understanding of the pertinent sorption mechanisms. Therefore, we envision these calorimetric techniques as a powerful tool for quantifying reactions at solid-water interfaces.

Chapter 6

The Thermodynamics of U(VI) Sorption onto Hematite*

Abstract

In this work, we have examined the thermodynamics of U(VI) sorption onto hematite (α−Fe_2O_3) using a combination of macroscopic techniques. Batch sorption experiments (0.51 g L^{-1} α−Fe_2O_3, $I = 0.01$ M NaCl) were conducted at two total U(VI) concentrations ($\sim 2\times10^{-8}$ and $\sim 4\times10^{-8}$ M) over the pH range 3 to 6.5 at 15, 25, 35, 50, and 80 ℃. Isothermal calorimetric titrations were also performed to directly measure U(VI) sorption enthalpy. Application of the diffuse layer model (DLM) to the batch sorption data suggested a temperature dependent change in uranyl surface speciation from $(\equiv FeOH)_2UO_2^{2+}$ and $(\equiv FeO)_2UO_2OH^-$ at 15 and 25 ℃, to $(\equiv FeOH)_2UO_2^{2+}$ at 35 and 50 ℃, to $(\equiv FeO)_2UO_2$ at 80 ℃. Results from the batch sorption experiments and isothermal titration calorimetry suggest that U(VI) sorption onto hematite is an endothermic, entropically driven reaction, with reaction enthalpies ranging from $\sim$ 36 to 100 kJ mol^{-1}. The thermodynamic parameters indicate that U(VI) sorption onto hematite occurs via an inner-sphere mechanism, which agrees with extended X-ray absorption fine structure (EXAFS) data from the literature that suggest that two water molecules are lost from the U(VI) hydration sphere during formation of bidenate uranyl

*This chapter has been prepared for submission to *Geochimica et Cosmochimica Acta* with authors Shanna L. Estes and Brian A. Powell. Each author contributed the following: (1) Shanna L. Estes performed all batch sorption and calorimetric experiments, performed all associated data analyses, and wrote the complete manuscript; (2) Brian A. Powell secured research funding, assisted with all data analyses, and reviewed the manuscript.

surface complexes. However, enthalpies and entropies for the formation of both $(\equiv FeOH)_2UO_2^{2+}$ and $(\equiv FeO)_2UO_2OH^-$ are less than the enthalpy and entropy for the formation of a Eu(III)-hematite surface complex reported in the literature, which may indicate a weaker interaction between U(VI) and the hematite surface, compared with Eu(III).

6.1 Introduction

Uranium is a common soil, sediment, and groundwater contaminant at legacy U.S. nuclear defense sites.[4] Present predominantly as the highly mobile uranyl oxycation ($U(VI)O_2^{2+}$) in these oxic or suboxic subsurface environments, uranium poses a significant health risk to future populations if off-site migration occurs. Therefore, it is necessary to understand the mechanisms controlling uranium transport, particularly sorption to solid surfaces, which is expected to play a primary role in the immobilization of actinides within the environment.

Many researchers have studied U(VI) sorption onto several iron oxy(hydr)oxides using both macroscopic batch techniques[e.g.,83,89,112–115] and spectroscopy.[e.g.,55,116,117] Results from these studies and others generally indicate that: (1) U(VI) sorption is favored at circumneutral pH; (2) the formation of uranyl-carbonate and alkaline earth-uranyl-carbonate complexes decreases sorption; and (3) inner-sphere bidentate surface species dominate, but ternary uranyl-carbonate or multimeric uranyl surface species may form at higher pH or carbonate concentrations, or higher uranyl concentrations, respectively. Cumulatively, there is a fairly robust understanding of U(VI) sorption onto iron oxy(hydr)oxides, even though there is still some debate over the relative importance of ternary uranyl-carbonate surface complexes under mildly acidic conditions,[55,117–119] and on whether U(VI) forms mononuclear (i.e., edge-sharing) or binuclear (i.e., corner-sharing) surface complexes.[32,55,83,89,119] However, there is relatively little information regarding the sorption processes of U(VI) or other actinides at temperatures above or below 25 ℃, despite the variable temperatures expected in natural systems, and the elevated temperatures (due to radioactive decay) expected in future subsurface nuclear waste repositories.[43]

From the studies available, there is evidence which suggests that actinide sorption is an endothermic process. For example, Lu et al. observed an approximately 40% increase in Pu(V) sorption onto montmorillonite as temperature was increased from 20 to 80 ℃.[42] Similarly, Almazan-Torres et al. also observed increased U(VI) sorption onto zirconium oxo-phosphate at elevated

temperatures.[3] These data suggest that actinide sorption processes may be enhanced at the temperatures expected under repository conditions. Therefore, to improve our ability to predict actinide transport in both natural and engineered systems, it is important to investigate the sorption of U(VI) and other actinides over a range of temperatures. Furthermore, studying actinide sorption thermodynamics can also lead to a deeper understanding of the mechanisms that govern these reactions. For example, we recently linked the sorption of Eu(III) onto hematite, an endothermic, entropically favorable reaction, to a loss of approximately five coordinating water molecules from the Eu(III) primary hydration sphere.[102] This finding indicated that Eu(III) sorption proceeded via an inner-sphere mechanism,[13,31] which may result in kinetically hindered desorption because of the expected large activation energy associated with Eu(III) rehydration.[102]

The objectives of this work were therefore to examine the influence of temperature on U(VI) sorption onto hematite and to correlate the observed thermodynamic properties to sorption mechanisms and changes in the U(VI) hydration sphere. To do this, we have combined multi-temperature batch sorption experiments, surface complexation modeling, and isothermal titration calorimetry. The results clearly indicate that U(VI) sorption onto hematite is an endothermic, entropically driven reaction. However, comparisons with the literature and our previous work suggest that fewer water molecules are lost from the U(VI) hydration sphere upon sorption compared with Eu(III). The implications these findings may have on U(VI) migration in the environment are briefly discussed.

6.2 Materials and Methods

6.2.1 Reagents

Hematite ($\alpha-Fe_2O_3$) was synthesized and characterized by Estes et al.[102] HNO_3 (67–70%, BDH Aristar Plus), NaCl (99%, BDH), and standardized HCl (0.01, 0.1 N, Metrohm) and NaOH (0.01, 0.1 N, Metrohm) were used as received. Calibration standards (in 2% HNO_3) and working solution #1 (WS1, 6.30×10^{-5} M U(VI) in 0.01 N HCl) were prepared by diluting a U plasma standard (1,000 μg L^{-1} in 2% HNO_3, High Purity Standards). Working solution #2 (WS2, 2.1×10^{-3} M U(VI) in 0.01 M NaCl) was prepared from $UO_2(NO_3)_2 \cdot 6H_2O$ (99.9–100%, EMS). Solutions and suspensions for the batch sorption work were prepared in ultrapure H_2O (resistivity > 18 MΩcm, < 5 ppb organic carbon, Millipore SuperQ or ELGA Purelab). For the calorimetry experiments, all

suspensions and solutions were prepared in de-gassed (boiled and cooled under N_2 purge) ultrapure H_2O. Additionally, the standardized NaOH (0.01 N, Metrohm) used for the calorimetry experiments was opened and stored in an anoxic glove box (1% H_2, 99% N_2, Coy) to limit CO_2 dissolution.

6.2.2 Multi-Temperature Batch Sorption

Batch sorption experiments were conducted in 125 mL screw top polycarbonate (PC) Erlenmeyer flasks. Before use, each flask was washed once with 2% HNO_3, rinsed three times with ultrapure H_2O, and dried in an oven at 105 ℃. Hematite was added to each flask as the dry solid, and then suspended in 0.01 M NaCl. These initial suspensions were mixed at room temperature for approximately 48 hours to adequately hydrate the hematite. After this step, an aliquot of WS1 was added to each flask, and the pH of each suspension was immediately adjusted using HCl or NaOH. The final suspensions contained 0.51 g L^{-1} hematite, $(2.16 \pm 0.06) \times 10^{-8}$ M U(VI) (system A) or $(4.35 \pm 0.06) \times 10^{-8}$ M U(VI) (system B), and 0.01 M NaCl in a total volume of $\sim$ 60 mL. Reported uncertainties in the uranium concentrations are the standard deviation of the exact concentrations of all samples. The suspension pH ranged from 3 to 6.5, and all reaction systems were prepared in duplicate.

Immediately following the above preparation, all flasks were placed in a temperature controlled orbital shaker (VWR) at 15 ℃. After 3 days of mixing, the pH of each suspension was measured using a combination pH electrode with automatic temperature compensation (Thermo 9157BNMD), and the suspensions were sampled by removing a 1.5 mL homogenous aliquot from each. Sample aliquots were centrifuged at 22,065g for 30 min to sediment particles larger than $\sim$ 60 nm based on Stokes Law (Beckman and Coulter Allegra 22R centrifuge with a F2402 rotor). After centrifugation, 1 mL of supernatant was diluted with 9 mL of 2% HNO_3 and analyzed for total U by inductively-coupled plasma mass spectrometry (ICP-MS, Thermo X Series 2) with ^{242}Pu as an internal standard. After 2 to 4 additional days of mixing, the suspensions were sampled a second time, and equilibrium was assumed if there were no significant differences between measured U concentrations for the two sampling events. If equilibrium was not achieved, the suspensions were mixed for an additional 2 to 4 days, and then sampled again. Once equilibrium was achieved (within three sampling events for all temperatures), the reaction temperature was increased, and this procedure was repeated to give U(VI) sorption data at 15, 25, 35, 50, and 80 ℃. The flasks were moved into a reciprocal shaking water bath (VWR) to measure U(VI) sorption at 80 ℃.

6.2.3 Isothermal Titration Calorimetry

All calorimetric titrations were performed in 1 mL stainless steel ampoules at 25 ℃ with an isothermal microcalorimeter (TA Instruments TAM III), which measures the heat flow (i.e., power) difference between reference and sample ampoules. The contents of the reference ampoule were always identical to the contents initially present in the sample ampoule. Although solutions and suspensions used for the calorimetric titrations were CO_2 free, some CO_2 dissolution during the titrations cannot be excluded because the ampoule headspace could not be actively purged with an inert gas. Additionally, it was not possible to monitor changes in suspension pH during the titrations. As such, the suspension pH was only measured before and after the titrations, and pH values are reported as the average for all titrations $\pm$ 1σ.

For each titration, the titrant was delivered into the sample ampoule from a 250 μL glass syringe via a stainless steel needle. A total of three titrations were completed in which a hematite suspension (810 μL, 5.14 g L^{-1}) at pH 3 (adjusted with 0.1 N HCl) in 0.01 M NaCl and containing 2.59×10^{-4} M $UO_2(NO_3)_2$ (from WS2) was titrated with $\sim$ 150 μL of 0.01 N NaOH in 4.97 μL increments. The titrant was injected every 25 min., and both ionic strength (0.01 M NaCl) and mixing (150 rpm with gold impeller) remained constant throughout each titration. Peaks in each thermogram were automatically integrated by the TAM Assistant software (TA Instruments) to give the measured heat (Q) for each injection. The dilution and mixing heat for each injection ($Q_{dil.}$) was determined from a separate experiment by titrating a hematite suspension with 0.01 M NaCl. For each injection, the net heat (Q_{net}) was calculated from the difference:

$$Q_{net} = Q - Q_{dil.} \tag{6.1}$$

, and the cummulative measured heat ($Q_{T,meas.}$) was calculated from:

$$Q_{T,meas.} = Q_{net,x} + Q_{net,x-1} + Q_{net,x-2} + \ldots Q_{net,x-\infty} \tag{6.2}$$

where x is the titrant injection number.

6.2.4 Surface Complexation Modeling

The surface complexation model (SCM) was developed from batch sorption data collected at each temperature using a modified version of FITEQL 4.0.[64] A description of the FITEQL modifications are given by Estes et al.[102] The SCM was developed using the single-site diffuse layer model (DLM),[67] which was chosen both for comparison with previous work, and because it has few adjustable parameters. U(VI) sorption data from both batch systems A and B were combined and fit simultaneously to develop a SCM which described sorption at multiple U(VI) concentrations. All experimental data was assigned a 5% relative error, and the ratio of the weighted sum of squares to the degrees of freedom (WSOS/DF) was used to indicate fit quality. The Davies model was used for all activity corrections, and the Davies A parameter was adjusted for temperature according to Langmuir.[9] The equilibrium constants developed using FITEQL are referenced to the 1.0 M standard state and are reported $\pm$ 1σ. However, we also report calculated equilibrium constants referenced to both the mole fraction[68] and site-occupancy[69] standard states. All bidentate reactions are represented with the notation $(\equiv \mathrm{FeOH})_2$ or $(\equiv \mathrm{FeO})_2$. However, this does not indicate bidentate binuclear surface coordination – such surface site specificity is not possible with the DLM. Instead this notation simply indicates that two surface sites are needed to describe the surface reaction mass balance.

6.2.5 Thermodynamic Parameter Quantification

The enthalpy of U(VI) sorption onto hematite was quantified: (1) from the van't Hoff relationship, as described in Section 6.3.1.3; and (2) from the calorimetric titration data, using the equation

$$Q_{T,calc.} = \sum_{i=1}^{j} \Delta n_i \cdot \Delta_r H_i \tag{6.3}$$

where $Q_{T,calc.}$ is the calculated cumulative heat evolved after each injection from all chemical reactions i to j, Δn_i is the cumulative moles of product formed from reaction i, and $\Delta_r H_i$ is the enthalpy of reaction i. Using the SCM developed from the batch experiments in this work, the moles of each reaction product formed after each titrant injection were calculated by modeling the calorimetric titration conditions in FITEQL. U(VI) sorption enthalpies were then calculated by fitting the measured cumulative heat ($Q_{T,meas.}$) with a multiple-independent variable non-linear regression (user defined from Eq. 6.3) using the graphical analysis software package Origin (OriginLab, Northhamp-

ton, MA). The van't Hoff and calorimetric enthalpies are reported ± 1σ. For analytical consistency, the enthalpies of hematite protonation ($\Delta_r H_2$) and de-protonation ($\Delta_r H_3$) used in Eq. 6.3 were also determined from calorimetric titrations, and are +3.06 and +38.59 kJ mol^{-1}, respectively (see Ch. 5). As discussed in Ch. 5, these enthalpies adequately reproduced the measured cumulative heat from hematite acid and base titrations and are therefore appropriate for use in Eq. 6.3. However, the enthalpies above are different than values determined from alternative techniques,[61,69,102] and therefore were not used to calculate $\log K_+$ and $\log K_-$ at each temperature (Table 6.1).

6.3 Results

6.3.1 Multi-Temperature Batch Sorption

6.3.1.1 Effect of Temperature

Typical for the sorption of cationic metals onto metal oxide surfaces,[31] U(VI) sorption increased from 0 to 100% over a narrow pH range ($\sim$ 1.5 pH units), regardless of initial U(VI) concentration (Fig. 6.1). As temperature increased from 15 to 80 ℃, a noticeable shift in the U(VI) sorption edge to lower pH occurred (Fig. 6.1). Re-plotting the batch sorption data as a function of "pH – $1/2\mathrm{p}K_w$," which effectively eliminated temperature dependence in the x-axis, also demonstrated a clear, albeit smaller, shift in the U(VI) sorption edge (Fig. C.1). This result indicates that U(VI) sorption onto hematite increased with increasing temperature (i.e., the reaction is endothermic), which is consistent with previous reports of endothermic sorption behavior for several transition metals,[45,46] lanthanides,[47,54,92,93,102] and actinides.[3,42]

6.3.1.2 Surface Complexation Model Development

Based on the expected aqueous U(VI) speciation in the batch experiments (Fig. 6.2), we included formation of both the first and second U(VI) hydrolysis products in the SCM. The formation of UO_2Cl^+ was also included in the SCM, but was generally negligible over the experimental pH range. Although the batch systems were open to the atmosphere and aqueous uranyl-carbonate complexes are expected above pH 5.5,[e.g.,89] including aqueous or surface uranyl-carbonate species in the SCM did not improve our fit results, likely because our experimental conditions resulted in 100% U(VI) sorption below pH 5.5 at all studied temperatures (Fig. 6.1). Furthermore, previous studies have

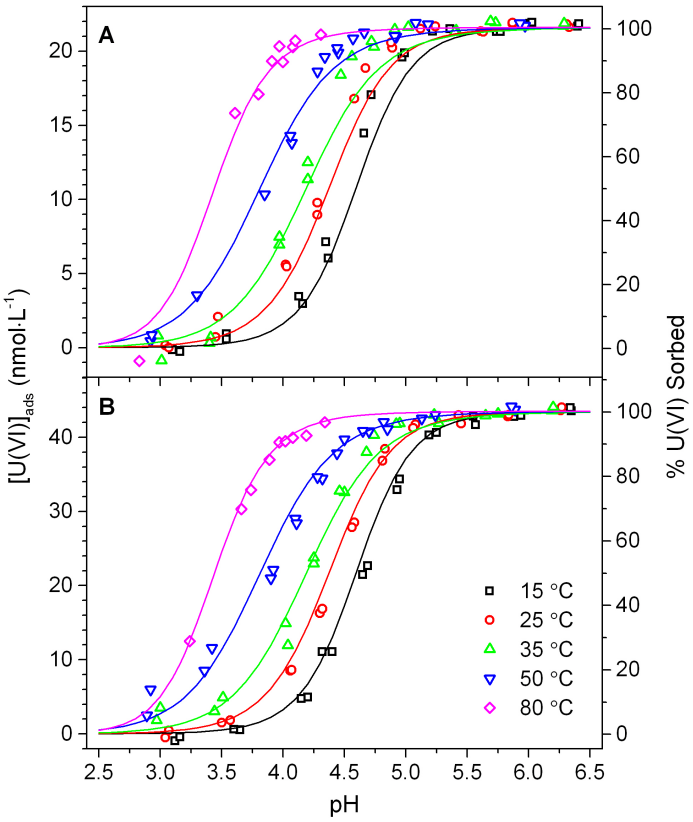

Figure 6.1: U(VI) sorption onto hematite as a function of pH and temperature for total U(VI) concentrations $(2.16 \pm 0.06) \times 10^{-8}$ M (A) and $(4.35 \pm 0.06) \times 10^{-8}$ M (B). Solid lines are the corresponding best fit surface complexation models (single-site DLM), which represent the following U(VI) surface complexes: $(\equiv \mathrm{FeOH})_2\mathrm{UO}_2^{2+}$ and $(\equiv \mathrm{FeO})_2\mathrm{UO}_2\mathrm{OH}^-$ at 15 and 25 ℃; $(\equiv \mathrm{FeOH})_2\mathrm{UO}_2^{2+}$ at 35 and 50 ℃; and $(\equiv \mathrm{FeO})_2\mathrm{UO}_2^0$ at 80 ℃. The WSOS/DF values, in order of increasing temperature, were 2.98, 0.91, 15.94, 5.02, and 0.04.

demonstrated that, in the presence of atmospheric CO_2, uranyl-carbonate surface complexes are not dominant until above pH ~ 6.[89,113] Therefore, we chose to exclude carbonate speciation in the final SCMs. Formation constants for the included aqueous U(VI) species were adjusted to each studied temperature using reported reaction enthalpies (Table 6.2) and the van't Hoff equation. All hematite characteristics and surface acidity constants were previously defined by Estes et al.,[102] with the exception of the acidity constants at 80 ℃, which we calculated using the van't Hoff equation. All reactions and equilibrium constants included in the final SCM are listed in Tables 6.1 – 6.3.

For each temperature, several possible U(VI) surface reactions were considered (listed in Table C.1) during SCM optimization. The reactions which yielded the best fits (i.e., lowest WSOS/DF) are listed in Table 6.3 with the corresponding calculated equilibrium constants. For all temperatures,

the best fits to our batch sorption data were given by one or more bidentate uranyl surface complexes (Fig. 6.1). At 15 and 25 ℃, the U(VI) sorption data were accurately modeled with two surface complexes, $(\equiv \mathrm{FeOH})_2\mathrm{UO}_2^{2+}$ and $(\equiv \mathrm{FeO})_2\mathrm{UO}_2\mathrm{OH}^-$ (Fig. 6.1). As temperature increased from 15 to 25 ℃, the contribution of $(\equiv \mathrm{FeO})_2\mathrm{UO}_2\mathrm{OH}^-$ to the overall uranyl surface speciation decreased (Fig. 6.3), and at 35 and 50 ℃, the sorption data were best fit using only $(\equiv \mathrm{FeOH})_2\mathrm{UO}_2^{2+}$. At the highest studied temperature, 80 ℃, the data were best fit using a fully de-protonated bidentate surface complex, $(\equiv \mathrm{FeO})_2\mathrm{UO}_2^0$.

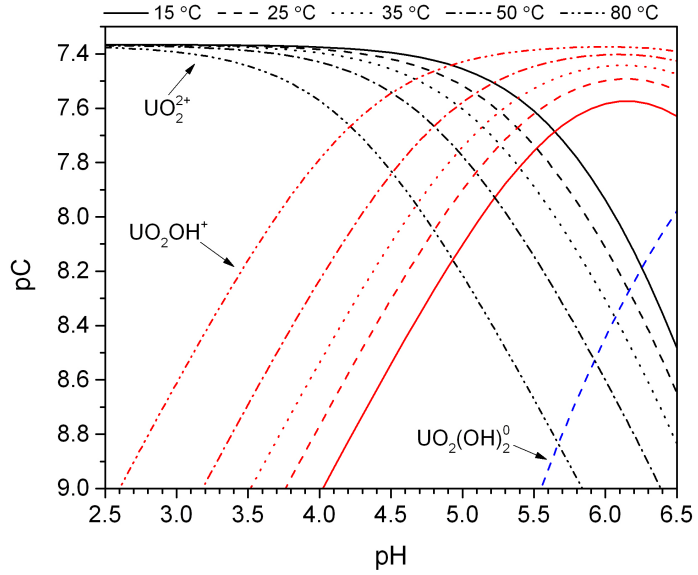

Figure 6.2: Aqueous speciation of U(VI) as a function of pH and temperature in the absence of CO_2. Modeled using Visual MINTEQ, with equilibrium constants given by Guillaumont et al.[21] The modeling conditions ($[\mathrm{U(VI)}]_{\mathrm{tot}} = 4.35 \times 10^{-8}$ M, $I = 0.01$ M NaCl) were equivalent to the batch sorption study with a higher total U(VI) concentration (system B). The enthalpy value for the second hydrolysis product is not defined; therefore, only the 25 ℃ model is shown.

6.3.1.3 Thermodynamic Parameter Quantification: van't Hoff Enthalpy

Quantifying reaction enthalpies using the van't Hoff approach requires the availability of formation constants defined for three or more temperatures. Because the SCM predicted a change in U(VI) surface speciation as temperature increased, we were only able to use the van't Hoff approach to quantify the enthalpy for the formation of $(\equiv \mathrm{FeOH})_2\mathrm{UO}_2^{2+}$. A plot of the $(\equiv \mathrm{FeOH})_2\mathrm{UO}_2^{2+}$ formation constants as a function of inverse temperature (i.e., a van't Hoff plot) is given in Appendix C (Fig. C.2). A least-squares linear regression indicated that this data set deviated from linearity,

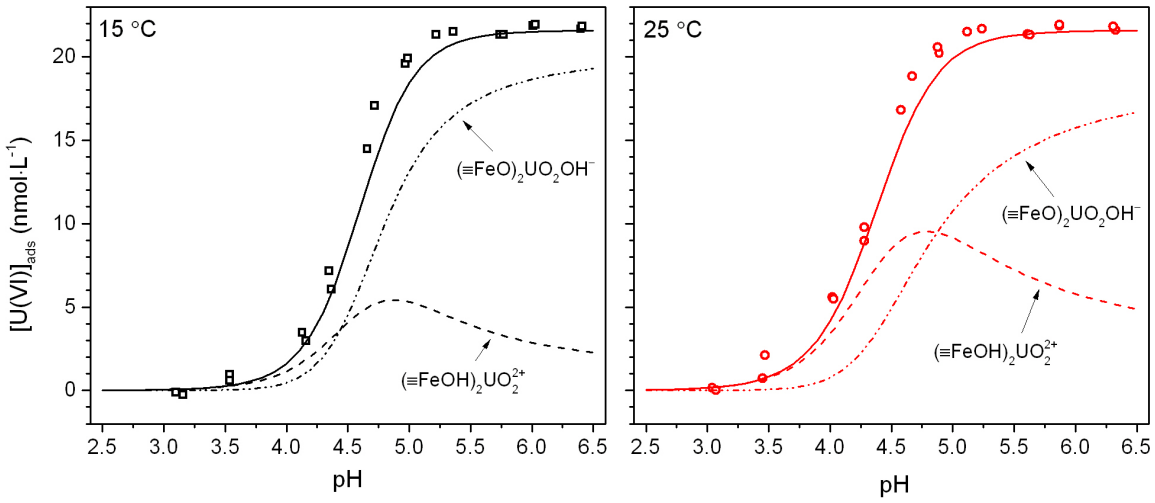

Figure 6.3: Distribution of U(VI) surface complexes at 15 and 25 ℃ for batch sorption system A ($[\mathrm{U(VI)}]_{\mathrm{tot}} = (2.16 \pm 0.06) \times 10^{-8}$ M). Solid lines are the total SCM (i.e., sum of $((\equiv\mathrm{FeOH})_2\mathrm{UO}_2^{2+}$ and $(\equiv \mathrm{FeO})_2\mathrm{UO}_2\mathrm{OH}^-$. A similar surface complex distribution was observed at 15 and 25 ℃ in system B ($[\mathrm{U(VI)}]_{\mathrm{tot}} = (4.35 \pm 0.06) \times 10^{-8}$ M).

which suggests that the enthalpy for the formation of $(\equiv \mathrm{FeOH})_2\mathrm{UO}_2^{2+}$ is not constant over the studied temperature range (i.e., $\Delta C_p \neq 0$). Therefore, we calculated the enthalpy and heat capacity for the formation of $(\equiv\mathrm{FeOH})_2\mathrm{UO}_2^{2+}$ using the extended van't Hoff equation[9]:

$$\log K - \log K^\circ = \left[\frac{\Delta_r H_7 - T^\circ \Delta C_{p,7}}{\ln 10 \cdot R} \cdot \left(\frac{1}{T^\circ} - \frac{1}{T}\right)\right] + \left[\frac{\Delta C_{p,7}}{R} \cdot \log \frac{T}{T^\circ}\right] \tag{6.4}$$

where $\log K$ is the $(\equiv\mathrm{FeOH})_2\mathrm{UO}_2^{2+}$ formation constant at each temperature, $\log K^\circ$ is the formation constant for $(\equiv\mathrm{FeOH})_2\mathrm{UO}_2^{2+}$ at 25 ℃, $\Delta_r H_7$ is the reaction enthalpy at 25 ℃, $\Delta C_{p,7}$ is the change in heat capacity at 25 ℃, T is the absolute temperature, T° is the absolute reference temperature (298.15 K), and R is the universal gas constant. Using a non-linear least-squares regression with simultaneous optimization of both thermodynamic parameters (Fig. 6.4), the calculated $\Delta_r H_7$ and $\Delta C_{p,7}$ are 35.5 ± 0.2 kJ mol^{-1} and -741 ± 14 J K^{-1} mol^{-1}. Additional thermodynamic parameters ($\Delta_r S_7$, $\Delta_r G_7$) derived from $\Delta_r H_7$ are listed in Table 6.4.

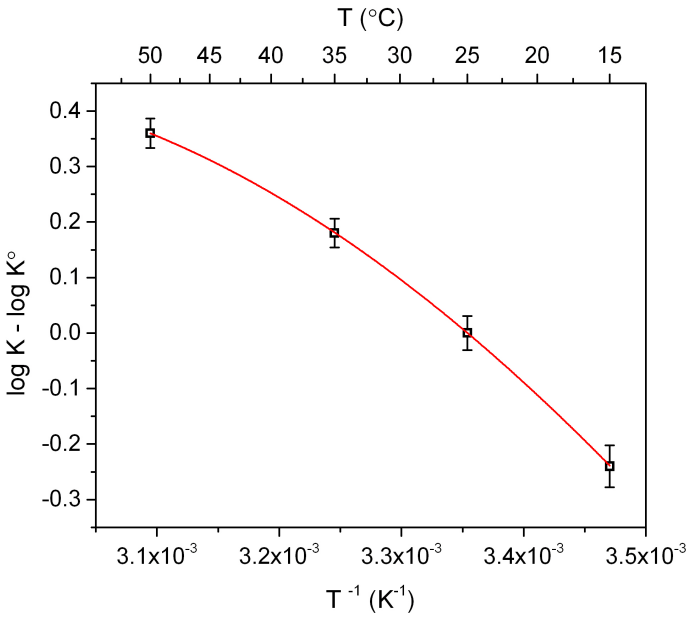

Figure 6.4: Extended van't Hoff plot using $\log K$ values for the surface complex $(\equiv \mathrm{FeOH})_2\mathrm{UO}_2^{2+}$. $\log K^\circ$ is the $(\equiv \mathrm{FeOH})_2\mathrm{UO}_2^{2+}$ formation constant at 25 ℃. The solid line is the non-linear fit with an adjusted R^2 equal to 0.999.

6.3.2 Isothermal Titration Calorimetry

6.3.2.1 Evolution of Heat and Surface Speciation

Relatively high concentrations of U(VI) (2.59×10^{-4} M) were necessary to produce measureable heat during the calorimetric titrations. However, equilibrium modeling with Visual MINTEQ indicated that all relevant U(VI) solid phases were undersaturated throughout the titrations. A total of three calorimetric titrations were performed, with each yielding a thermogram (typical example in Fig. 6.5) with well resolved exothermic peaks. Aqueous and surface speciation during the titrations were simulated using the SCM developed in Section 6.3.1.2.

As the calorimetric titrations progressed, the SCM (Table 6.3) indicated that pH and U(VI) sorption increased (Fig. 6.5), and that the formation of U(VI) surface complexes was greatest during the second half of the titration. The increased heat observed in the thermogram at $\sim$ 10 hr (Fig. 6.5) corresponds well with the predicted transition in U(VI) surface speciation from primarily $(\equiv \mathrm{FeOH})_2\mathrm{UO}_2^{2+}$ to primarily $(\equiv \mathrm{FeO})_2\mathrm{UO}_2\mathrm{OH}^-$. Because the formation of $(\equiv \mathrm{FeO})_2\mathrm{UO}_2\mathrm{OH}^-$ results in the release of three protons (Table 6.3), this increased heat may be due to additional proton neutralization (i.e., formation of $\mathrm{H_2O}$). The final measured suspension pH (7.6 ± 0.3) was in

fairly good agreement with the pH predicted by the SCM (8.9).

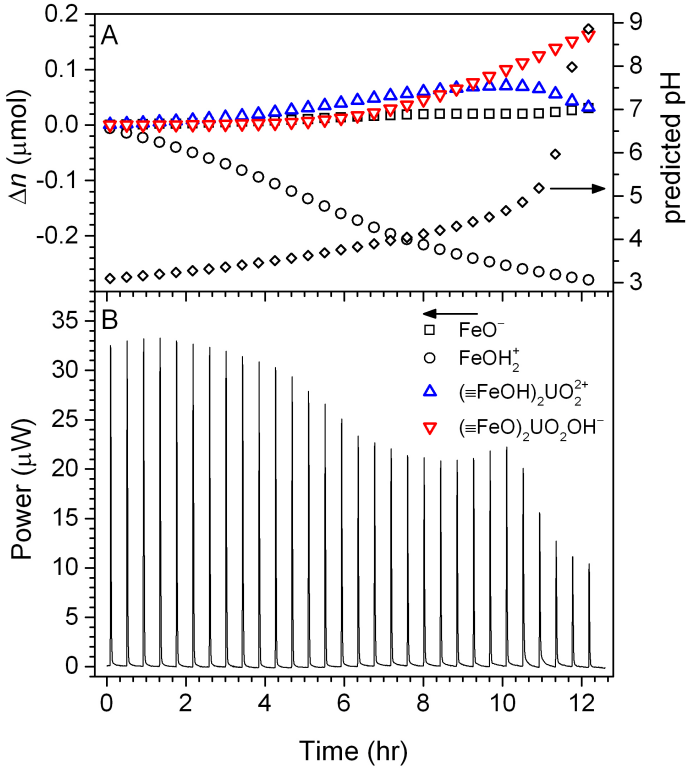

Figure 6.5: Change in pH (right y-axis) and hematite surface species (left y-axis) as a function of titration progress (A), and typical titration thermogram for U(VI) sorption onto hematite. Titration prarameters: $[\mathrm{U(VI)}]_0 = 2.59 \times 10^{-4}$ M, $[\alpha\text{–}\mathrm{Fe_2O_3}] = 5.14$ g L^{-1}, $I = 0.01$ M NaCl, $T = 25$ ℃, titrant = 0.01 M NaOH, injection volume = 4.97 μL.

6.3.2.2 Thermodynamic Parameter Quantification: Calorimetric Enthalpy

From the calorimetric titration data, the enthalpy of formation for both $(\equiv\mathrm{FeOH})_2\mathrm{UO_2^{2+}}$ ($\Delta_r H_7$) and $(\equiv\mathrm{FeO})_2\mathrm{UO_2OH^-}$ ($\Delta_r H_7$) were calculated by fitting $Q_{T,meas.}$ (for all titrations simultaneously) as a function of moles of product formed from each reaction listed in Tables 6.1 – 6.3 (25 ℃ only). Reaction enthalpies for the formation of both surface complexes were optimized simultaneously. The cumulative enthalpy plot and resulting fit are shown in Fig. 6.6 as a function of the formation of U(VI) surface species expected at 25 ℃. The calculated enthalpies for the formation of $(\equiv\mathrm{FeOH})_2\mathrm{UO_2^{2+}}$ and $(\equiv\mathrm{FeO})_2\mathrm{UO_2OH^-}$ are 81.5 ± 3.9 kJ mol^{-1} and 102 ± 3 kJ mol^{-1}, respectively. Additional thermodynamic parameters derived from these enthalpies are listed in Table 6.4.

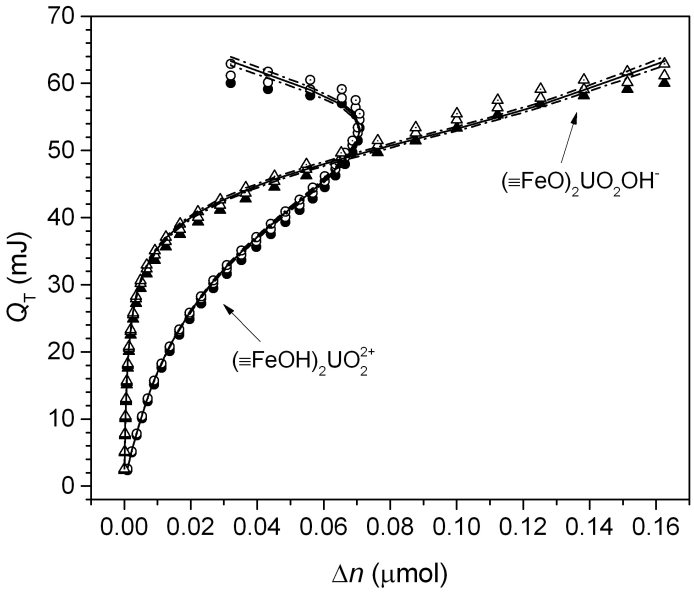

Figure 6.6: Cumulative enthalpy plot as a function of $(\equiv \mathrm{FeOH})_2\mathrm{UO}_2^{2+}$ and $(\equiv \mathrm{FeO})_2\mathrm{UO}_2\mathrm{OH}^-$ formation. Titration prarameters: $[\mathrm{U(VI)}]_0 = 2.59 \times 10^{-4}$ M, $[\alpha{-}\mathrm{Fe_2O_3}] = 5.14$ g L^{-1}, $I =$ 0.01 M NaCl, $T = 25$ ℃, titrant = 0.01 M NaOH, injection volume = 4.97 μL. Symbols are the measured cumulative heat for three titrations, and solid lines are the cumulative heat simultaneously calculated from all titration data (adjusted $R^2 = 0.997$); the dashed lines are the 95% upper and lower confidence limits.

6.4 Discussion

6.4.1 Comparison of Calculated van't Hoff and Calorimetric Enthalpies

As shown in Section 6.3.2.2, the resulting fit to the cumulative enthalpy plot is quite satisfactory (Fig. 6.6). However, the calculated $\Delta_r H_7$ is significantly higher than the same value calculated from the van't Hoff analysis (Table 6.4). There are two possible reasons for this disagreement. First, previous studies have demonstrated that U(VI) sorption onto iron oxy(hydr)oxides is non-linear over a wide range of U(VI) concentrations.[120,121] This non-linear isotherm behavior could indicate surface saturation or changes in uranyl surface speciation as equilibrium U(VI) concentrations increase. For this reason, our SCM, which was developed from batch experiments at much lower U(VI) concentrations, may not adequately describe U(VI) sorption onto hematite at the concentrations used in the calorimetric titrations.

Second, it is possible that there are chemical reactions that contribute to the measured cumulative heat that are not included in the SCM. Because we were unable to purge the am-

poule headspace during the calorimetric titrations, CO_2 dissolution and the subsequent formation of carbonate complexes may have contributed to the cumulative heat. However, the cumulative heat expected from these reactions after each injection is less than 1% of the heat expected from the other aqueous or surface reactions, suggesting that CO_2 dissolution is not responsible for the disagreement in calculated enthalpies. Electrolyte sorption onto the hematite surface may also contribute to the measured cumulative heat during each titration. However, we cannot account for these reactions with the DLM. Regardless of the reason for the discrepancy in calculated enthalpies, it is clear that the formation of both $(\equiv \mathrm{FeOH})_2\mathrm{UO}_2^{2+}$ and $(\equiv \mathrm{FeO})_2\mathrm{UO}_2\mathrm{OH}^-$ is endothermic. Thus, the thermodynamic driving force behind the strong sorption of U(VI) to hematite is due to a favorable entropy.

6.4.2 Comparison with Previous Sorption Studies

6.4.2.1 U(VI) Surface Complexation

Although many researchers have developed SCMs to describe U(VI) sorption onto various iron oxy(hydr)oxides, direct comparisons with our results are difficult because of differences between modeling approaches or experimental conditions. For example, Waite et al.[89] studied U(VI) sorption onto ferrihydrite in open systems and proposed a two-site, two-species model which included a bidentate uranyl complex, $(\equiv \mathrm{Fe}_{s,w}\mathrm{O}_2)\mathrm{UO}_2$, at pH < 6, and a bidentate uranyl-carbonate complex, $(\equiv \mathrm{Fe}_{s,w}\mathrm{O}_2)\mathrm{UO}_2\mathrm{CO}_3^{2-}$, at pH > 6.5. Although their SCM adequately modeled U(VI) sorption data for a variety of experimental conditions, it doesn't appear that they explored the full range of possible surface reaction stoichiometries. Zeng et al.[83] and Missana et al.[120] found that U(VI) sorption onto hematite and goethite, respectively, was best described with a bidentate uranyl surface complex. However, they also did not consider many alternative reactions in the development of their SCMs. Jang et al. developed a SCM using isotherm data for U(VI) sorption onto hydrous ferric oxide (HFO) at several circumneutral pH values.[121] Because their model was developed from these neutral pH isotherm data where U(VI) concentrations were ~ 1 μM, their model required monodentate and bidentate uranyl surface complexes, as well as aqueous and surface polynuclear uranyl complexes. Wazne et al. also used monodentate uranyl surface complexes to describe U(VI) sorption onto ferrihydrite in experiments where total U(VI) concentrations were $\sim 4 \times 10^{-6}$ M.[113] Neither polynuclear uranyl complexes nor monodentate uranyl surface complexes (generally consid-

ered a less favorable surface binding configuration) are expected in our batch sorption experiments where U(VI) concentrations are less than 5×10^{-8} M.

Perhaps the most thoroughly developed SCM comes from Hiemstra et al.,[114] who used the CD-MUSIC model to fit 168 experimental data points collected from the literature for U(VI) sorption onto ferrihydrite. Allowing only inner-sphere uranyl surface complexation at the singly coordinated terminal oxygen sites on the edges of Fe octahedra, they considered five possible uranyl surface complexes for CO_2-free systems. The surface reactions that best described the cumulative sorption data were given by $(\equiv \mathrm{FeOH})_2\mathrm{UO}_2$, $(\equiv \mathrm{FeOH})_2\mathrm{UO}_2\mathrm{OH}$, and $(\equiv \mathrm{FeOH})_2\mathrm{UO}_2(\mathrm{OH})_2$, where the net charge imparted to the electrical double layer (EDL) for each species was +2, +1, and 0, respectively. Furthermore, Hiemstra et al. stated that $(\equiv \mathrm{FeOH})_2\mathrm{UO}_2\mathrm{OH}$ was the most important surface species, based on the standard deviation of the calculated equilibrium constant. In a similar manner, we also considered many possible surface reaction stoichiometries in our SCM and determined that $(\equiv \mathrm{FeOH})_2\mathrm{UO}_2^{2+}$ and $(\equiv \mathrm{FeO})_2\mathrm{UO}_2\mathrm{OH}^-$ gave the best fit to our U(VI) sorption data at 25 ℃. Because we used a single-site DLM to describe our data, we were not able to distinguish the location of charge within the EDL, or to specify uranyl coordination to specific surface sites (e.g., $\equiv \mathrm{FeOH}^{-1/2}$, $\equiv \mathrm{Fe_3O}^{-1/2}$, etc.). However, we can make some comparisons with the SCM developed by Hiemstra et al.[114] First, the uranyl surface complexes in our 25 ℃ model compare well with the complexes suggested by Hiemstra et al.,[114] although we find that the hydrolyzed surface species $(\equiv \mathrm{FeO})_2\mathrm{UO}_2\mathrm{OH}^-$ is somewhat less important based on both the standard deviation of the $\log K$ value (Table 6.3) and percent speciation (Fig. 6.3). Second, our SCM suggests that the average net charge imparted to the EDL over the studied pH range, based on the relative concentrations of each complex at each data point, is +0.7 , which is close to the +1 charge of the dominant surface complex in the Hiemstra et al. model, $(\equiv \mathrm{FeOH})_2\mathrm{UO}_2\mathrm{OH}$. The agreement we find between our model and the Hiemstra et al.[114] model gives us confidence that our SCM is reasonable, and therefore we can use it to better understand the thermodynamics of U(VI) sorption onto hematite.

6.4.2.2 Temperature-Dependent Surface Speciation

Ridley et al. previously reported that Nd(III) hydrolysis at the rutile surface increased with increasing temperature.[92] From their results, and based on aqueous uranyl speciation models, which indicate that uranyl hydrolysis increases with increasing temperature (Fig. 6.2), one might expect the percentage of hydrolyzed uranyl-hematite surface complexes to also increase with increasing

temperature. However, this was not the trend observed in our modeling results. Instead, we observed a change in speciation from a combination of $(\equiv \mathrm{FeOH})_2\mathrm{UO}_2^{2+}$ and $(\equiv \mathrm{FeO})_2\mathrm{UO}_2\mathrm{OH}^-$ at low temperatures, to only $(\equiv \mathrm{FeOH})_2\mathrm{UO}_2^{2+}$ at 35 and 50 ℃, to $(\equiv \mathrm{FeO})_2\mathrm{UO}_2$ at the highest temperature studied. Upon further analysis, we find that the evolution of uranyl surface complexes reported here is consistent with the expected increase in negative surface charge (i.e., increased concentration of $\equiv \mathrm{FeO}^-$) as temperature increases and the hematite pzc decreases.[102] In other words, as temperature and the distribution of negatively charged surface sites increase, electrostatic attraction favors sorption of the divalent UO_2^{2+} over the monovalent $\mathrm{UO}_2\mathrm{OH}^+$. Furthermore, because the dielectric constant of water decreases as temperature increases,[122] we expect greater aqueous destabilization of the more highly charged uranyl ion compared with $\mathrm{UO}_2\mathrm{OH}^+$, and, therefore, greater sorption of UO_2^{2+} than $\mathrm{UO}_2\mathrm{OH}^+$.

6.4.2.3 Sorption Enthalpy

Sorption enthalpies are expected to fluctuate based on the sorbent and analyte binding configuration. Despite this, the van't Hoff and calorimetric reaction enthalpies calculated for the formation of $(\equiv \mathrm{FeOH})_2\mathrm{UO}_2^{2+}$ (Table 6.4) are similar to the range reported ($\sim 4 - 70$ kJ mol^{-1}) for sorption of other divalent metals (e.g., Zn(II), Pb(II), Cu(II), Cd(II)) onto various minerals).[45,46] Additionally, Almazan-Torres et al. reported an enthalpy of 58 kJ mol^{-1} for U(VI) sorption onto the phosphate sites in zirconium oxophosphate,[3] which is similar to the van't Hoff enthalpy we calculated for the formation of $(\equiv \mathrm{FeOH})_2\mathrm{UO}_2^{2+}$. However, $\Delta_r H$ for the formation of both $(\equiv \mathrm{FeOH})_2\mathrm{UO}_2^{2+}$ and $(\equiv \mathrm{FeO})_2\mathrm{UO}_2\mathrm{OH}^-$ are less than the enthalpy we previously calculated for Eu(III) sorption onto hematite ($(\equiv \mathrm{FeO})_2\mathrm{Eu}^+$, $\Delta_r H = +131$ kJ mol^{-1}).[102] As will be discussed further in the next section, this larger sorption enthalpy may be due to a stronger interaction between Eu(III) and the hematite surface and a greater number of hydrating waters lost upon Eu(III) sorption relative to U(VI) sorption.

6.4.3 Thermodynamic Interpretation

As previously stated, the formation of inner-sphere surface complexes should proceed with some dehydration of the uranyl ion upon sorption.[31] Because dehydration will increase the total system disorder, yet also requires energy for bond breakage, dehydration is an endothermic, entropically favorable reaction.[13] On the other hand, the formation of outer-sphere surface complexes should not

require uranyl dehydration, such that sorption should be dominated by electrostatic attraction and will likely be exothermic.[13] For this reason, we infer from the calculated thermodynamic parameters (Table 6.4) that U(VI) sorption onto hematite results in the formation of inner-sphere surface complexes. In support of this finding, extended X-ray absorption fine structure (EXAFS) data also indicate that, in our studied pH range, U(VI) forms bidentate mononuclear or bidentate binuclear inner-sphere complexes on the surfaces of hematite,[55,83] ferrihydrite,[89,117,118] goethite,[116,119] and lepidocrocite.[116]

The enthalpy (+131 kJ mol^{-1}) and entropy (+439 J mol^{-1} K^{-1}) previously determined for Eu(III) sorption onto hematite[102] were significantly larger than the entropy or enthalpy determined in this work for either U(VI) surface complex (Table 6.4). From EXAFS data and computational modeling, we suggested that the large Eu(III) sorption entropy was due to the loss of approximately five H_2O molecules from the Eu(III) primary hydration sphere.[102] EXAFS and theoretical modeling have previously indicated that the aquo uranyl ion is coordinated to five H_2O molecules in the equatorial plane, for a total U−O coordination number (CN) of 7, including the di-oxo moiety.[123,124] EXAFS data from the sorption studies cited above suggest that the equatorial U−O CN is approximately five for U(VI) surface complexes, such that U(VI) is bound to two surface oxygen atoms and three H_2O molecules or OH^- ligands. Although the overall U(VI) CN does not change from the aquo uranyl ion to the sorbed complex, this data indicates that approximately two H_2O molecules are removed from the primary hydration sphere of the aqueous uranyl ion upon sorption to iron oxy(hydr)oxide surfaces. We therefore propose that the smaller sorption entropies of the U(VI) surface complexes compared with the Eu(III) surface complex result from the loss of fewer H_2O molecules from the uranyl hydration sphere. Additionally, Trivedi and Axe suggested that larger sorption enthalpies are indicative of greater bonding strength between sorbate and sorbent.[125] Therefore, the smaller sorption enthalpies of the uranyl surface complexes may indicate a weaker interaction between U(VI) and hematite compared with Eu(III) and hematite. Possibly due to steric hindrance induced from the uranyl di-oxo moiety, greater distances have been observed in EXAFS data between U and Fe ($\sim$ 3.4 Å)[e.g.,55,89] compared with Eu and Fe ($\sim$ 3.1 Å)[102] for bidentate mononuclear surface complexes, which further suggests a weaker interaction between U(VI) and the hematite surfaces.

6.4.4 Implications for U(VI) Environmental Transport

The results presented above indicate that U(VI) sorption onto hematite, and perhaps other iron oxy(hydr)oxides, will be favored at higher temperatures, which may result in decreased migration of U(VI) in hydrothermal environments. However, compared with Eu(III), the thermodynamics also imply that there is a weaker interaction between U(VI) and the hematite surface, and that fewer H_2O molecules are lost from the U(VI) hydration sphere upon sorption. We previously postulated that desorption of Eu(III) may be kinetically hindered due to the expected large activation energy of rehydration.[102] Similarly, rehydration may limit U(VI) desorption as well, though a lower activation energy is expected due to the weaker interaction of U(VI). Thus, U(VI) may exhibit greater desorption from environmental surfaces and possibly greater environmental transport relative to Eu(III).

6.5 Conclusions

Additional work is clearly needed to further examine U(VI) sorption thermodynamics in more complex systems, and to understand the role that dehydration will play on the environmental transport of uranium. However, overall, the data and analyses presented in this paper support the following statements:

1. the speciation of U(VI) on the hematite surface may be temperature dependent;
2. U(VI) sorption onto hematite is an endothermic, entropically favorable reaction, indicating that enhanced sorption onto solid surfaces may be observed in natural or engineered systems at elevated temperatures;
3. partial dehydration of the uranyl ion upon sorption results in the formation of inner-sphere surface complexes;
4. enthalpies and entropies for the formation of both U(VI)-hematite surface complexes are less than the enthalpy and entropy for the formation of a Eu(III)-hematite surface complex, possibly indicating a weaker interaction between U(VI) and the hematite surface.

While the qualitative conclusions discussed above help in the understanding of uranium geochemical behavior, quantification of the exact enthalpy and entropy of the reactions remains somewhat uncer-

tain. The combination of variable temperature sorption studies and isothermal titration calorimetry can be a powerful tool to understand radionuclide sorption reactions. However, the disagreement between sorption enthalpies determined from the van't Hoff equation and calorimetry in this work is concerning. Since the enthalpies determined from these two approaches were based on data with greatly different U(VI) concentrations ($\sim$ 4 orders of magnitude), future work will focus on examining potential changes in uranium speciation as a function uranium surface concentrations.

Table 6.1: Hematite characteristics and surface acidity constants.

	parameter		value	
i	reaction	T ℃	$\log K$	$\log K^{\ddagger}$
	pzc		7.36[a]	
	A_s, BET surface area ($m^2\ g^{-1}$)		30.7[a]	
	N_s, site density (10^{18} sites m^{-2})		4.28[a]	
	$N^{\dagger}$, molar site density (10^{-6} mol m^{-2})		7.11	
	C_s, solid phase concentration (g L^{-1}) [batch expts. only]		0.51	
1	K_w°	15	−14.34[b]	
	$H_2O \rightleftharpoons H^+ + OH^-$	25	−13.99[b]	
	$\Delta_r H_1 = 55.8$ kJ mol^{-1} [c]	35	−13.68[b]	
		50	−13.26[b]	
		80	−12.60[b]	
2	K_+	15	6.39[d]	6.51[a,e]
	$\equiv FeOH + H^+ \rightleftharpoons \equiv FeOH_2^+$	25	6.19[d]	6.31[a,e]
	$\Delta_r H_2 = -32.2$ kJ mol^{-1} [a]	35	6.01[d]	6.13[a,e]
		50	5.75[d]	5.87[a,e]
		80	5.31[f]	5.43[e]
3	K_-	15	−8.30[d]	−8.18[a,e]
	$\equiv FeOH \rightleftharpoons \equiv FeO^- + H^+$	25	−8.11[d]	−7.99[a,e]
	$\Delta_r H_3 = 32.2$ kJ mol^{-1} [a]	35	−7.92[d]	−7.80[a,e]
		50	−7.67[d]	−7.55[a,e]
		80	−7.23[f]	−7.11[e]

[a] Estes et al.[102]
[b] $I = 0$ M; calculated from the standard density of water[84] according to Bandura and Lvov.[85]
[c] Martell et al.[109]
[d] Calculated by Estes et al.[102] using a single-site diffuse layer model (DLM); $I = 0.01$ M NaCl; referenced to the 1.0 M standard state.
[e] Referenced to the site occupancy standard state,[69] and calculated with the equation: $\log K^{\ddagger} = \log K + \log \frac{N_s A_s}{N^{\ddagger} A^{\ddagger}}$, where $N^{\ddagger}$ and $A^{\ddagger}$ are the theoretical site density (10×10^{18} sites m^{-2}) and surface area (10 $m^2\ g^{-1}$) suggested by Sverjensky.[69]
[f] $\log K_+$ and $\log K_-$ at 80 ℃ were calculated using the van't Hoff equation, the $\log K_+$ and $\log K_-$ values at 25 ℃, and the protonation ($\Delta_r H_2$) and de-protonation ($\Delta_r H_3$) enthalpies listed in this table.

Table 6.2: U(VI) reactions and equilibrium constants used for surface complexation modeling.

	parameter		value
i	reaction	T ℃	$\log K$
4	${}^*\beta_{1,1}$	15	-5.51^a
	$UO_2^{2+} + H_2O \rightleftharpoons UO_2OH^+ + H^+$	25	-5.25^b
	$\Delta_r H_4 = 43.46$ kJ mol^{-1} [c]	35	-5.00^a
		50	-4.66^a
		80	-4.06^a
5	${}^*\beta_{2,1}$	15	-12.15^d
	$UO_2^{2+} + H_2O \rightleftharpoons UO_2(OH)_2 + 2H^+$	25	-12.15^b
		35	-12.15^d
		50	-12.15^d
		80	-12.15^d
6	$K_{UO_2Cl^+}$	15	0.12^a
	$UO_2^{2+} + Cl^- \rightleftharpoons UO_2Cl^+$	25	0.17^b
	$\Delta_r H_6 = 8$ kJ mol^{-1} [b]	35	0.22^a
		50	0.28^a
		80	0.39^a

[a] $I = 0$ M; $\log K$ values for aqueous uranyl reactions at 15, 35, 50, and 80 ℃ were calculated using the van't Hoff equation, the $\log K$ values at 25 ℃, and the reaction enthalpies listed in this table.

[b] $I = 0$ M; Guillaumont et al.[21]

[c] $\Delta_r H_4$ was calculated from the formation enthalpies ($\Delta_f H_m^\circ$) given by Guillaumont et al.,[21] for the species UO_2^{2+}, UO_2OH^+, and H_2O (l). H^+ is the reference state, therefore $\Delta_f H_m^\circ$ (H^+) = 0 kJ mol^{-1}. The calculated $\Delta_r H_4$ agrees well with the value determined by Zanonato et al.,[105] (46.5 kJ mol^{-1}).

[d] The reaction enthalpy for ${}^*\beta_{2,1}$ is unknown. Therefore, the same $\log^* \beta_{2,1}$ was used for each experimental temperature.

Table 6.3: Best-fit U(VI) surface complexation reactions and equilibrium constants.

	parameter		value		
i	reaction	T ℃	$\log K$	$\log K_3$	$\log K^{\ddagger}$
7	K_{SC1}	15	12.77 ± 0.03^{a}	8.82^{b}	32.71^{c}
	$2 \equiv \mathrm{FeOH} + \mathrm{UO_2^{2+}} \rightleftharpoons (\equiv \mathrm{FeOH})_2\mathrm{UO_2^{2+}}$	25	$13.01 \pm 0.02^{a,d}$	9.06^{b}	32.95^{c}
		35	13.19 ± 0.01^{a}	9.24^{b}	33.13^{c}
		50	13.37 ± 0.02^{a}	9.42^{b}	33.31^{c}
		80	—	—	—
8	K_{SC2}	15	-8.22 ± 0.06^{a}	-12.17^{b}	11.72^{c}
	$2 \equiv \mathrm{FeOH} + \mathrm{UO_2^{2+}}$	25	$-7.82 \pm 0.09^{a,d}$	-11.77^{b}	12.12^{c}
	$\rightleftharpoons (\equiv \mathrm{FeO})_2\mathrm{UO_2OH^-} + 3\mathrm{H^+}$	35	—	—	—
		50	—	—	—
		80	—	—	—
9	K_{SC3}	15	—	—	—
	$2 \equiv \mathrm{FeOH} + \mathrm{UO_2^{2+}} \rightleftharpoons (\equiv \mathrm{FeO})_2\mathrm{UO_2} + 2\mathrm{H^+}$	25	—	—	—
		35	—	—	—
		50	—	—	—
		80	1.43 ± 0.04^{a}	-2.52^{b}	21.37^{c}

[a] Calculated using a single-site DLM and referenced to the 1.0 M standard state; I = 0.01 M NaCl. The exponent for ≡FeOH was defined as 2 in both the FITEQL mass balance and mass action expressions. As such, the $\log K$ values determined here for the U(VI) surface complexation reactions are dependent on solid phase concentration. To apply our SCM, researchers should use the $\log K_3$ values as described in note *b* below.

[b] Referenced to the mole fraction standard state as suggested by Wang and Giammar,[68] and calculated with the equation: $\log K_3 = \log K + \log(N^{\dagger} A_s C_s)$. Researchers that wish to use our SCM can directly input the $\log K_3$ values into modeling software which implements the mole fraction standard state. When using modeling software which implements the 1.0 M standard state (e.g., FITEQL), researchers should convert the $\log K_3$ into $\log K$ values using the above equation and the molar site density, specific surface area, and solid phase concentration specific to their reaction conditions.

[c] Referenced to the site occupancy standard state,[69] and calculated with the equation: $\log K^{\ddagger} = \log K + \log\left(\frac{(N_s A_s)^2 \cdot C_s}{N^{\ddagger} A^{\ddagger}}\right)$, where $N^{\ddagger}$ and $A^{\ddagger}$ are the theoretical site density (10×10^{18} sites $\mathrm{m^{-2}}$) and surface area (10 $\mathrm{m^2\ g^{-1}}$) suggested by Sverjensky.[69]

[d] The $\log K$ values were corrected for the hematite concentrations used in the calorimetric titrations (C_s = 5.14 g $\mathrm{L^{-1}}$) as described in note *b* above. The corrected $\log K$ values for formation of $(\equiv \mathrm{FeOH})_2\mathrm{UO_2^{2+}}$ and $(\equiv \mathrm{FeO})_2\mathrm{UO_2OH^-}$ were 11.998 and –8.832, respectively.

Table 6.4: Calculated thermodynamic parameters for U(VI) sorption onto hematite.[a]

	$\Delta_r G_i$[b] (kJ mol^{-1})	$\Delta_r H_i$ (kJ mol^{-1})	$\Delta_r S_i$[c] (J mol^{-1} K^{-1})	$\Delta_r C_{p,i}$ (J mol^{-1} K^{-1})
$(i = 7)$ $2 \equiv\mathrm{FeOH} + \mathrm{UO_2^{2+}} \rightleftharpoons (\equiv\mathrm{FeOH})_2\mathrm{UO_2^{2+}}$				
vH	-74.3 ± 0.1	$+35.5 \pm 0.2$	$+368 \pm 1$	-741 ± 14
cal.	-74.3 ± 0.1	$+81.5 \pm 3.9$	$+522 \pm 13$	—
$(i = 8)$ $2 \equiv\mathrm{FeOH} + \mathrm{UO_2^{2+}} \rightleftharpoons (\equiv\mathrm{FeO})_2\mathrm{UO_2OH^-} + 3\mathrm{H^+}$				
cal.	$+44.6 \pm 0.5$	$+102 \pm 3$	$+193 \pm 9$	—

[a] All values are for 25 ℃ and $I = 0.01$ M NaCl; "*vH*" indicates values derived from the van't Hoff analysis, "*cal.*" indicates values derived from ITC.
[b] Calculated from: $\Delta_r G_i = -RT \cdot \ln K$, where T is 298.15 K.
[c] Calculated from: $\Delta_r G_i = \Delta_r H_i - T\Delta_r S_i$, where T is 298.15 K.

Chapter 7

A Comparison of the Thermodynamics of Np(V), Th(IV), and Pu(IV) Sorption onto Hematite*

Abstract

Using multi-temperature batch sorption experiments and surface complexation modeling, we have studied the thermodynamics of Np(V), Th(IV), and Pu(IV) sorption onto hematite (α–Fe_2O_3). Np(V) experiments (0.5 g L^{-1} α–Fe_2O_3, I = 0.01 M NaCl, 10^{-8} M $Np(V)_{tot}$) were conducted over the pH range 3 to 8 at 15, 25, 35, and 50 ℃, and Th(IV) and Pu(IV) sorption experiments (0.58 g L^{-1} α–Fe_2O_3, I = 0.01 M NaCl, 10^{-8} M $Th(IV)/Pu(IV)_{tot}$) were conducted over the pH range 1.5 to 5.5 at 15, 25, 35, 50, and 65 ℃. Surface complexation modeling with the diffuse layer model (DLM) indicated that Np(V) and Th(IV) sorption onto hematite at all temperatures was best described with monodentate unhydrolyzed surface complexes, while Pu(IV) sorption onto hematite

*This chapter has been prepared for submission to *Geochimica et Cosmochimica Acta* with authors Shanna L. Estes and Brian A. Powell. Each author contributed the following: (1) Shanna L. Estes performed all batch sorption and calorimetric experiments, performed all associated data analyses, and wrote the complete manuscript; (2) Brian A. Powell secured research funding, assisted with all data analyses, and reviewed the manuscript.

at 25 ℃ was best described as $Pu(OH)_x^{4-x}$ sorbed in a monodentate fashion. Neither Np(V) nor Th(IV) sorption increased with increasing temperature, suggesting that both sorption reactions were temperature independent. Additionally, calculated sorption enthalpies and entropies suggest that Np(V) and Th(IV) sorption onto hematite occurs via predominantly outer-sphere and both outer- and inner-sphere surface complexation, respectively. Pu sorption onto hematite increased slightly with increasing temperature, suggesting that inner-sphere complexation may dominate the Pu(IV) sorption mechanism. Attempts to fit the Pu(IV) sorption behavior with the surface complexation model derived from Th(IV) were unsuccessful.

7.1 Introduction

Decades of nuclear weapons production and testing have resulted in significant Pu contamination of soils, sediments, and groundwater at many U.S. Department of Energy (DOE) sites.[4] Although this contamination is primarily localized at these DOE sites, several researchers have reported long-distance Pu transport,[1,2,126] which represents a significant risk to future populations due to the radiological health hazards associated with Pu exposure.

Pu chemistry at the solid-water interface is perhaps one of the most important processes controlling Pu transport in the environment, and therefore, it is important to investigate this chemistry under environmentally relevant conditions. However, the influence of temperature on Pu sorption reactions has not been widely studied, and to our knowledge, only Lu et al.[42] have examined the effect of temperature on Pu sorption onto various minerals. This is unfortunate, because in addition to providing necessary data for empirically modeling actinide sorption behavior under the elevated temperature conditions expected in a geologic repository,[43] investigating these reactions over a range of temperatures can also yield important information regarding reaction mechanisms. For example, we previously demonstrated that Eu(III)[102] and U(VI) sorption onto hematite are endothermic, entropically driven reactions, which suggests that both Eu(III)[102] and U(VI) form inner-sphere complexes with the hematite surface and that some dehydration of these elements occurs. Yet, because Pu is extremely sensitive to changes in redox conditions, and because Pu can routinely exist in aqueous solutions as mixtures of Pu(III), Pu(IV), Pu(V), and Pu(VI),[127] the interpretation of experimental data can be difficult. For this reason, researchers commonly use Np(V) and Th(IV) as redox stable chemical analogs of Pu(V) and Pu(IV), repectively. To this end, the objectives of this work were to

examine the influence of temperature on Np(V), Th(IV), and Pu(IV) sorption onto hematite, and to compare the Np(V), Th(IV), and Pu(IV) data and surface complexation models in an effort to indentify the mechanisms responsible for the sorption of these actinides onto hematite.

7.2 Materials and Methods

7.2.1 Reagents

Hematite ($\alpha-Fe_2O_3$) synthesis and characterization are described by Estes et al.[102] $La(NO)_3 \cdot 6\,H_2O$ (99.9%, Alfa Aesar), $KMnO_4$ (99.5%, Mallinckrodt), NaCl (99%, BDH), $NaNO_2$ (101.5%, Mallinckrodt), H_2SO_4 (95.0–98.0%, EM Science), HF (47–51%, Fisher), HCl (37%, BDH Aristar Plus), HNO_3 (67–70%, BDH Aristar Plus), bis-(ethylhexyl)-phosphoric acid (HDEHP, 95%, Aldrich), 4-benzyol-3-methyl-1-phenyl-5-pyrazolone (PMBP, TCI), cyclohexane (>99%, Alfa Aesar), and standardized HCl (0.01, 0.1 N, Metrohm) and NaOH (0.01, 0.1 N, Metrohm) were used as received. Perkin Elmer Optiphase HiSafe 3 cocktail was used for all liquid scintillation counting (LSC). For Pu oxidation state analyses, PMBP (0.025 M) and HDEHP (0.5 M) solutions were prepared in cyclohexane and equilibrated with 1 M HCl for a minimum of 30 minutes, and a lanthanum stock solution containing 0.01 M $LaNO_3$, 0.8 M HNO_3, 0.25 M H_2SO_4, and 0.001 M $KMnO_4$ was prepared in ultrapure H_2O – these solutions were stored in amber glass bottles sealed with PTFE septa and screw caps. Neptunium calibration standards (in 2% HNO_3) and working solution #1 (WS1, 4.2×10^{-6} M Np(V) in 2% HNO_3) were prepared from a ^{237}Np NIST standard reference solution (SRM 4341). Thorium calibration standards (in 2% HNO_3) and working solution #2 (WS2, 6.45×10^{-5} M Th(IV) in 1 M HCl) were prepared by diluting a Th plasma standard (1,000 μg L^{-1} in 2% HNO_3, High Purity Standards). Working solution #3 (WS3, 1.51×10^{-6} M Pu(IV) in 1 M HCl) was prepared from a ^{238}Pu source solution (Eckert & Ziegler, source #1556-59) by evaporating an aliquot of the source solution to dryness and reconstituting in 1 M HCl three times, with a few crystals of $NaNO_2$ added to the final solution to oxidize or reduce any Pu(III) or Pu(V/VI), respectively. Solvent extraction and LaF_3 coprecipitation (see Sec. 7.2.3) confirmed that the oxidation state distribution in WS3 was > 98% Pu(IV). All experiments were prepared in ultrapure H_2O (resistivity > 18 MΩ cm, Millipore SuperQ).

7.2.2 Multi-Temperature Batch Sorption

Batch experiments were conducted in either 50 mL polypropylene (PP) centrifuge tubes (Np(V)) or 125 mL screw top polycarbonate (PC) Erlenmeyer flasks (Th(IV) and Pu(IV)). For the Np(V) experiments, 4 mL of a 5 g L^{-1} hematite suspension and 4 mL of 0.1 M NaCl were added to each PP tube and diluted to a total volume of 40 mL with ultrapure H_2O. Following this step, an aliquot of WS1 was added to each tube, and the pH of each suspension was adjusted using HCl or NaOH. For the Th(IV) and Pu(IV) experiments, hematite was added to each PC flask as the dry solid, and then suspended in 0.01 M NaCl. To hydrate the hematite, these suspensions were initially mixed for $\sim$ 48 hours before adding an aliquot of both WS2 and WS3 to each flask. Immediately after the working solution additions, the pH of each suspension was adjusted using HCl or NaOH. Although both Th(IV) and Pu(IV) were present in these suspensions, 100% sorption of both Th(IV) and Pu(IV) at the highest concentrations studied would represent $< 0.05\%$ surface coverage. Therefore, no competition between the two actinides are expected in these experiments. The final Np(V) suspensions contained 0.5 g L^{-1} hematite, $(2.09 \pm 0.03) \times 10^{-8}$ M Np(V), and 0.01 M NaCl, with pH ranging from 3 to $\sim$ 8. The final Th(IV)/Pu(IV) suspensions (prepared in duplicate) contained 0.58 g L^{-1} hematite, $(2.11 \pm 0.02) \times 10^{-8}$ M or $(4.23 \pm 0.05) \times 10^{-8}$ M Th(IV), $(3.88 \pm 0.01) \times 10^{-10}$ M or $(2.00 \pm 0.01) \times 10^{-9}$ M Pu(IV), and 0.01 M NaCl in a total volume of $\sim$ 60 mL, with pH ranging from $\sim$ 1.5 to 5.5. No attempts to exclude atmospheric CO_2 were made. Additionally, no pH adjustments were made in either the Np(V) or Th(IV)/Pu(IV) experiments after the initial preparation of the batch systems.

Immediately following preparation of the batch systems, all flasks or tubes were initially placed within a temperature controlled orbital shaker (VWR) at 15 ℃ – PP tubes were placed horizontally in secondary containment. After 3 days of mixing, the pH of each suspension was measured using a combination pH electrode with automatic temperature compensation (Thermo 9157BNMD), and the suspensions were sampled by removing a 1.5 mL homogenous aliquot from each. Sample aliquots were centrifuged at 22,065g for 30 min to sediment particles larger than $\sim$ 60 nm. For Np(V) and Th(IV) analyses, 1 mL or 0.5 mL of the supernatant was diluted with 9 mL of 2% HNO_3 and analyzed for total Np or Th by inductively-coupled plasma mass spectrometry (ICP-MS, Thermo X Series 2). For Pu(IV) analyses, 0.5 mL of the supernatant was mixed with 4 mL of Optiphase HiSafe 3 cocktail in a 6 mL polyethylene (PE) scintillation vial and analyzed

using liquid scintillation counting (LSC, 30 minute count time, Perkin Elmer Tri-Carb 2910). After 5 to 7 additional days of mixing, the suspensions were sampled a second time to verify sorption equilibrium of Np(V) or Th(IV). During this second sampling event, an additional 300 μL of the supernatant from select samples spanning the pH range of the Th(IV)/Pu(IV) batch experiments was collected for Pu oxidation state analysis, as described in Sec. 7.2.3. After the second sampling event, the reaction temperature was increased, and the entire sampling procedure was repeated to give Np(V) sorption data at 15, 25, 35, and 50 ℃, and Th(IV) and Pu(IV) sorption data at 15, 25, 35, 50, and 65 ℃.

7.2.3 Plutonium Oxidation State Analysis

The oxidation state of aqueous Pu was determined using a solvent extraction method adapted from Neu et al.[128] and LaF_3 coprecipitation.[129] For solvent extractions, an aliquot of the Pu containing sample was diluted to 1 mL with H_2O and 5 M HCl in a 1.5 mL PP centrifuge tube to give an aqueous solution with pH = 0. Following this step, 0.5 mL of either the PMBP or HDEHP cyclohexane solutions was added to each PP tube. The tubes were then immediately capped and mixed on a vortex mixer (VWR) for three minutes, and then centrifuged for 1.5 minutes at 4,600g (VWR Galaxy 5D) to quickly separate the phases. A 0.4 mL aliquot of both the organic and aqueous phases was then carefully removed and mixed with 4 mL of liquid scintillation cocktail and analyzed as above. For LaF_3 coprecipitation, an aliquot of each Pu containing sample (diluted with H_2O if necessary to give 0.5 mL total sample volume) was mixed with 1 mL of the lanthanum stock solution and 10 μL of concentrated HF in a 1.5 mL PP centrifuge tube. The tubes were mixed and centrifuged as described for the solvent extractions, and then 0.4 mL of the aqueous phase was analyzed using LSC as described above. To limit Pu oxidation state changes as much as possible, all extraction or coprecipitation procedures were generally completed (to the point of LSC analysis) within 5 to 7 minutes of initial sample collection. For these conditions, PMBP and HDEHP extract Pu(IV) and Pu(IV)/Pu(VI), respectively, from the aqueous phase, and both Pu(III) and Pu(IV) are coprecipitated with LaF_3, allowing quantification of the oxidation state distribution of Pu in our initial solutions or batch systems.

7.2.4 Surface Complexation Modeling

To describe Np(V), Th(IV), and Pu(IV) sorption onto hematite, surface complexation models (SCMs) were developed by fitting the batch sorption data at each temperature as a function of pH using a modified version of FITEQL 4.0.[64] FITEQL modifications are described by Estes et al.[102] For each SCM, the electrical double layer (EDL) was defined using a single-site diffuse layer model (DLM),[67] which was selected for comparison with earlier work and because it has few adjustable parameters. For the Th(IV) and Pu(IV) SCMs, data from experiments at both initial actinide concentrations were combined and fit simultaneously. A 5% relative error was assigned to all experimental data during SCM optimization. Activity corrections were performed in FITEQL with the Davies model, after adjusting the Davies A parameter to each experimental temperature.[9] Except where noted, the FITEQL goodness of fit parameter, the ratio of the weighted sum of squares to the degrees of freedom (WSOS/DF), was used to identify the best SCM for each data set. Calculated equilibrium constants are referenced to the 1.0 M standard state and are reported $\pm$ 1σ. To ease comparison with future modeling efforts, equilibrium constants are also reported referenced to the site-occupancy standard state, as suggested by Sverjensky.[69]

7.3 Results

7.3.1 Np(V) and Th(IV) Sorption onto Hematite

7.3.1.1 Effect of Temperature

Np(V) and Th(IV) sorption onto hematite increased sharply with increasing pH at all studied temperatures, and as expected based on the greater effective charge of Th(IV)[130] and thus greater electrostatic attraction to the hematite surface, the Th(IV) sorption edge occurred at a lower pH than the Np(V) sorption edge (Fig. 7.1). Compared with the Th(IV) data, the Np(V) sorption data contained significant scatter (Fig. 7.1). Because we do not expect any reduction of Np(V) to Np(IV) under our experimental conditions,[131] this data scatter suggests a relatively weak interaction between Np(V) and the hematite surface.

Increasing the reaction temperature from 15 to 50 ℃ did not significantly affect Np(V) sorption onto hematite (Fig. 7.1). For the Th(IV) experiments, the sorption edge shifted to lower pH as the reaction temperature increased from 15 to 65 ℃, regardless of initial Th(IV) concentra-

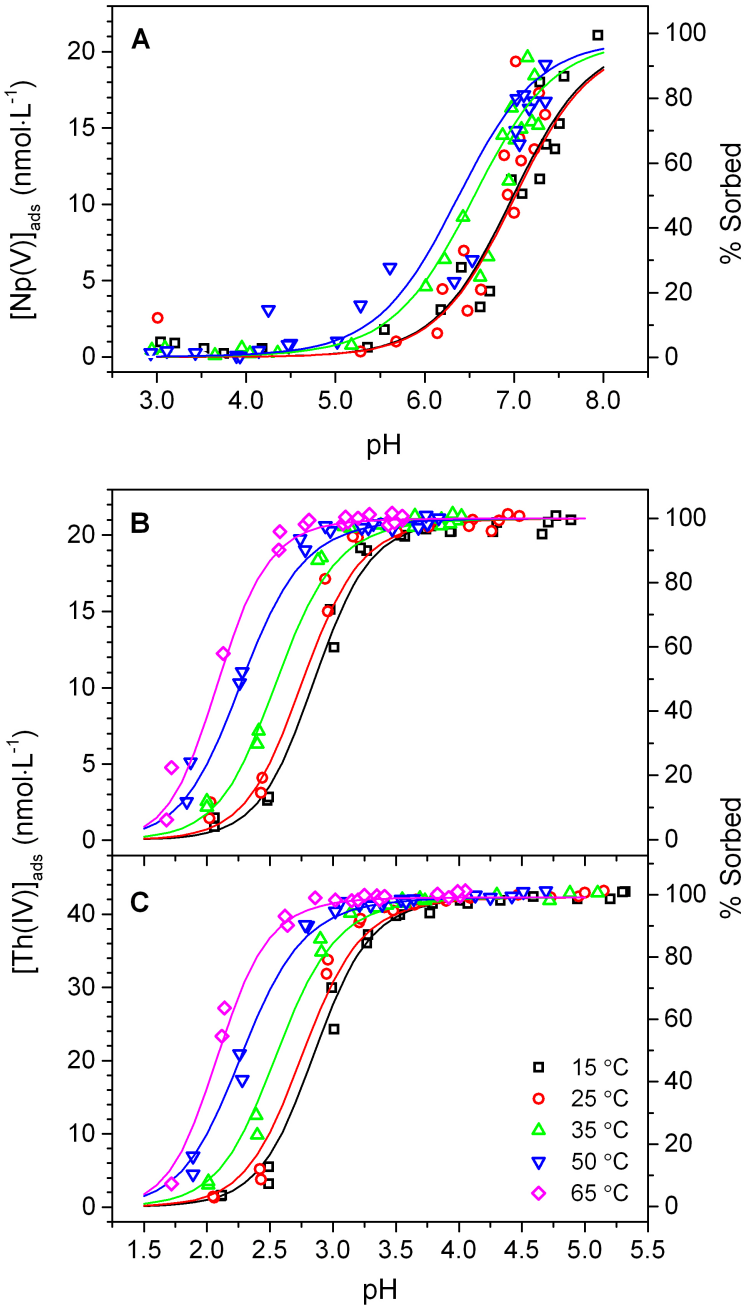

Figure 7.1: Np(V) and Th(IV) sorption onto hematite as a function of pH and temperature for a $[\mathrm{Np(V)}]_{\mathrm{tot}}$ of $(2.09 \pm 0.03) \times 10^{-8}$ M (A) and $[\mathrm{Th(IV)}]_{\mathrm{tot}}$ of $(2.11 \pm 0.02) \times 10^{-8}$ M (B) and $(4.23 \pm 0.05) \times 10^{-8}$ M (C). Solid lines are the corresponding surface complexation models (single-site DLM), which represent the following Np(V) and Th(IV) surface complexes: $\equiv\mathrm{FeONpO_2^0}$ at 15 and 25 ℃; $\equiv\mathrm{FeOHNpO_2^+}$ at 35 and 50 ℃; $\equiv\mathrm{FeOHTh^{4+}}$ at 15, 25, 35, and 50 ℃; and $\equiv\mathrm{FeOTh^{3+}}$ at 65 ℃. The WSOS/DF values, in order of increasing temperature, were: 20.32, 6.33, 11.84, and 17.91 for the Np(V) SCMs; and 3.70, 6.02, 1.15, 1.23, and 1.48 for the Th(IV) SCMs.

tion (Fig. 7.1). However, because K_w varies with temperature, the observed shift in the Th(IV) sorption edge is misleading, and does not necessarily indicate increased sorption. Re-plotting the Th(IV) sorption data as a function of "pH – $1/2\text{p}K_w$" (Fig. D.1), reveals that Th(IV) sorption does not change with increasing temperature. Therefore, it appears that the Np(V) and Th(IV) sorption reactions are temperature independent, at least for our experimental conditions, which is contradictory to the sorption behavior reported for other metals,[45,46] lanthanides,[47,54,92,93,102] and actinides.[3,42]

7.3.1.2 Surface Complexation Model Development

As illustrated in Fig. 7.2, the aqueous speciation of Np(V) is dominated by NpO_2^+ across the experimental pH range. The formation of NpO_2OH^0 was included in the final SCM, but concentrations of this species were generally insignificant in our batch systems. Although the formation of $NpO_2CO_3^-$ is significant above pH $\sim$ 7.5 (Fig. 7.2), including aqueous or surface neptunyl-carbonate complexes in the SCM did not improve our fit results. Additionally, Kohler et al. previously demonstrated that the presence of atmospheric CO_2 did not affect Np(V) sorption onto hematite at pH < 8.[132] Therefore, all carbonate species were excluded from the final Np(V) SCM. Similarly, all carbonate species were excluded from the final Th(IV) SCM based on the expected aqueous Th(IV) speciation (Fig. 7.2), which indicates that Th(IV)-carbonate complexes were not present at significant concentrations in the pH range of the Th(IV) batch experiments ($\sim$ 1.5 to 5.5). However, unlike Np(V), the Th(IV) aqueous speciation includes several Th(IV) hydrolysis products and $ThCl^{3+}$ (Fig. 7.2). Therefore, formation reactions for $ThOH^{3+}$, $Th(OH)_2^{2+}$, $Th(OH)_4^0$, and $ThCl^{3+}$ were included in the SCM. All aqueous reactions and associated formation constants used in the final Np(V) and Th(IV) SCMs are listed in Table 7.1. Unless otherwise noted, the formation constants at each temperature were calculated using available reaction enthalpies (Table 7.1) and the van't Hoff equation. All pertinent hematite parameters, which were determined by Estes et al.[102] are given in Table 7.2.

For both the Np(V)- and Th(IV)-hematite systems, many different surface reactions were considered during optimization of the SCM. At 15 and 25 ℃, the Np(V) sorption data were best fit (i.e., lowest WSOS/DF) using a monodentate de-protonated surface complex, $\equiv FeONpO_2^0$; while at 35 and 50 ℃, the data were best fit using a monodentate protonated surface complex, $\equiv FeOHNpO_2^+$ (Fig. 7.1). In contrast, the Th(IV) sorption data were best fit at 15, 25, 35, and 50 ℃ using a monodentate protonated surface complex, $\equiv FeOHTh^{4+}$ (Fig. 7.1). However, at 65 ℃, a bidentate

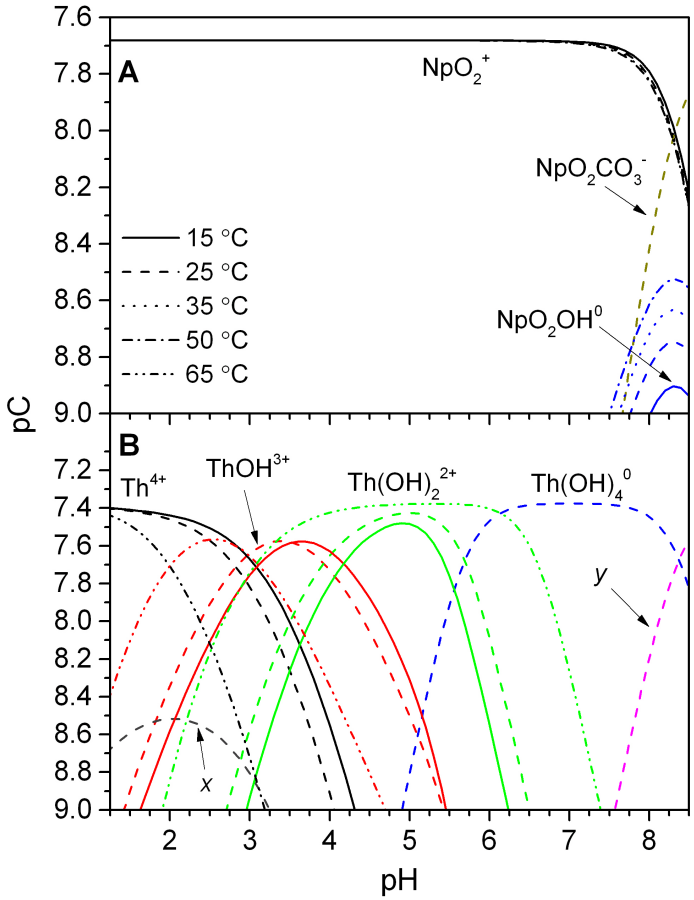

Figure 7.2: Aqueous speciation of Np(V) (A) and Th(IV) (B) as a function of pH and temperature in the presence of atmospheric CO_2 ($P_{CO_2} = 10^{-3.4}$ atm). Modeled using Visual MINTEQ, with equilibrium constants given by Guillaumont et al.,[21] Rao et al.,[23] and Rand et al.[133] The arrows x and y (B) indicate the Th(IV) species $ThCl^{3+}$ and $Th(OH)_2(CO_3)_2^{2-}$, respectively. The modeling conditions ($[Np(V)]_{Ttot} = 2.09 \times 10^{-8}$ M or $[Th(IV)]_{tot} = 4.23 \times 10^{-8}$ M, $I = 0.01$ M NaCl) were equivalent to the batch sorption experiments. The enthalpies for $NpO_2CO_3^-$, $Th(OH)_4^0$, $ThCl^{3+}$, and $Th(OH)_2(CO_3)_2^{2-}$ are not defined; therefore, only models at 25 ℃ are shown. For simplicity, only 15, 25, and 65 ℃ models, which illustrate the speciation range expected for our experimental conditions, are shown for other Th(IV) species.

de-protonated surface complex, $(\equiv FeO)_2Th^{2+}$, fit the Th(IV) sorption data slightly better than a monodentate de-protonated surface complex, $\equiv FeOTh^{3+}$ (WSOS/DF = 1.35 vs. 1.48, respectively). It is not clear which surface complex best represents Th(IV) sorption onto hematite at 65 ℃. However, because the relative error in the calculated $\log K$ for $(\equiv FeO)_2Th^{2+}$ ($\log K = 12.38 \pm 0.04$) was $\sim 30\%$ greater than the relative error in the calculated $\log K$ for $\equiv FeOTh^{3+}$ ($\log K = 13.62 \pm 0.03$), we chose to model the Th(IV) sorption data at 65 ℃ with the monodentate surface complex. All surface complexation reactions and equilibrium constants chosen for the final Np(V) and Th(IV) SCMs at each temperature are listed in Table 7.3.

7.3.1.3 Sorption Thermodynamics

Because the best fit SCMs indicated a change in Np(V) surface speciation with increasing temperature, resulting in $\log K$ values at only two temperatures for each surface complex, it was not possible to use the van't Hoff relationship to calculate the Np(V) sorption enthalpy. However, changes in the $\log K$ values at each temperature (Table 7.3) for the formation of $\equiv FeONpO_2^0$ and $\equiv FeOHNpO_2^+$ are insignificant, suggesting that the enthalpies for both reactions ($\Delta_r H_9$ and $\Delta_r H_{10}$, respectively) are ≈ 0 kJ mol^{-1}. Sufficient data were available to approximate the enthalpy of Th(IV) sorption onto hematite using a van't Hoff plot (Fig. 7.3). However, the linear regression yielded a slope that was not significantly different than zero (ANOVA, $P = 0.05$), suggesting that the reaction enthalpy for the formation of $\equiv FeOHTh^{4+}$ ($\Delta_r H_{11}$) is also ≈ 0 kJ mol^{-1}. These sorption enthalpies are consistent with the absence of any temperature dependent changes in the Np(V) and Th(IV) sorption edges noted earlier (Sec. 7.3.1.1).

7.3.2 Pu(IV) Sorption onto Hematite

7.3.2.1 Effect of Temperature

Pu(IV) sorption onto hematite as a function of pH and temperature is shown in Fig. 7.4. This figure illustrates that: (1) sorption equilibrium was not reached at the first sampling event, as represented by significant differences between closed and open symbols, particularly at the higher pH values; (2) the Pu(IV) sorption edges are more shallow (i.e., sorption from 0 to 100% occurs over a wider pH range) than those observed for either Np(V) or Th(IV) (Fig. 7.1); and (3) there is significant scatter in the sorption data compared with the Th(IV) sorption data (Fig. 7.1). This anomalous sorption

Table 7.1: Aqueous reactions, equilibrium constants, and reaction enthalpies used to model Np(V) and Th(IV) sorption onto hematite at 15 to 65 ℃.

i	reaction	T ℃	$\log K^a$	T ℃	$\log K^a$
1	K_w°	15	-14.34^b	50	-13.26^b
	$H_2O \rightleftharpoons H^+ + OH^-$	25	-13.99^b	65	-12.91^b
	$\Delta_r H_1 = 55.8$ kJ mol^{-1} ^{c}	35	-13.68^b		
4	${}^*\beta_{1,1}$ (Np(V))	15	-9.17^c	50	-8.74^c
	$NpO_2^+ + H_2O \rightleftharpoons NpO_2OH + H^+$	25	-8.98^d		
		35	-8.85^c		
5	${}^*\beta_{1,1}$ (Th(IV))	15	-2.77^e	50	-1.90^e
	$Th^{4+} + H_2O \rightleftharpoons ThOH^{3+} + H^+$	25	-2.50^e	65	-1.58^e
	$\Delta_r H_5 = 44.2$ kJ mol^{-1} ^{f}	35	-2.25^e		
6	${}^*\beta_{2,1}$ (Th(IV))	15	-6.72^e	50	-5.04^e
	$Th^{4+} + 2\,H_2O \rightleftharpoons Th(OH)_2^{2+} + 2\,H^+$	25	-6.20^f	65	-4.42^e
	$\Delta_r H_6 = 85.7$ kJ mol^{-1} ^{f}	35	-5.71^e		
7	${}^*\beta_{4,1}$ (Th(IV))	15	-17.40^g	50	-17.40^f
	$Th^{4+} + 4\,H_2O \rightleftharpoons Th(OH)_4^0 + 4\,H^+$	25	-17.40^f	65	-17.40^f
		35	-17.40^f		
8	$K_{ThCl^{3+}}$	15	1.70^g	50	1.70^g
	$Th^{4+} + Cl^- \rightleftharpoons ThCl^{3+}$	25	1.70^f	65	1.70^g
		35	1.70^g		

[a] All equilibrium constants are for $I = 0$ M.
[b] Calculated from the standard density of water[84] according to Bandura and Lvov.[85]
[c] $\log K$ for neptunyl hydrolysis at 15, 35, and 50 ℃ was calculated from an exponential fit of $\log {}^*\beta_1^\circ$ [23] as a function of temperature.
[d] Rao et al.[23]
[e] $\log K$ values for aqueous Th(IV) reactions at 15, 35, 50, and 65 ℃ were calculated with the van't Hoff equation using the $\log K$ values at 25 ℃ and the reaction enthalpies listed in this table.
[f] Rand et al.[133]
[g] The reaction enthalpies for ${}^*\beta_{4,1}$ (Th(IV)) and $K_{ThCl^{3+}}$ are unknown. Therefore the same $\log {}^*\beta_{4,1}$ and $\log K_{ThCl^{3+}}$ were used for each experimental temperature.

Table 7.2: Hematite characteristics and surface acidity constants

	parameter		value	
i	reaction	T ℃	$\log K$	$\log K^{\ddagger}$
	pzc		7.36[a]	
	A_s, BET surface area ($m^2\ g^{-1}$)		30.7[a]	
	N_s, site density (10^{18} sites m^{-2})		4.28[a]	
	$N^{\dagger}$, molar site density (10^{-6} mol m^{-2})		7.11	
	C_s, solid phase concentration (g L^{-1}) [Np(V) expts.]		0.51	
	C_s, solid phase concentration (g L^{-1}) [Th(IV)/Pu(IV) expt.]		0.58	
2	K_+	15	6.39[b]	6.51[a,c]
	$\equiv FeOH + H^+ \rightleftharpoons \equiv FeOH_2^+$	25	6.19[b]	6.31[a,c]
	$\Delta_r H_2 = -32.2$ kJ mol^{-1} [a]	35	6.01[b]	6.13[a,c]
		50	5.75[b]	5.87[a,c]
		65	5.52[d]	5.64[c]
3	K_-	15	−8.30[b]	−8.18[a,c]
	$\equiv FeOH \rightleftharpoons \equiv FeO^- + H^+$	25	−8.11[b]	−7.99[a,c]
	$\Delta_r H_3 = 32.2$ kJ mol^{-1} [a]	35	−7.92[b]	−7.80[a,c]
		50	−7.67[b]	−7.55[a,c]
		65	−7.44[d]	−7.32[c]

[a] Estes et al.[102]

[b] Calculated by Estes et al.[102] using a single-site diffuse layer model (DLM); $I = 0.01$ M NaCl; referenced to the 1.0 M standard state.

[c] Referenced to the site-occupancy standard state,[69] and calculated with the equation: $\log K^{\ddagger} = \log K + \log \frac{N_s A_s}{N^{\ddagger} A^{\ddagger}}$, where $N^{\ddagger}$ and $A^{\ddagger}$ are the theoretical site density (10×10^{18} sites m^{-2}) and surface area (10 $m^2\ g^{-1}$) suggested by Sverjensky.[69]

[d] $\log K_+$ and $\log K_-$ at 65 ℃ were calculated using the van't Hoff equation, the $\log K_+$ and $\log K_-$ values at 25 ℃ and the protonation ($\Delta_r H_2$) and de-protonation ($\Delta_r H_3$) enthalpies listed in this table.

Table 7.3: Best-fit Np(V) and Th(IV) surface complexation reactions and equilibrium constants

	parameter		value	
i	reaction	T ℃	$\log K$	$\log K^{\ddagger}$
9	K_{SC1}	15	-2.93 ± 0.02^{a}	-2.81^{b}
	$\equiv\text{FeOH} + \text{NpO}_2^+ \rightleftharpoons \equiv\text{FeONpO}_2 + \text{H}^+$	25	-2.95 ± 0.02^{a}	-2.83^{b}
		35	—	—
		50	—	—
		65	—	—
10	K_{SC2}	15	—	—
	$\equiv\text{FeOH} + \text{NpO}_2^+ \rightleftharpoons \equiv\text{FeOHNpO}_2^+$	25	—	—
		35	4.46 ± 0.03^{a}	4.58^{b}
		50	4.38 ± 0.02^{a}	4.50^{b}
		65	—	—
11	K_{SC3}	15	19.20 ± 0.02^{a}	19.32^{b}
	$\equiv\text{FeOH} + \text{Th}^{4+} \rightleftharpoons \text{FeOHTh}^{4+}$	25	19.03 ± 0.02^{a}	19.15^{b}
		35	19.12 ± 0.02^{a}	19.24^{b}
		50	19.21 ± 0.02^{a}	19.33^{b}
		65	—	—
12	K_{SC4}	15	—	—
	$\equiv\text{FeOH} + \text{Th}^{4+} \rightleftharpoons \equiv\text{FeOTh}^{3+} + \text{H}^+$	25	—	—
		35	—	—
		50	—	—
		65	13.62 ± 0.03^{a}	13.74^{b}

[a] Estes et al.[102]

[b] Calculated by Estes et al.[102] using a single-site diffuse layer model (DLM); $I = 0.01$ M NaCl; referenced to the 1.0 M standard state.

[c] Referenced to the site-occupancy standard state,[69] and calculated with the equation: $\log K^{\ddagger} = \log K + \log \frac{N_s A_s}{N^{\ddagger} A^{\ddagger}}$, where $N^{\ddagger}$ and $A^{\ddagger}$ are the theoretical site density (10×10^{18} sites m^{-2}) and surface area (10 m^2 g^{-1}) suggested by Sverjensky.[69]

[d] $\log K_+$ and $\log K_-$ at 65 ℃ were calculated using the van't Hoff equation, the $\log K_+$ and $\log K_-$ values at 25 ℃ and the protonation ($\Delta_r H_2$) and de-protonation ($\Delta_r H_3$) enthalpies listed in this table.

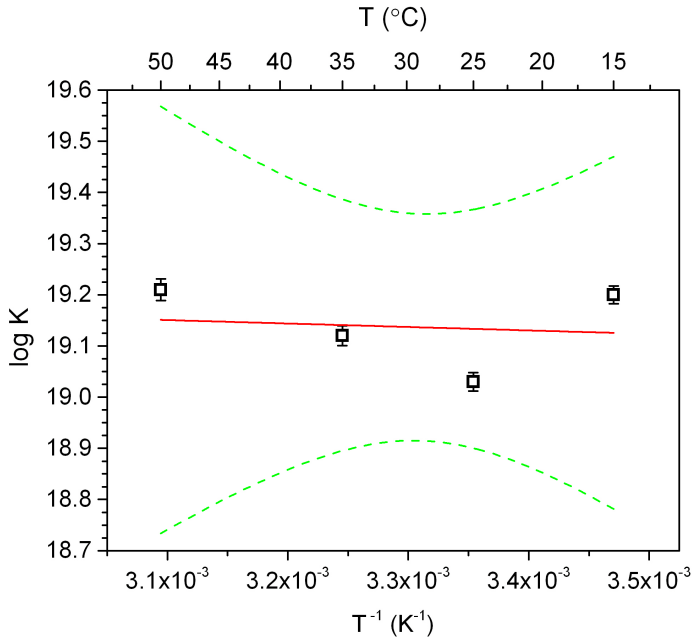

Figure 7.3: van't Hoff plot using $\log K$ values for the surface complex $\equiv$FeOHTh^{4+}. The solid line is the linear fit, which is not significantly different than zero (at the 0.05 level), and the dashed lines are the 95% confidence intervals.

behavior was likely due to changes in the oxidation state of aqueous phase Pu across the studied pH range and at each reaction temperature (Fig. 7.5).

As pH increases, some Pu(IV) oxidation, likely to Pu(V), is evident at 15 to 50 ℃ (Fig. 7.5). At 25 ℃, these oxidation state changes are consistent with the expected thermodynamic stabilities of Pu(III, IV, V, VI) under the experimental conditions.[e.g.,134] Interestingly, at 65 ℃, the aqueous phase Pu speciation in our batch experiments appears to reverse, such that oxidized Pu species become dominant at lower pH values compared to Pu(III/IV) (Fig. 7.5). Possible reasons for this oxidation state reversal are unknown, and warrant further investigation.

If we assume that sorption equilibrium was reached at the second sampling event, and plot this data as a function of "pH – 1/2pK_w" (Fig. D.2), Pu sorption onto hematite appears to increase with increasing temperature, which is consistent with previous observations by Lu et al.[42] However, because we do not have direct evidence that sorption equilibrium was achieved, and because there are known changes in the Pu oxidation state, it is not clear if this increased sorption is actually due to one or more endothermic sorption reactions.

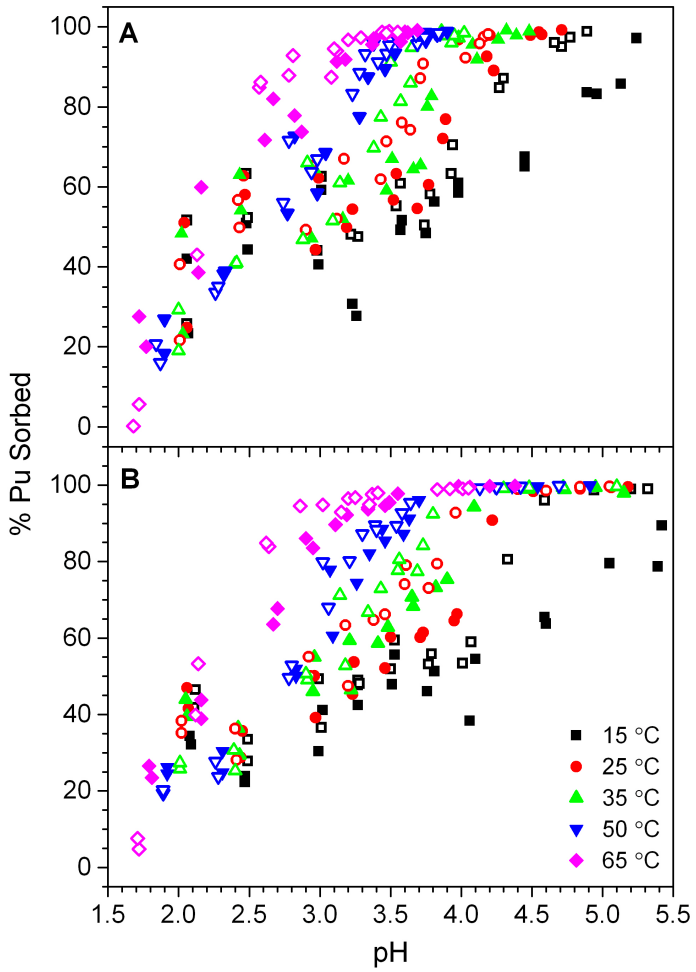

Figure 7.4: Pu(IV) sorption onto hematite as a function of pH and temperature for batch systems with [Pu(IV)]tot of $(3.88 \pm 0.01) \times 10^{-10}$ M (A) and $(2.00 \pm 0.01) \times 10^{-9}$ M (B). Errors, calculated from counting statistics, are $\pm 1\sigma$. Closed and open symbols represent data from the first and second sampling events, respectively.

7.3.2.2 Surface Complexation Model Development at 25 °C

Using data from the second sampling event, we developed a SCM to describe the observed Pu sorption onto hematite. However, because Pu(IV) hydrolysis constants are only available at 25 °C, we were only able to fit the sorption data at that temperature. We explored several combinations of surface reactions during SCM optimization, using the Th(IV) best fit monodentate protonated surface complex as a guide. Carbonate speciation was excluded from the SCMs because Pu-carbonate species are not expected in significant concentrations in the studied pH range.[135,136] For model development, we assumed that Pu was present as 100% Pu(IV) and that neither Pu oxidation

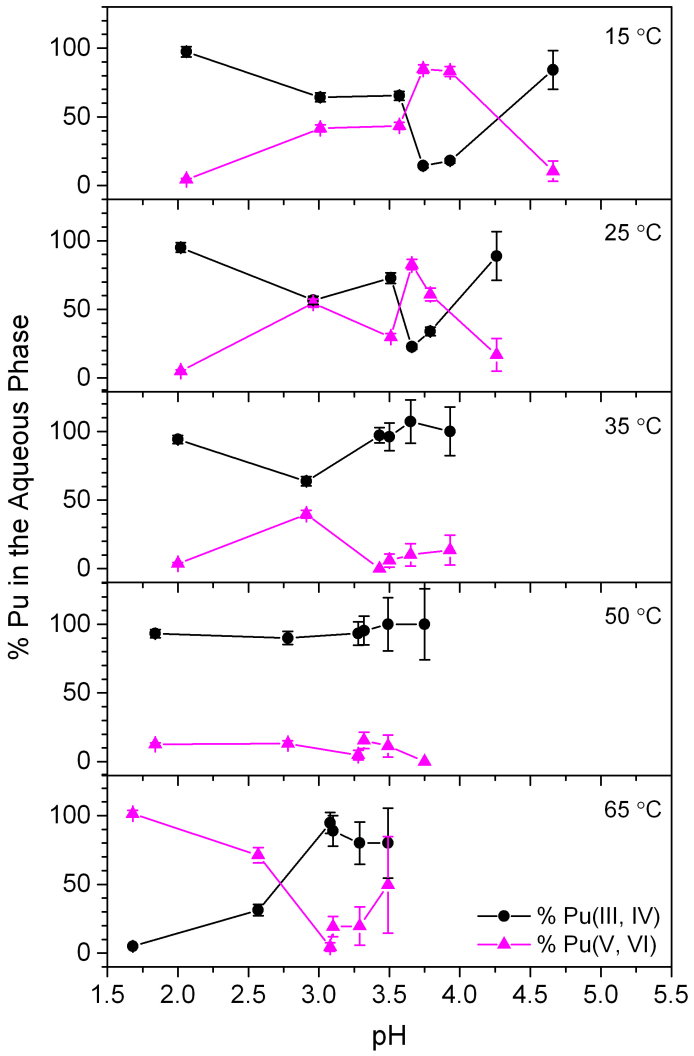

Figure 7.5: Pu oxidation state distribution in the aqueous phase as a function of pH and temperature for the batch systems with initial $Pu(IV)_{tot}$ concentrations of $(3.88 \pm 0.01) \times 10^{-10}$ M. Errors, calculated from counting statistics, are $\pm 1\sigma$. Similar oxidation state distributions were measured for batch systems with higher initial Pu(IV) concentrations (Fig. D.4). Pu(III,IV) concentrations are from solvent extraction with PMBP in cyclohexane, and agree well with results from LaF_3 coprecipitation. Pu(V/VI) concentrations are from coprecipitation with LaF_3.

nor reduction occurred. As several researchers have observed Pu(V) reduction to Pu(IV) in the presence of various pure and mixed mineral phases,[e.g.,33–35,41] and have suggested that Pu(IV) may be the thermodynamically favorable surface species, our assumption, that only Pu(IV) was present, may be reasonable for describing Pu surface reactions only. As clearly demonstrated in Fig. 7.5, a similar assumption cannot be made regarding the aqueous Pu speciation. The 25 ℃ data were best fit using a combination of three surface complexes, $\equiv FeOHPu(OH)_2^{2+}$, $\equiv FeOHPu(OH)_3^{+}$, and

$\equiv$FeOHPu$(OH)_4^0$ (Fig. 7.6). The relative importance of each surface complex is illustrated in Fig. 7.6, and the calculated equilibrium constants are given in Table 7.4.

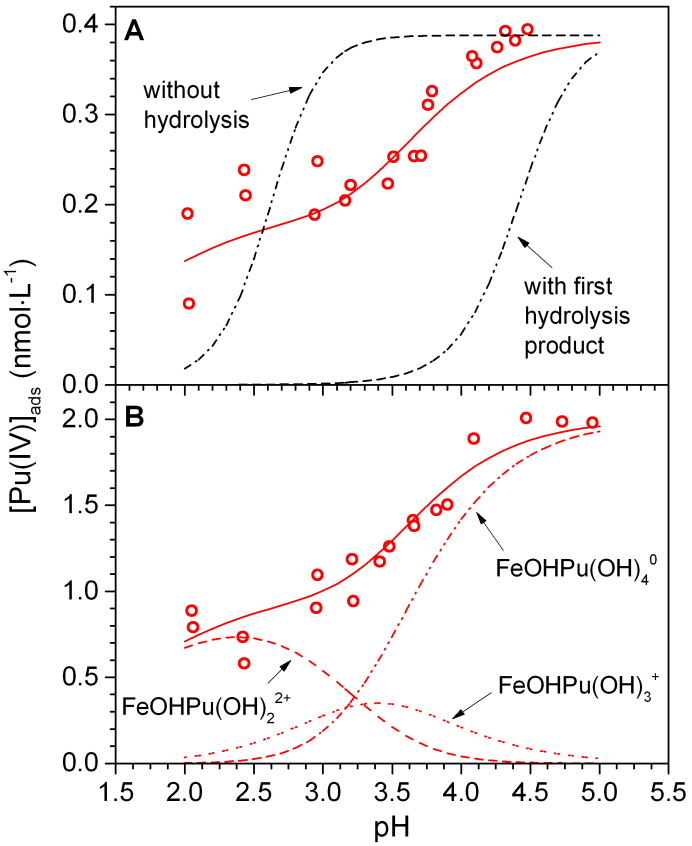

Figure 7.6: Pu sorption onto hematite as a function of pH at 25 ℃ for batch systems with $[\mathrm{Pu(IV)}]_{\mathrm{tot}}$ of $(3.88 \pm 0.01) \times 10^{-10}$ M (A) and $(2.00 \pm 0.01) \times 10^{-9}$ M (B). Data is from the second sampling event only. Pu was assumed to be present as only Pu(IV), and neither reduction nor oxidation of Pu was allowed. Solid lines are the total SCM (i.e., sum of $\equiv$FeOHPu$(OH)_2^{2+}$, $\equiv$FeOHPu$(OH)_3^+$, and $\equiv$FeOHPu$(OH)_4^0$), which gave a WSOS/DF value of 4.99. The red dashed lines (B) represent the distribution of surface complexes across the experimental pH range. A similar distribution was observed for the batch systems with lower initial Pu(IV) concentrations. The black dashed lines (A) represent the Pu(IV) sorption that is predicted when the best fit Th(IV) surface complexation reaction (i.e., $\equiv$FeOHTh^{4+}, $\log K = 19.03$) is used to model the Pu sorption data in the absence and presence of Pu(IV) hydrolysis.

7.3.2.3 Ability to Predict Pu(IV) Sorption at 25 ℃ from Th(IV) Data

As mentioned previously, it is possible that in the presence of hematite, Pu(IV) is the dominant surface species. Therefore, we also attempted to predict the Pu sorption behavior using only the best-fit SCM for Th(IV) (Sec. 7.3.1.2). When Pu(IV) hydrolysis products were excluded from the

Table 7.4: Aqueous reactions, best-fit surface complexation reactions, and associated equilibrium constants used in the 25 ℃ Pu(IV) SCM.

i	reaction	$\log K$	$\log K^{\ddagger\,a}$
13	${}^{*}\beta_{1,1}$ (Pu(IV))		
	$Pu^{4+} + H_2O \rightleftharpoons PuOH^{3+} + H^+$	0.6^b	
14	${}^{*}\beta_{2,1}$ (Pu(IV))		
	$Pu^{4+} + 2\,H_2O \rightleftharpoons Pu(OH)_2^{2+} + 2\,H^+$	0.6^b	
15	${}^{*}\beta_{3,1}$ (Pu(IV))		
	$Pu^{4+} + 3\,H_2O \rightleftharpoons Pu(OH)_3^{+} + 3\,H^+$	-2.3^b	
16	${}^{*}\beta_{4,1}$ (Pu(IV))		
	$Pu^{4+} + 4\,H_2O \rightleftharpoons Pu(OH)_4^{0} + 4\,H^+$	-8.5^b	
17	K_{SC5}		
	$\equiv FeOH + Pu^{4+} + 2\,H_2O \rightleftharpoons \equiv FeOHPu(OH)_2^{2+} + 2\,H^+$	4.95 ± 0.03^c	5.07
18	K_{SC6}		
	$\equiv FeOH + Pu^{4+} + 3\,H_2O \rightleftharpoons \equiv FeOHPu(OH)_3^{+} + 3\,H^+$	1.61 ± 0.14^c	1.73
19	K_{SC7}		
	$\equiv FeOH + Pu^{4+} + 4\,H_2O \rightleftharpoons \equiv FeOHPu(OH)_4^{0} + 4\,H^+$	-1.60 ± 0.07^c	-1.48

[a] Referenced to the site-occupancy standard state,[69] and calculated with the equation: $\log K^{\ddagger} = \log K + \log \frac{N_s A_s}{N_s^{\ddagger} A^{\ddagger}}$, where $N^{\ddagger}$ and $A^{\ddagger}$ are the theoretical site density (10×10^{18} sites m^{-2}) and surface area (10 m^2 g^{-1}) suggested by Sverjensky.[69]

[b] From Guillaumont et al.[21] for $I = 0$ M.

[c] Calculated in this work using a single-site DLM and referenced to the 1.0 M standard state; $I = 0.01$ M NaCl.

simulation (i.e., only Pu^{4+} was allowed), Pu sorption is over-predicted (Fig. 7.4). When both the free Pu^{4+} cation and the first Pu(IV) hydrolysis product, $PuOH^{3+}$, are allowed, Pu sorption is under-predicted, suggesting that Pu(IV) hydrolysis is more thermodynamically favored than a $\equiv FeOHPu^{4+}$ surface complex with a $\log K$ value equal to that for $\equiv FeOHTh^{4+}$. This is not surprising when considering the large difference in Pu(IV) and Th(IV) hydrolysis formation constants (Tables 7.1, 7.4).

7.4 Discussion

7.4.1 Comparison with Previous Studies

7.4.1.1 Np(V) Surface Complexation

Kohler et al. investigated Np(V) sorption onto hematite over a wide range of ionic strengths, pH, Np(V) concentrations, and CO_2 partial pressures.[132] Similar to our data, the Np(V) sorption edge was observed at pH $\sim$ 7. Using the triple layer model (TLM),[137] which allows differentiation between inner- and outer-sphere surface species, Kohler et al.[132] suggested that the inner-sphere surface complex, $\equiv$FeONpO_2, was dominant below pH 8 in the presence or absence of atmospheric CO_2. Additionally, at higher Np(V) sorption densities, they noted that a second inner-sphere surface complex, $\equiv$FeOHNpO_2^+, was needed to accurately model their sorption data. The necessary inclusion of a second surface species only at higher loadings suggests Np(V) association with a second, less favorable, binding site. Similar to this finding, the best-fit SCM determined here suggested a speciation change at elevated temperatures. Because the acid/base properties of hematite are temperature dependent, it is not clear if the speciation change calculated with our SCM is simply the result of charge compensation within the double layer, or if another phenomenon is responsible. However, we cannot exclude the possibility that Np(V) could favor alternative binding sites at elevated temperatures, although, this would presumably also result in increased Np(V) sorption with increasing temperature, which was not observed (Fig. 7.1).

Wang et al.[138] also used the DLM to describe Np(V) sorption onto ferrihydrite from sorption data previously published by Girvin et al.[139]. Although the Wang et al.[138] model with ferrihydrite is not directly comparable to our model with hematite, we note that a similar surface complex, $\equiv$FeONpO_2, best described the Girvin et al.[139] data. Additionally, even though the original ferrihydrite study was conducted at $I = 0.1$ M $NaNO_3$,[139] the $\log K$ calculated by Wang et al.[138] (-2.72) is in good agreement with our value at 25 ℃ (Table 7.3). Wang et al.[138] also modeled Np(V) sorption onto hematite, using data previously published by Nakayama and Sakamoto.[140] The modeling results from Wang et al. suggested that two surface complexes best described the Nakayama and Sakamoto data, $\equiv$FeOHNpO_2^+ and $(\equiv FeO)_2NpO_2^-$. Attempts to fit our Np(V) sorption data using these two surface complexes gave poorer fits (i.e., larger WSOS/DF values) compared with our chosen SCM (Table 7.3) or no convergence of the optimization procedure (depending on temperature). However,

a greater ratio of $[Np(V)]_{tot}/[\equiv FeOH]_{tot}$ in the Nakayama and Sakamoto study (0.35) compared to our study (0.0002) may have contributed to the different modeling results.

Our surface complexation modeling results are in fairly good agreement with the model proposed by Kohler et al.[132] and the ferrihydrite model proposed by Wang et al.[138] However, these models, including our own, suggest that Np(V) forms a monodentate complex with the hematite surface. This is contradictory to the results from several spectroscopic studies. For example, Arai et al. investigated the interaction between Np(V) and hematite using extended X-ray absorption fine structure (EXAFS) spectroscopy and suggested that both outer-sphere and bidentate inner-sphere surface complexes are present in the sorption samples at pH ∼7 to 9.[56] Using attenuated total reflectance fourier-transform infrared spectroscopy (ATR FTIR), Müller et al. suggested that Np(V) forms bidentate complexes on the surfaces of TiO_2, SiO_2, and ZnO based on the large observed shift (~ 30 cm^{-1}) in the antisymmetric vibrational mode of the neptunyl ion.[141] From ATR FTIR and EXAFS studies, Gückel et al. also suggested the presence of bidenate inner-sphere complexes on the surface of gibbsite ($Al(OH)_3$).[142] The reason for the discrepancy between our modeling results and these spectroscopic studies is unclear. However, in each of the spectroscopic studies, higher pH, higher Np(V) surface loadings, and generally higher ionic strengths were used compared with this study.

7.4.1.2 Th(IV) Surface Complexation

Cromières et al. used the DLM to describe Th(IV) sorption onto hematite colloids over the pH range 2 to 10.[143] Their results suggested that several surface complexes, which included $\equiv FeOHTh^{4+}$, $\equiv FeOTh(OH)_2^+$, $\equiv FeOTh(OH)_4^-$, were needed to model the sorption data over the full pH range. However, $\equiv FeOHTh^{4+}$ was the most important species at pH values similar to those studied here. Their calculated $\log K$ value for $\equiv FeOHTh^{4+}$ (18.7), is in good agreement with our $\log K$ value (19.03). Using the TLM, Murphy et al. also suggested that Th(IV) sorption onto hematite was best described using the inner-sphere surface complex, $\equiv FeOHTh^{4+}$.[144] However, Rojo et al. suggested that Th(IV) sorption onto ferrihydrite and magnetite (Fe_3O_4) could be described equally well using either a bidentate surface complex, $(\equiv FeO)_2Th^{2+}$, or a monodentate hydrolyzed surface species, $FeOThOH^{2+}$.[90] Jakobsson modeled Th(IV) sorption onto TiO_2 over a wide range of Th(IV) concentrations using several different EDL models.[145] Although monodentate Th(IV) surface complexes described most of the lower concentration data adequately, Jakobsson suggested that the proton

stoichiometry associated with Th(IV) sorption onto TiO_2 was sensitive to the surface site density. For example, when higher site densities were specified in FITEQL, a surface reaction with zero net proton release gave the best fit to the data.[145] As the site density was decreased (equivalent to increasing Th(IV) surface loading), surface reactions with an increasing number of released protons were predicted. This finding is somewhat reverse to that of Kohler et al., where fewer protons were released at higher Np(V) sorption densities.[132] However, it is clear from both of these studies that the sorbate concentration may significantly affect the reaction stoichiometry predicted with SCMs.

In contrast to our modeling results, EXAFS studies of Th(IV) sorption onto SiO_2,[146] magnetite,[147] and ferrihydrite,[147] indicate that Th(IV) may form bidentate inner-sphere complexes on these surfaces. Similar to the case for Np(V), there are significant discrepancies between the Th(IV) surface complexes indicated by SCMs and spectroscopic studies, making it difficult to determine if the Th(IV) (or Np(V)) surface complexes we propose here are representative of the surface coordination.

7.4.2 Plutonium Sorption onto Hematite

Although it is not clear if sorption equilibrium was achieved in the Pu(IV) experiment, we were able to accurately fit the second sampling event sorption edge data at 25 ℃ using a combination of three hydrolyzed Pu(IV) surface complexes (Sec. 7.3.2.2). A similar approach was taken by Sanchez et al., who demonstrated increasingly better fits to their sorption data as hydrolyzed Pu(IV) surface complexes were incrementally added to the SCM.[34] Recently, Herr[148] re-modeled the Pu(IV) sorption data from Sanchez et al., and suggested that the data was best described with the surface complexes $\equiv FeOPuOH^{2+}$ and $\equiv FeOPu(OH)_3$. Not surprisingly, the results presented by Herr[148] agree well with the expected aqueous Pu(IV) speciation over the studied pH range (Table 7.4).

As shown in Sec. 7.3.2.1, when Pu(IV) was reacted with hematite over the pH range $\sim$ 1.5 to 5.5, some oxidation occurred. We proposed that these oxidation state changes were the cause of the significant data scatter and shallow sorption edges observed for Pu sorption at each temperature. However, similar behavior has not been observed when Pu(IV) was reacted with goethite[34] or hematite.[52] As mentioned previously, this Pu oxidation appears to be the result of the thermodynamic favorability of Pu(V) in the aqueous phase. In many cases, researchers have added Pu(IV) to water free of complexing agents and found that the aqueous phase is dominated by Pu(V) at equilibrium.[149,150] Thus, in these studies, the longer equilibration periods used relative to previous

work may allow for greater concentrations of aqueous Pu(V) to form. Previous studies examining Pu(V) reduction to Pu(IV) on hematite and goethite found that Pu remaining in the aqueous phase was always dominated by Pu(V). However, oxidation of Pu(IV) to Pu(V) is considered kinetically hindered because of the necessary formation of the trans-dioxo moiety of the plutonyl structure.[127] Considering that Pu(IV) sorption should be comparatively fast,[34,52] it is surprising that Pu oxidation appears to have had such a large effect on the sorption of Pu(IV). We therefore propose that the low pH in our systems facilitates a relatively weak Pu-surface interaction allowing for greater mobility of the Pu(IV) ion on the surface, and thus greater potential for re-oxidation to and subsequent desorption of Pu(V). Therefore, this observation of Pu(IV) oxidation to Pu(V) may be due to the additional time allowed for the equilibration of our samples. To support this, the fraction Pu sorbed in samples at the lowest pH values generally decreased between the first and the second sampling events (Fig. 7.4). Therefore, Pu may have sorbed to the hematite surface initially as Pu(IV), but then desorbed after $\sim$ 1.5 weeks as Pu(V). Clearly, this behavior warrants further research. However, such an investigation is currently outside the scope of this work.

7.4.2.1 Using Th(IV) to Describe Pu(IV) Sorption onto Hematite

Because Pu is extremely redox sensitive, and because of the hazards imposed by and the regulatory limits of working with Pu, it is very appealing to use stable oxidation state analogs to study plutonium chemistry. However, comparisons between analog sorption behavior and Pu sorption behavior are few. Banik et al. observed relatively little difference between Pu(IV) and Th(IV) uptake on kaolinite in relation to the percent sorption of each actinide.[151] However, the Pu(IV) concentration in their experiment was 10^4 times greater than the Th(IV) concentration, suggesting that the Th(IV) behavior actually is not comparable with the Pu(IV). Similarly, we observed poor agreement with the Pu sorption predicted when a Th(IV) SCM was employed. These results are not surprising, considering that several researchers have already suggested that Th(IV) is not an adequate analog for Pu(IV)[152,153] due to the larger ionic radius of Th(IV) compared with Pu(IV) (1.048 vs. 0.962 Å),[154] which makes Th(IV) significantly "softer" than Pu(IV).

7.4.3 Thermodynamic Interpretation

As mentioned previously, our primary objective in this paper is to relate the thermodynamics of Np(V), Th(IV), and Pu(IV) sorption onto hematite with sorption mechanisms and changes in ac-

tinide hydration. We have previously demonstrated a correlation between the enthalpy and entropy of Eu(III)[102] and U(VI) sorption onto hematite and the extent of Eu(III) or U(VI) dehydration upon sorption. We would like to do the same here. However, the spectroscopic data for adsorbed Np(V) and Th(IV) are not consistent with our SCMs or the SCMs developed from other similar batch sorption experiments. These inconsistencies may be due to differences in experimental conditions between studies. For example, we previously noted that nearly all Np(V) spectroscopic studies were performed at ionic strengths greater than the ionic strength used for our experiments. Lützenkirchen suggested that high ionic strengths may effectively shield highly charged surface species, perhaps leading to greater surface stability or different sorption mechanisms.[155] Therefore, we will use a different approach toward understanding the thermodynamics and mechanisms of Np(V), Th(IV), and Pu(IV) sorption onto hematite.

If we consider that the formation of inner-sphere surface complexes will perturb the hydration sphere of the actinide in question, we can perhaps infer some binding mechanisms from the calculated thermodynamic parameters listed in Table 7.5. Because actinide dehydration is both an entropically favorable and endothermic reaction, we would expect inner-sphere surface complexation to result in positive entropy and enthalpy changes, as we previously observed for Eu(III)[102] and U(VI). Only considering the 25 ℃ surface complexation reaction for Np(V) sorption onto hematite, we in fact calculate a negative entropy change (Table 7.5). Combined with the apparent sorption enthalpy of ~ 0 kJ mol^{-1}, the thermodynamics suggest that there may be a greater contribution from outer-sphere Np(V) surface species than inner-sphere Np(V) surface species in our batch sorption experiments. This is despite our ability to model the Np(V) sorption data with the DLM, which assumes all surface species are inner-sphere complexes, and despite the spectroscopic literature which indicate mostly inner-sphere Np(V) surface complexation (albeit under very different experimental conditions). Furthermore, the presence of a significant contribution of outer-sphere species may also explain the significant amount of scatter observed in the Np(V) sorption data (Fig. 7.1). For Th(IV) sorption onto hematite, the story is similar, however, the rather large entropy value (Table 7.5) suggests that some Th(IV) dehydration occurs upon sorption. However, because the calculation of sorption entropies are quite dependent on the SCM employed,[102] and because the hydration entropies of the different actinides vary significantly, one cannot assume from the entropy value that only inner-sphere complexation occurs for Th(IV). If only inner-sphere complexation were present, a larger positive enthalpy should also be determined. Therefore, we propose that Th(IV) sorption

Table 7.5: Calculated thermodynamic parameters for Np(V), Th(IV), and Pu(IV) sorption onto hematite.[a]

i	reaction	$\Delta_r G_i$[b] (kJ mol^{-1})	$\Delta_r H_i$ (kJ mol^{-1})	$\Delta_r S_i$[c] (J mol^{-1} K^{-1})
9	K_{SC1}			
	$\equiv\text{FeOH} + \text{NpO}_2^+ \rightleftharpoons \equiv\text{FeONpO}_2 + \text{H}^+$	16.8	≈ 0	–56.4
11	K_{SC3}			
	$\equiv\text{FeOH} + \text{Th}^{4+} \rightleftharpoons \equiv\text{FeOHTh}^{4+}$	–108	≈ 0	364
17	K_{SC5}			
	$\equiv\text{FeOH} + \text{Pu}^{4+} + 2\,\text{H}_2\text{O}$	–28.2	—	—
	$\rightleftharpoons \equiv\text{FeOHPu(OH)}_2^{2+} + 2\,\text{H}^+$			
18	K_{SC6}			
	$\equiv\text{FeOH} + \text{Pu}^{4+} + 3\,\text{H}_2\text{O}$	–9.2	—	—
	$\rightleftharpoons \equiv\text{FeOHPu(OH)}_3^{+} + 3\,\text{H}^+$			
19	K_{SC7}			
	$\equiv\text{FeOH} + \text{Pu}^{4+} + 4\,\text{H}_2\text{O}$	9.1	—	—
	$\rightleftharpoons \equiv\text{FeOHPu(OH)}_4^{0} + 4\,\text{H}^+$			

[a] All values are for 25 °C and $I = 0.01$ M NaCl.
[b] Calculated from: $\Delta_r G_i = -RT \cdot \ln K$, where T is 298.15 K.
[c] Calculated from: $\Delta_r G_i = \Delta_r H_i - T\Delta_r S_i$, where T is 298.15 K.

onto hematite should also be described with a combination of outer-sphere and inner-sphere surface complexes. Considering the strong sorption of Th(IV) at low pH values where there is a large net positive surface charge, formation of outer sphere surface complexes is a reasonable conceptual model.

Because we could not develop SCMs for Pu(IV) sorption onto hematite at all temperatures, we were unable to extrapolate any thermodynamic parameters using the van't Hoff analysis. However, plots of K_d values as a function of inverse temperature (see Fig. D.3) indicate that sorption increased with increasing temperature (i.e., the reaction is endothermic), as previously indicated based on Fig. D.2 which illustrates Pu(IV) sorption as a function of "pH – 1/2pK_w." These findings suggest that Pu(IV) sorption onto hematite occurs predominantly via an inner-sphere mechanism, although outer-sphere complexation cannot be excluded. The observed differences between Th(IV) and Pu(IV) data are likely due to the stronger affinity of Pu(IV) for both hydrolysis and sorption to

metal oxide minerals. Thus the stonger interactions are likely a greater indication of the formation of inner-sphere surface complexes.

7.5 Conclusions

Additional research is clearly needed to understand Np(V), Th(IV), and Pu(IV) sorption onto hematite over a wider range of experimental conditions, particularly with respect to surface speciation at both low and high actinide concentrations. However, under the conditions studied, the data and analyses given above support the following conclusions:

1. Np(V) and Th(IV) sorption onto hematite are temperature independent;
2. Np(V) and Th(IV) sorption onto hematite may occur via both outer- and inner-sphere complexation mechanisms, with outer-sphere complex formation dominating Np(V) sorption;
3. assuming sorption equilibrium was achieved, Pu sorption onto hematite increases with increasing temperature, indicating the formation of inner-sphere surface complexes;
4. Pu(IV) sorption onto hematite cannot be predicted using Th(IV) sorption data.

Chapter 8

Conclusions

To better understand and to possibly predict actinide transport in the environment, it is first necessary to understand actinide chemistry over a wide range of environmentally relevant conditions. Although a significant amount of research has been devoted to understanding actinide sorption reactions onto a variety of pure minerals, soils, and sediments, very little research has been devoted to investigating the effect of temperature – a constantly fluctuating variable in environmental systems, and a very important variable when assessing the future performance of geologic nuclear waste repositories – on these reactions. Additionally, few studies which quantify important thermodynamic parameters, such as enthalpy and entropy, for actinide sorption reactions are available in the literature, despite the possibility for gaining mechanistic insight from these parameters. Therefore, the goal of this research was to develop of a better understanding of the thermodynamics and mechanisms of actinide sorption reactions. Using multiple-temperature batch sorption experiments, surface complexation modeling, and, in some cases, isothermal titration calorimetry, the effect of temperature on Eu(III) (a trivalent actinide analog), Th(IV), Np(V), U(VI), and Pu(IV) sorption onto hematite was studied, and the enthalpies and entropies for each sorption reaction were defined. Overall, this research has demonstrated the following:

- Eu(III) sorption onto hematite is endothermic and entropically favorable. A large sorption enthalpy ($\Delta_r H = +131$ kJ mol^{-1}) and entropy ($\Delta_r S \simeq 439$J K^{-1} mol^{-1}), calculated using both a van't Hoff analysis and calorimetry, and EXAFS data which demonstrate a decrease in the Eu−O coordination number upon sorption onto hematite, suggest that Eu(III) sorption

is an inner-sphere reaction driven by the displacement of H_2O molecules from it's primary hydration sphere.

- U(VI) sorption onto hematite is also endothermic and entropically favorable. However, smaller reaction enthalpies ($\Delta_r H = +35 - +102$ kJ mol^{-1}) and entropies ($\Delta_r S <\sim 370$ J K^{-1} mol^{-1}), and EXAFS data from the literature suggest that the U(VI) sorption reaction is weaker and proceeds with less U(VI) dehydration compared with the Eu(III) sorption reaction. Additionally, discrepancies between $\Delta_r H$ values calculated via the van't Hoff analysis and calorimetry indicate that additional research is needed to understand U(VI) sorption mechanisms across a wider range of concentrations.

- The sorption of Np(V) and Th(IV) onto hematite is not temperature dependent (i.e., $\Delta_r H \simeq 0$ kJ mol^{-1}), suggesting that a combination of inner- and outer-sphere surface complexes may be responsible for sorption of these actinides. However, the possibility of outer-sphere surface complexes is generally in disagreement with EXAFS literature which suggest the predominance of inner-sphere surface complexes, albeit under significantly difference experimental conditions.

- Pu(IV) sorption onto hematite appears to increase with increasing temperature, but due to Pu oxidation state changes under the acidic conditions of the experiments performed in this research, it is not clear if sorption equilibrium was achieved. However, surface complexation modeling suggests (assuming sorption equilibrium) that hydrolyzed Pu(IV) surface species, not surprisingly, play a dominant role in surface complexation.

Although the results presented here provide valuable insight into the mechanisms driving actinide sorption reactions, the experimental conditions employed here were limited, and therefore it is difficult to comment on whether these results can be related to actinide sorption reactions in the presence of other minerals, soils, or sediments. Future research efforts should focus on examining the influence of temperature on actinide sorption reactions for a wider range of experimental conditions, including ionic strength, solid phase type and concentration, and actinide concentration. Significant discrepancies were identified when comparing Np(V) and Th(IV) surface complexation modeling results with spectroscopic data available in the literature. Therefore, effort should be particularly focused on better understanding the role actinide concentration has on actinide surface speciation. Additionally, as similar thermodynamic data become available in the literature, it will

be interesting and useful to investigate possible correlations between measured sorption enthalpies and the hydration enthalpies of actinides (or other cationic metals).

Appendices

Appendix A Supplementary Data for Chapter Four

Derivation of Eq. 4.1:

Let the protonation of the hematite surface be defined with the reactions,

$$\equiv \mathrm{FeOH} + \mathrm{H}^+ \rightleftharpoons \equiv \mathrm{FeOH}_2^+ \tag{A.1}$$

$$\equiv \mathrm{FeO}^- + \mathrm{H}^+ \rightleftharpoons \equiv \mathrm{FeOH} \tag{A.2}$$

each with an equilibrium constant given by $\log K_+$ and $-\log K_-$. The enthalpy of reactions A.1 and A.2 can be related to temperature with the equations,

$$\log K_+ = -\frac{\Delta H}{\ln 10 \cdot RT} \tag{A.3}$$

$$-\log K_- = -\frac{\Delta H}{\ln 10 \cdot RT} \tag{A.4}$$

The summation of reactions A.1 and A.2 give,

$$\equiv \mathrm{FeO}^- + 2\mathrm{H}^+ \rightleftharpoons \equiv \mathrm{FeOH}_2^+ \tag{A.5}$$

where the equilibrium constant is given by $\log K_+ - \log K_-$. If the enthalpies of reactions A.1 and A.2 are equivalent, then the following equation is valid:

$$\log K_+ - \log K_- = -2\frac{\Delta H}{\ln 10 \cdot RT} \tag{A.6}$$

which can also be written as,

$$\frac{\log K_+ - \log K_-}{2} = -\frac{\Delta H}{\ln 10 \cdot RT} \tag{A.7}$$

then it follows that,

$$pzc = -\frac{\Delta H}{\ln 10 \cdot RT} \tag{A.8}$$

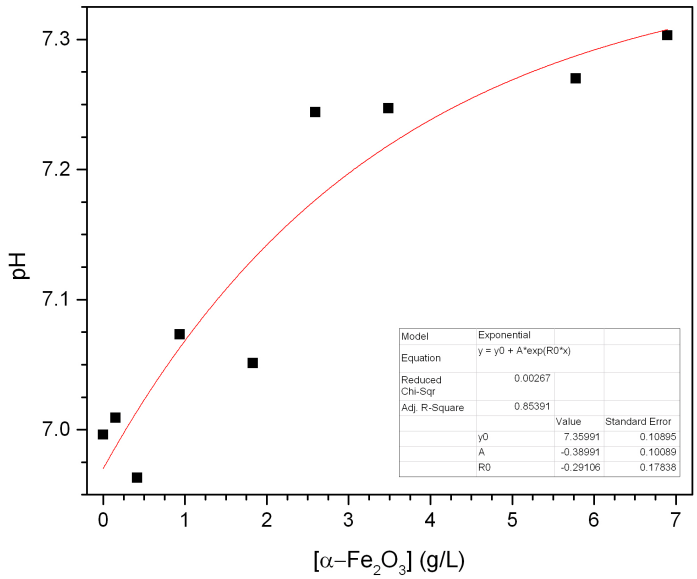

Figure A.1: Mass titration of $\alpha-Fe_2O_3$ suspensions in 0.01 M NaCl.

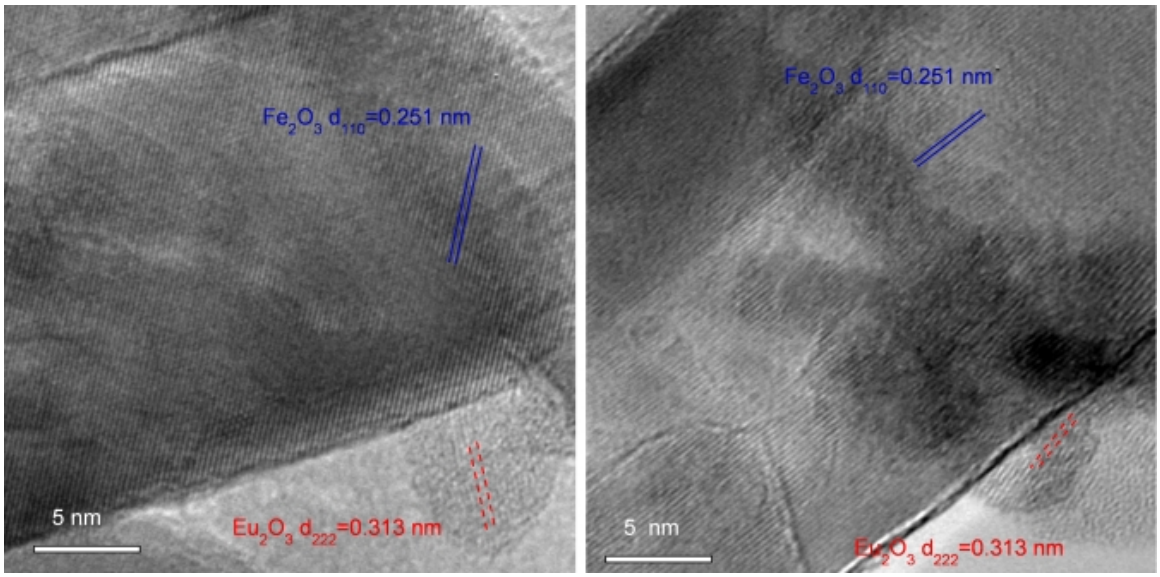

Figure A.2: HRTEM images of Eu-hematite sample showing the presence of Eu_2O_3 nano-precipitates. This was the only observation of precipitates present in our EXAFS samples.

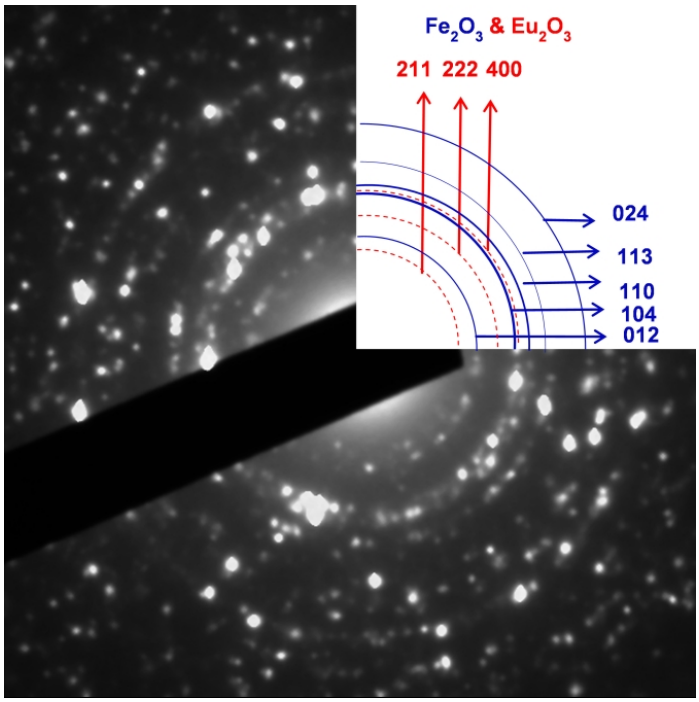

Figure A.3: Selected-area electron diffraction pattern with indices of the same Eu-hematite sample as in Fig. A.2 showing the lattice spacing for $\alpha-Fe_2O_3$ and Eu_2O_3.

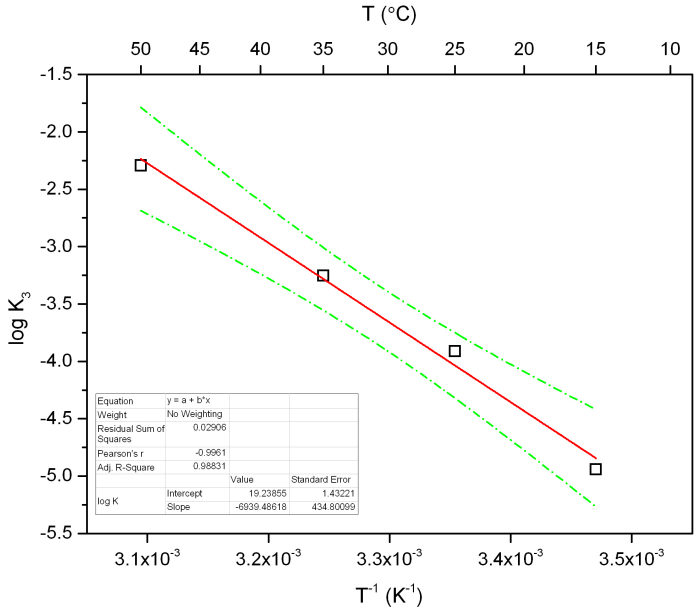

Figure A.4: van't Hoff plot using $\log K_3$ values for the surface species $(\equiv FeO)_2Eu^+$. The solid line is the linear fit with an adjusted R^2 equal to 0.989, and the dashed lines are the 95% confidence intervals.

Appendix B Supplementary Data for Chapter Five

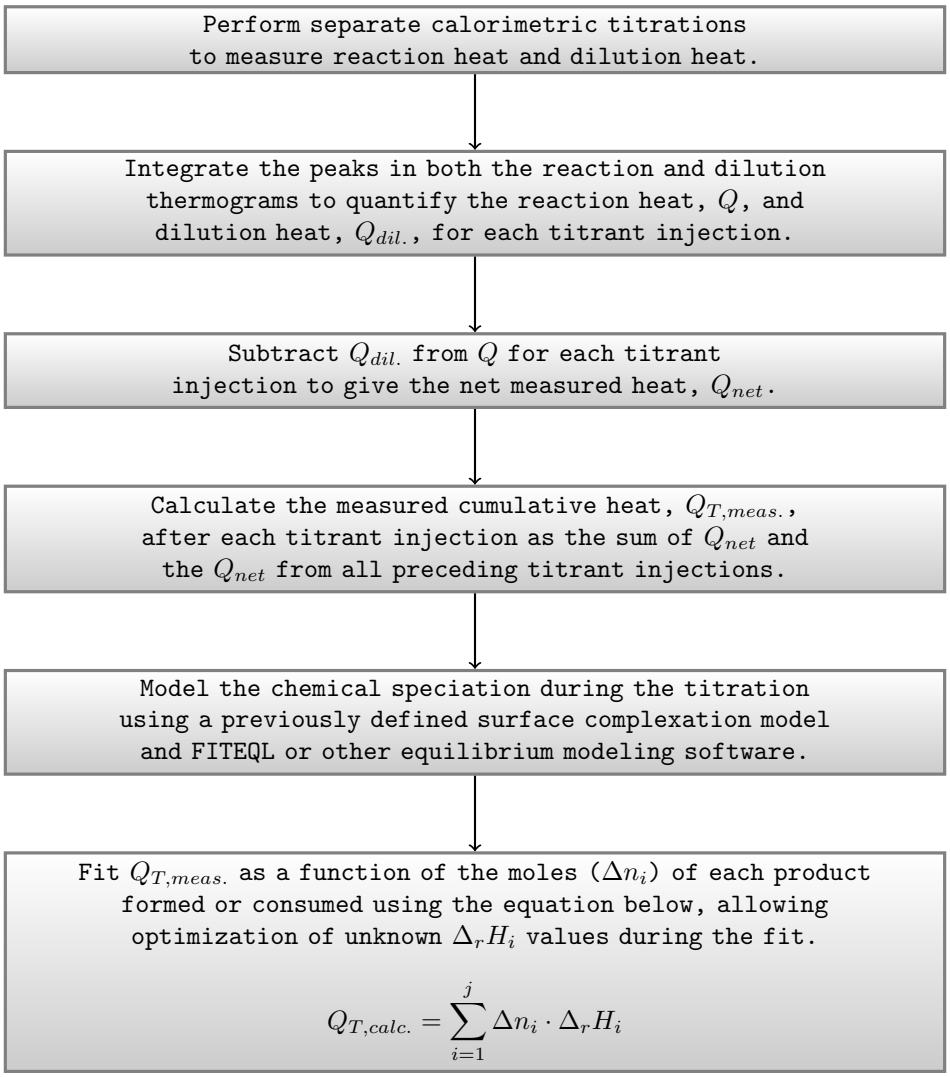

Figure B.1: Block diagram illustrating the steps needed to calculate sorption enthalpies from ITC data.

.

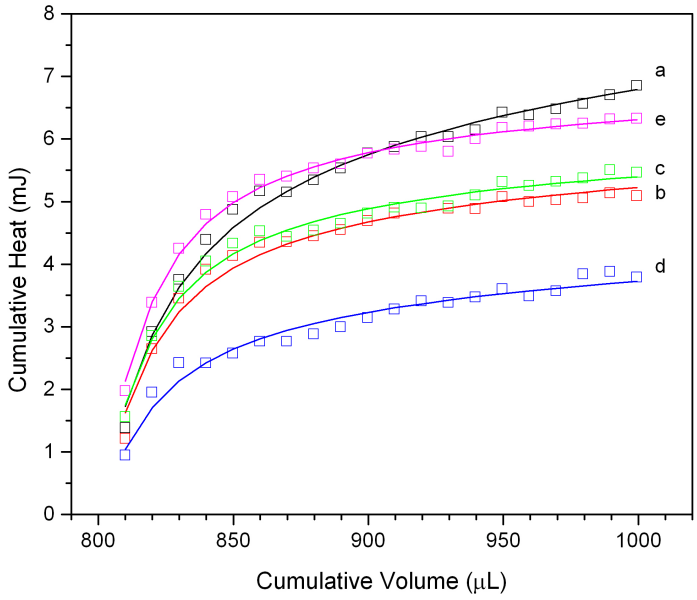

Figure B.2: Cumulative enthalpy plot for the hematite acid titrations. Titration parameters: [α–Fe_2O_3] = 7.77 g L^{-1} (c – e) or 7.91 g L^{-1} (a – b), I = 0.01 M NaCl, T = 25 ℃, titrant = 0.01 M HCl, injection volume = 9.98 μL. Open symbols are the measured cumulative heat for each titration a – e, and the solid line is the calculated heat for each titration (adjusted R^2 values are given in Table B.1).

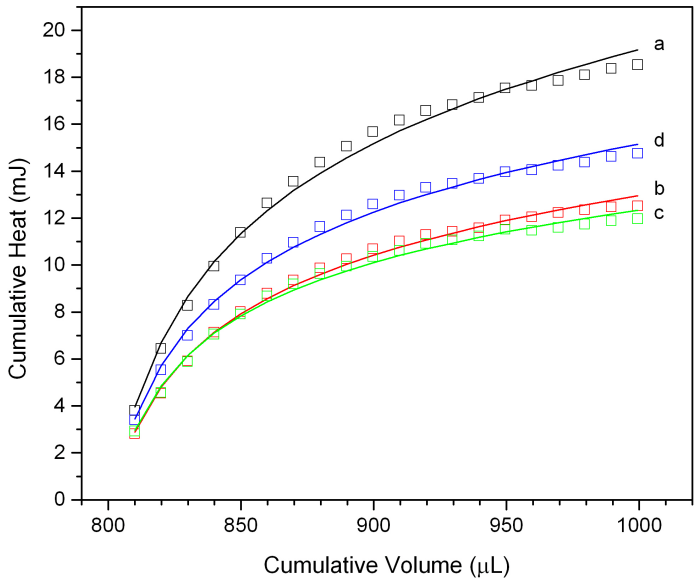

Figure B.3: Cumulative enthalpy plot for the hematite base titrations. Titration parameters: [α–Fe_2O_3] = 7.91 g L^{-1}, I = 0.01 M NaCl, T = 25 ℃, titrant = 0.01 M HCl, injection volume = 9.98 μL. Open symbols are the measured cumulative heat for each titration a – d, and the solid line is the calculated heat for each titration (adjusted R^2 values are given in Table B.1).

Table B.1: Measured pH values and calculated enthalpy values from each acid or base titration, and the adjusted R^2 for each fit.

	$\Delta_r H_3$ (kJ mol^{-1})		$\Delta_r H_2$ (kJ mol^{-1})				
	value	1σ	value	1σ	adj. R^2	initial pH	final pH
acid a	38.7	1.6	-4.8	0.4	0.990	6.81	2.75
acid b	41.8	1.6	-0.9	0.4	0.980	6.81	2.78
acid c	42.8	1.5	-1.0	0.4	0.982	6.58	2.84
acid d	22.7	1.6	-2.2	0.4	0.963	6.43	2.84
acid e	52.9	1.0	-0.5	0.3	0.994	6.33	2.75
base a	28.5	1.7	16.2	5.4	0.991	6.81	10.68
base b	39.7	1.1	1.1	3.4	0.992	6.81	10.95
base c	42.8	1.1	7.0	3.6	0.989	6.64	10.72
base d	37.4	1.2	12.7	3.9	0.992	6.64	10.96
average	38.6	8.7	3.1	7.2			

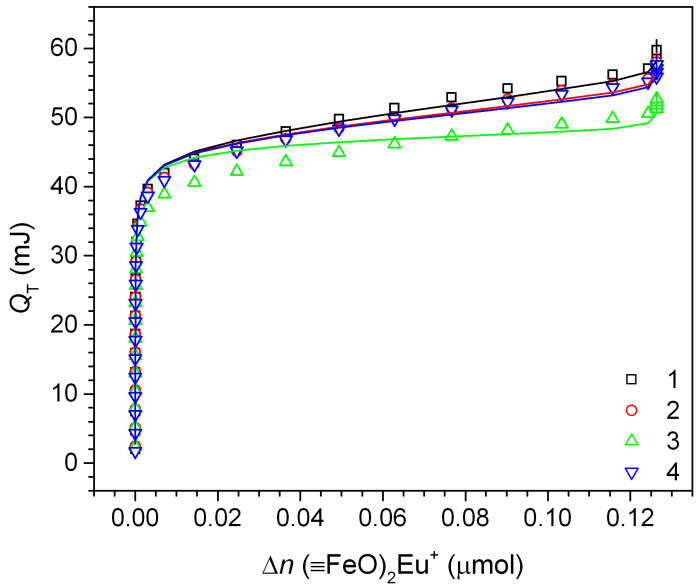

Figure B.4: Cumulative enthalpy plot as a function of $(\equiv FeO)_2Eu^+$ formation. Titration parameters: $[Eu(III)]_0 = 1.56 \times 10^{-4}$ M, $[\alpha\text{–}Fe_2O_3] = 6.71$ g L^{-1}, $I = 0.01$ M NaCl, $T = 25$ °C, titrant = 0.01 M NaOH, injection volume = 4.97 μL. Open symbols are the measured cumulative heat for each titration 1 – 4, and solid lines are the corresponding calculated cumulative heat for each titration (adjusted R^2 values are given in Table B.2).

Table B.2: Measured pH values and calculated enthalpy values from each Eu(III) base titration, and the adjusted R^2 for each fit.

	$\Delta_r H_4$ (kJ mol^{-1})				
	value	1σ	adjusted R^2	initial pH	final pH
1	104.76	2.72	0.997	3.14	7.19
2	119.29	3	0.996	3.14	7.34
3	164.5	5.6	0.985	3.11	9.36
4	122.71	4.01	0.994	2.96	8.91
average	127.81	2		3.09 $\pm$0.09	8.2 $\pm$1.1

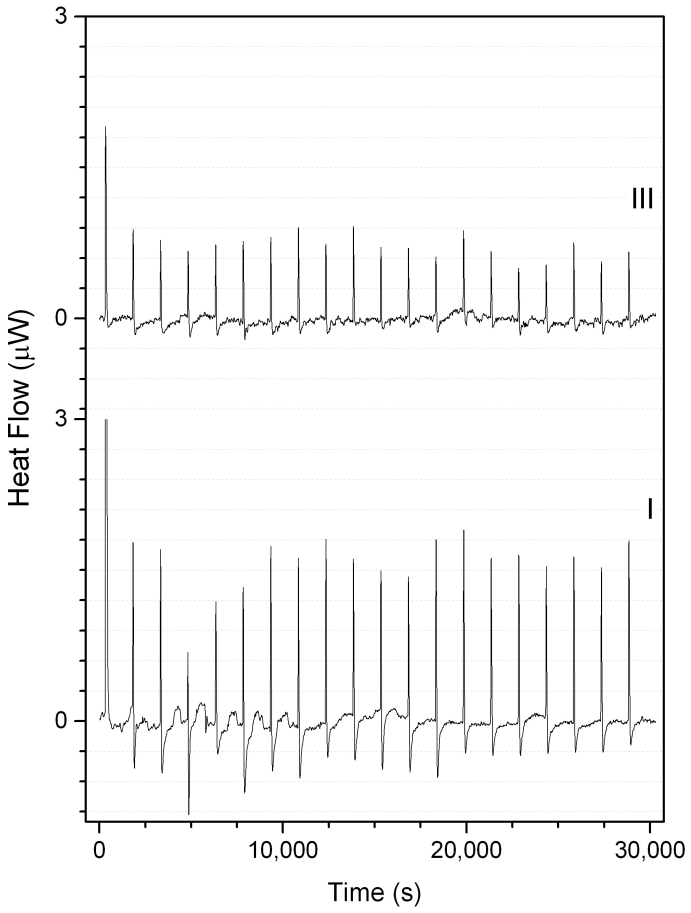

Figure B.5: Two titration thermograms for Eu(III) sorption onto hematite at pH $\sim$ 6. Titration parameters: $[\text{Eu(III)}]_0$ = 0 M, $[\alpha\text{–Fe}_2\text{O}_3]$ = 7.77 g L^{-1}, I = 0.01 M NaCl, T = 25 ℃, titrant = 0.1 mM $EuCl_3$ in 0.01 M NaCl at pH $\sim$ 6, injection volume = 9.98 μL. The Gaussian peak fitting tool in Origin was used to extrapolate the heat associated with only the endothermic peaks shown for titration I. We assumed the endothermic heat was representative of Eu(III) sorption or de-protonation of the hematite surface. This heat data was fit as shown in Fig. B.6

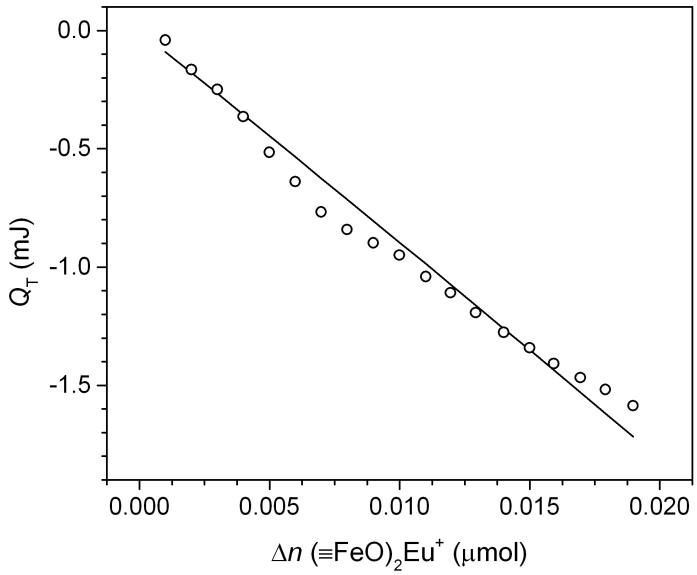

Figure B.6: Cumulative enthalpy plot as a function of $(\equiv FeO)_2Eu^+$ formation for a Eu(III) titration at pH $\sim$ 6. The heat data was fit in the same manner as the Eu(III) base titrations, except only considering the reactions on the hematite surface (i.e., OH^- formation was excluded). Titration parameters: $[Eu(III)]_0$ = 0 M, $[\alpha{-}Fe_2O_3]$ = 7.77 g L^{-1}, I = 0.01 M NaCl, T = 25 ℃, titrant = 0.1 mM $EuCl_3$ in 0.01 M NaCl at pH $\sim$ 6, injection volume = 9.98 μL. Open symbols are the cumulative heat extrapolated from endothermic peaks in titration I in Fig. B.5; and the solid line is the calculated cumulative heat (adjusted $R^2 = 0.975$); the calculated $\Delta_r H_4 = 127.5 \pm 1.5$ kJ mol^{-1}.

Appendix C Supplementary Data for Chapter Six

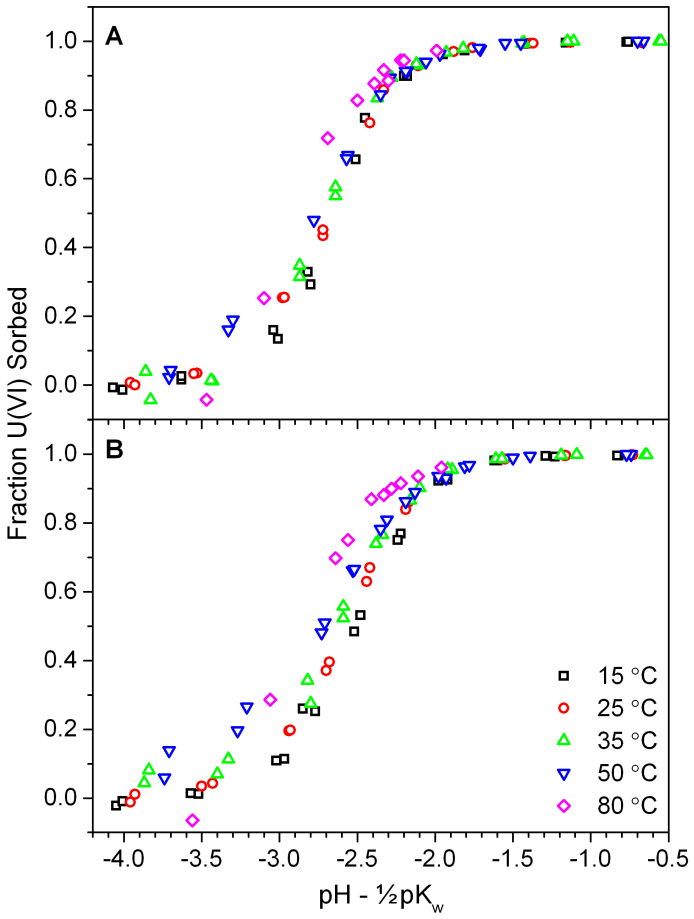

Figure C.1: U(VI) sorption onto hematite as a function of pH – $1/2\mathrm{p}K_w$ and temperature for total U(VI) concentrations $(2.16 \pm 0.06) \times 10^{-8}$ M (A) and $(4.35 \pm 0.06) \times 10^{-8}$ M (B). The sorption edge shift to lower pH indicates that U(VI) sorption increases as temperature increases.

Table C.1: Reactions considered during development of the surface complexation model describing U(VI) sorption onto hematite.

	reactions
A	$2 \equiv \mathrm{FeOH} + \mathrm{UO_2^{2+}} \rightleftharpoons (\equiv \mathrm{FeOH})_2\mathrm{UO_2} + 2\,\mathrm{H^+}$
B	$2 \equiv \mathrm{FeOH} + \mathrm{UO_2^{2+}} \rightleftharpoons (\equiv \mathrm{FeO})_2\mathrm{UO_2} + 2\,\mathrm{H^+}$ $2 \equiv \mathrm{FeOH} + \mathrm{UO_2^{2+}} \rightleftharpoons (\equiv \mathrm{FeOH})_2\mathrm{UO_2^{2+}}$
C	$2 \equiv \mathrm{FeOH} + \mathrm{UO_2^{2+}} \rightleftharpoons (\equiv \mathrm{FeO})_2\mathrm{UO_2} + 2\,\mathrm{H^+}$ $2 \equiv \mathrm{FeOH} + \mathrm{UO_2^{2+}} \rightleftharpoons (\equiv \mathrm{FeOH})_2\mathrm{UO_2^{2+}}$ $2 \equiv \mathrm{FeOH} + \mathrm{UO_2^{2+}} + \mathrm{H_2O} \rightleftharpoons (\mathrm{FeO})_2\mathrm{UO_2OH^-} + 3\,\mathrm{H^+}$
D	$2 \equiv \mathrm{FeOH} + \mathrm{UO_2^{2+}} \rightleftharpoons (\equiv \mathrm{FeO})_2\mathrm{UO_2} + 2\,\mathrm{H^+}$ $2 \equiv \mathrm{FeOH} + \mathrm{UO_2^{2+}} \rightleftharpoons (\equiv \mathrm{FeOH})_2\mathrm{UO_2^{2+}}$ $2 \equiv \mathrm{FeOH} + \mathrm{UO_2^{2+}} + \mathrm{H_2O} \rightleftharpoons (\equiv \mathrm{FeO})_2\mathrm{UO_2OH^-} + 3\,\mathrm{H^+}$ $2 \equiv \mathrm{FeOH} + \mathrm{UO_2^{2+}} + 2\,\mathrm{H_2O} \rightleftharpoons (\equiv \mathrm{FeO})_2\mathrm{UO_2(OH)_2^{2-}} + 4\,\mathrm{H^+}$
E	$2 \equiv \mathrm{FeOH} + \mathrm{UO_2^{2+}} \rightleftharpoons (\equiv \mathrm{FeO})_2\mathrm{UO_2} + 2\,\mathrm{H^+}$ $2 \equiv \mathrm{FeOH} + \mathrm{UO_2^{2+}} \rightleftharpoons (\equiv \mathrm{FeOH})_2\mathrm{UO_2^{2+}}$ $2 \equiv \mathrm{FeOH} + \mathrm{UO_2^{2+}} + 2\,\mathrm{H_2O} \rightleftharpoons (\equiv \mathrm{FeO})_2\mathrm{UO_2(OH)_2^{2-}} + 4\,\mathrm{H^+}$
F	$2 \equiv \mathrm{FeOH} + \mathrm{UO_2^{2+}} \rightleftharpoons (\equiv \mathrm{FeOH})_2\mathrm{UO_2^{2+}}$
G	$2 \equiv \mathrm{FeOH} + \mathrm{UO_2^{2+}} \rightleftharpoons (\equiv \mathrm{FeOH})_2\mathrm{UO_2^{2+}}$ $2 \equiv \mathrm{FeOH} + \mathrm{UO_2^{2+}} + \mathrm{H_2O} \rightleftharpoons (\equiv \mathrm{FeO})_2\mathrm{UO_2OH^-} + 3\,\mathrm{H^+}$
H	$2 \equiv \mathrm{FeOH} + \mathrm{UO_2^{2+}} \rightleftharpoons (\equiv \mathrm{FeO})_2\mathrm{UO_2} + 2\,\mathrm{H^+}$ $\equiv \mathrm{FeOH} + \mathrm{UO_2^{2+}} \rightleftharpoons \equiv \mathrm{FeOUO_2^+} + \mathrm{H^+}$

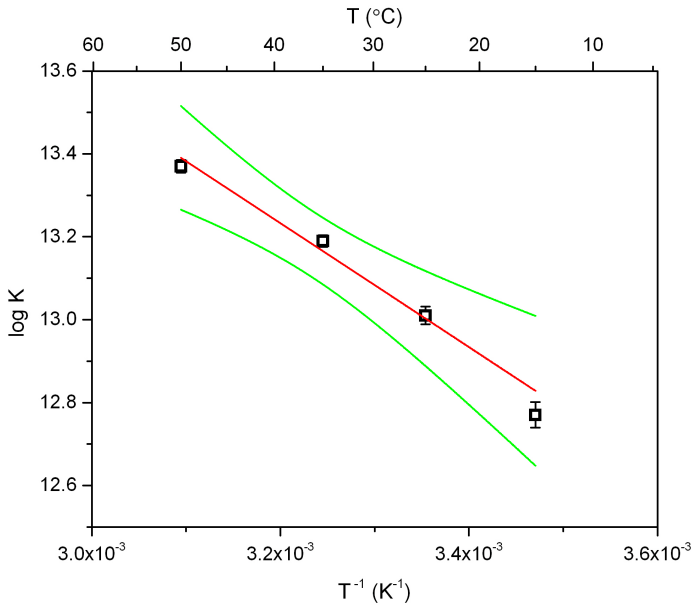

Figure C.2: van't Hoff plot using $\log K$ values for the surface species $(\equiv \mathrm{FeOH})_2\mathrm{UO}_2^{2+}$. The red line is the linear fit with an adjusted R^2 equal to 0.967, and the green lines are the 95% confidence intervals.

Appendix D Supplementary Data for Chapter Seven

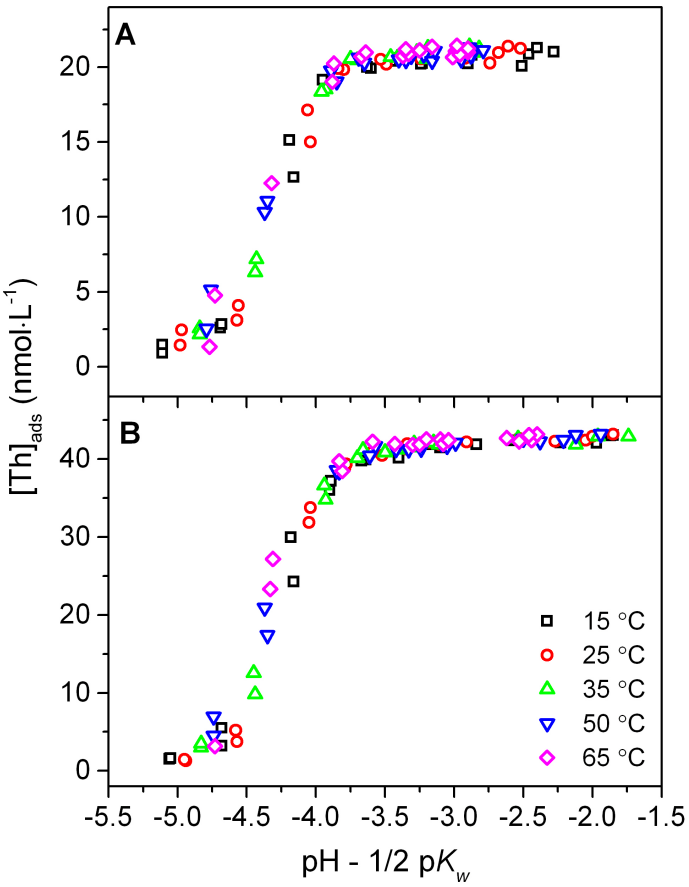

Figure D.1: Th(IV) sorption onto hematite as a function of pH – $1/2\mathrm{p}K_w$ and temperature for total Th(IV) concentrations of $(2.11 \pm 0.02) \times 10^{-8}$ M (A) and $(4.23 \pm 0.05) \times 10^{-8}$ M (B).

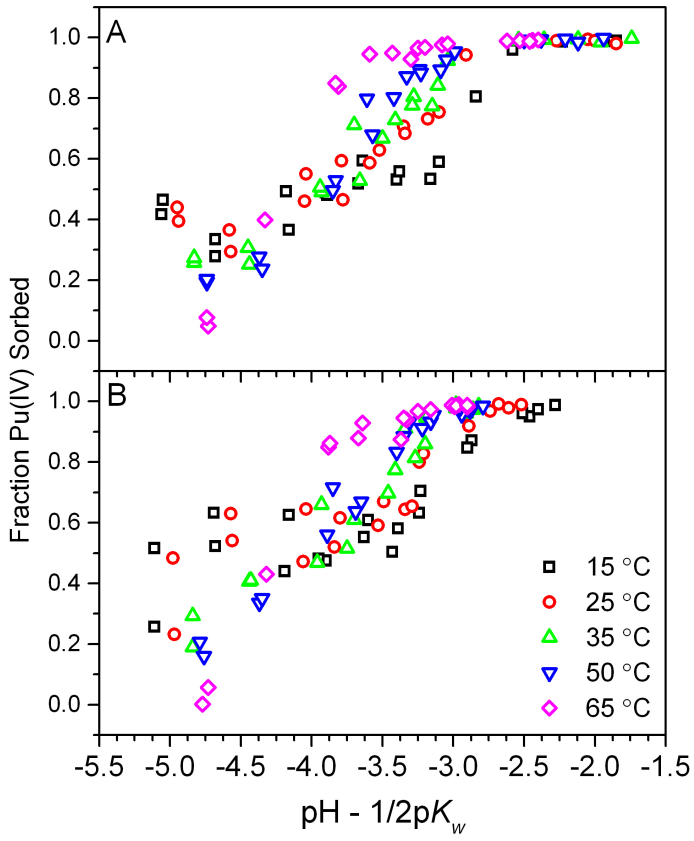

Figure D.2: Pu(IV) sorption onto hematite as a function of pH – 1/2pK_w and temperature for batch systems with total Pu(IV) concentrations of $(3.88\pm0.01)\times10^{-10}$ M (A) and $(2.00\pm0.01)\times10^{-9}$ M (B).

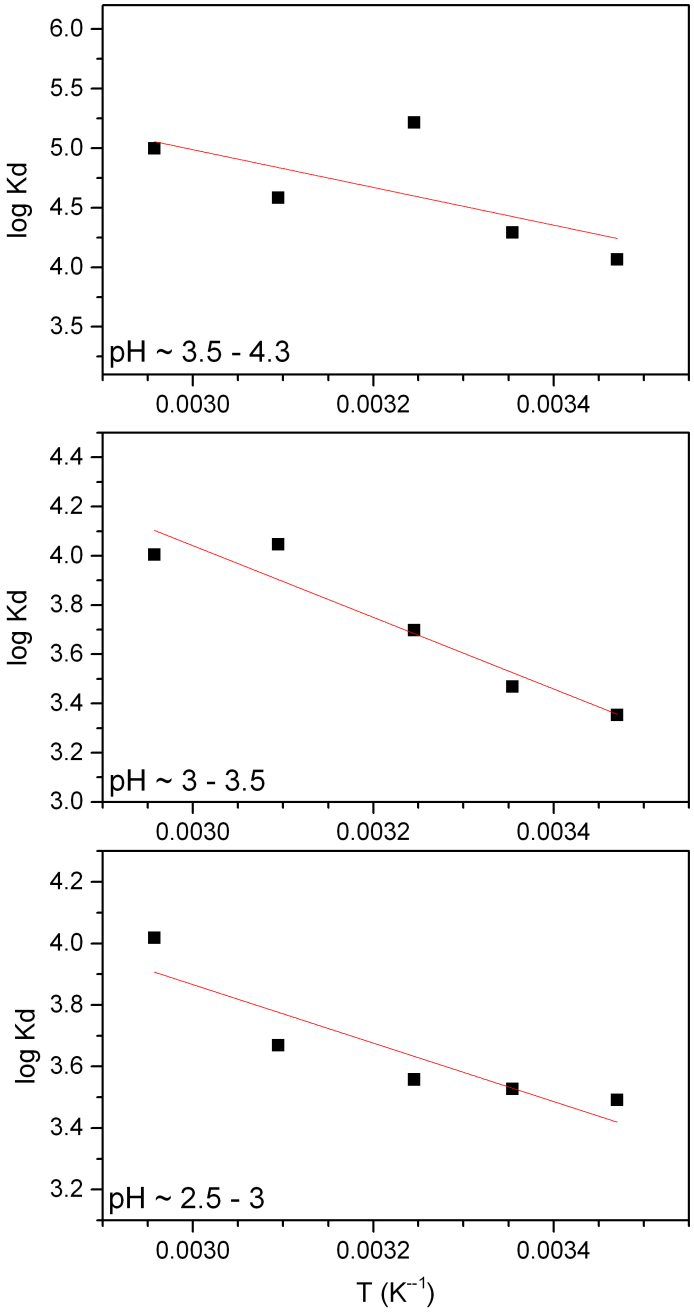

Figure D.3: log K_d as a function of inverse temperature for Pu(IV) batch systems at three pH values.

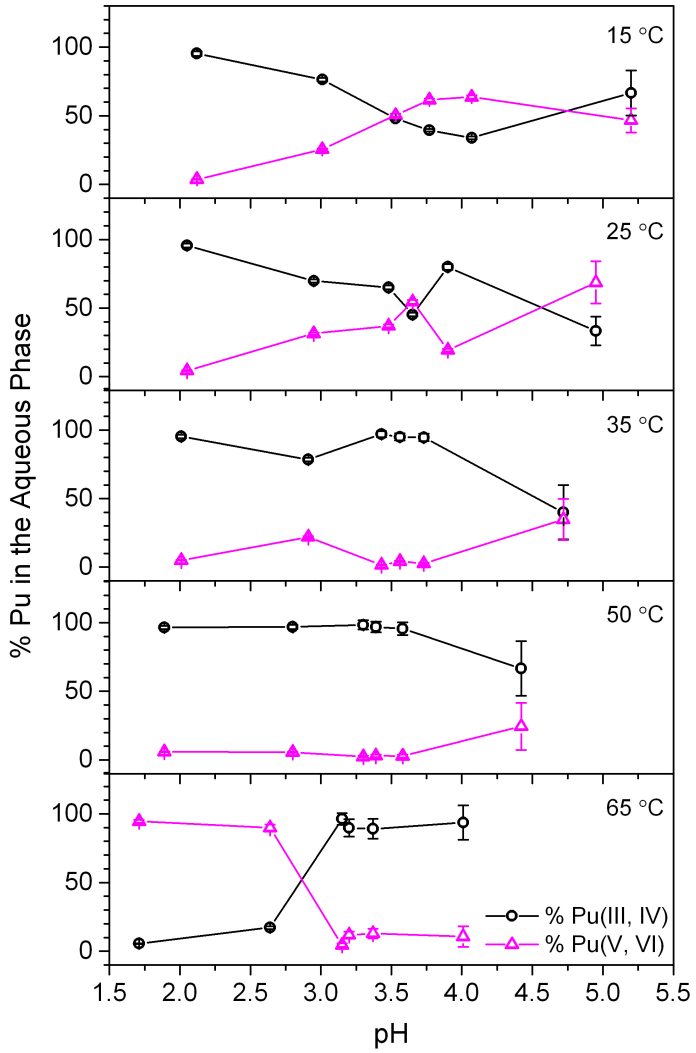

Figure D.4: Pu oxidation state distribution in the aqueous phase as a function of pH and temperature for the batch systems with initial $Pu(IV)_{tot}$ concentrations of $(2.00 \pm 0.01) \times 10^{-9}$ M Pu(IV). Errors, calculated from counting statistics, are $\pm 1\sigma$. Pu(III,IV) concentrations are from solvent extraction with PMBP in cyclohexane, and agree well with results from LaF_3 coprecipitation. Pu(V/VI) concentrations are from coprecipitation with LaF_3.

References

(1) Kersting, A. B.; Efurd, D. W.; Finnegan, D. L.; Rokop, D. J.; Smith, D. K.; Thompson, J. L. Migration of plutonium in ground water at the Nevada Test Site. *Nature* **1999**, *397*, 56–59.

(2) Novikov, A. P.; Kalmykov, S. N.; Utsunomiya, S.; Ewing, R. C.; Horreard, F.; Merkulov, A.; Clark, S. B.; Tkachev, V. V.; Myasoedov, B. F. Colloid Transport of Plutonium in the Far-Field of the Mayak Production Association, Russia. *Science* **2006**, *314*, 638–641.

(3) Almazan-Torres, M. G.; Drot, R.; Mercier-Bion, F.; Catalette, H.; Den Auwer, C.; Simoni, E. Surface complexation modeling of uranium(VI) sorbed onto zirconium oxophosphate versus temperature: Thermodynamic and structural approaches. *J. Colloid Interface Sci.* **2008**, *323*, 42–51.

(4) Riley, R. G; Zachara, J. M. Chemical contaminants on DOE lands and selection of contaminant mixtures for subsurface science research., DOE/ER-0547T, Richland, WA: Pacific Northwest Laboratory, 1992.

(5) Burghardt, D.; Simon, E.; Knller, K.; Kassahun, A. Immobilization of uranium and arsenic by injectible iron and hydrogen stimulated autotrophic sulphate reduction. *J. Contam. Hydrol.* **2007**, *94*, 305–314.

(6) Lieser, K. H. Radionuclides in the Geosphere: Sources, Mobility, Reactions in Natural Waters and Interactions with Solids. *Radiochim. Acta* **1995**, *70/71*, 355–375.

(7) Meinrath, G.; Volke, P.; Helling, C.; Dudel, E. G.; Merkel, B. J. Determination and interpretation of environmental water samples contaminated by uranium mining activities. *Fresenius' J. Anal. Chem.* **1999**, *364*, 191–202.

(8) Noubactep, C.; Meinrath, G.; Dietrich, P.; Merkel, B. Mitigating Uranium in Groundwater: Prospects and Limitations. *Environ. Sci. Technol.* **2003**, *37*, 4304–4308.

(9) Langmuir, D., *Aqueous Environmental Geochemistry*; Prentice Hall: Upper Saddle River, NJ, 1997.

(10) Hughes, L. D.; Powell, B.; Soreefan, A. M.; Falta, D. A.; DeVol, T. A. Anomalously high levels of uranium and other naturally occurring radionuclides in private wells in the piedmont region of South Carolina. *Health Phys.* **2005**, *88*, 248–252.

(11) Asikainen, M. State of disequilibrium between ^{238}U, ^{234}U, ^{226}Ra, and ^{222}Rn in groundwater from bedrock. *Geochim. Cosmochim. Acta* **1981**, *45*, 201–206.

(12) Salonen, L. In *Future Groundwater Resources at Risk*, Soveri, J., Suokko, T., Eds.; Proceedings of the Helsinki Conference 222; International Association of Hydrological Sciences: Wallingford, UK, 1994, pp 71–84.

(13) Choppin, G. R. Solution Chemistry of the Actinides. *Radiochim. Acta* **1983**, *32*, 43–53.

(14) Silva, R. J.; Nitsche, H. Actinide Environmental Chemistry. *Radiochim. Acta* **1995**, *70*, 377–396.

(15) Runde, W. The Chemical Interactions of Actinides in the Environment. *Los Alamos Science* **2000**, *26*, 392–411.

(16) *The Chemistry of the Actinide and Transactinide Elements*, 3rd ed.; Morss, L. R., Edelstein, N. M., Fuger, J., Eds.; Springer: The Netherlands, 2006; Vol. 1–5.

(17) Choppin, G. Actinide speciation in the environment. *J. Radioanal. Nucl. Chem.* **2007**, *273*, 695–703.

(18) Begg, J. D.; Zavarin, M.; Zhao, P.; Tumey, S. J.; Powell, B.; Kersting, A. B. Pu(V) and Pu(IV) sorption to montmorillonite. *Environ. Sci. Technol.* **2013**, *47*, 5146–5133.

(19) Allard, B.; Kipatsi, H.; Lilijenzin, J. *J. Inorg. Nucl. Chem.* **1980**, *42*, 1015–1027.

(20) Peretrukhin, V.; Shilov, V.; Pikaev, A.; Delegard, C. Alkaline chemistry of transuranium elements and technetium and the treatment of alkaline radioactive wastes., Report No. WHC-EP-0817, Westinghouse, Hanford Company, 1995.

(21) Guillaumont, R.; Fanghanel, T.; Neck, V.; Fuger, J.; Palmer, D. A.; Grenthe, I.; Rand, M. H., *Update on the chemical thermodynamics of uranium, neptunium, plutonium, americium and technetium*; Mompean, F. J., Illemassne, M., Domenech-Orti, C., BEN SAID, K., Eds.; Chemical Thermodynamics, Vol. 5; Elsevier: New York, NY, 2003.

(22) Klungness, G. D.; Byrne, R. H. Comparative hydrolysis behavior of the rare earths and yttrium: the influence of temperature and ionic strength. *Polyhedron* **2000**, *19*, 99–107.

(23) Rao, L.; Srinivasan, T. G.; Garnov, A. Y.; Zanonato, P.; Di Bernardo, P.; Bismondo, A. Hydrolysis of neptunium(V) at variable temperatures (10 to 85 ℃). *Geochim. Cosmochim. Acta* **2004**, *68*, 4821–4830.

(24) Zhao, P.; Zavarin, M.; Leif, R. N.; Powell, B. A.; Singleton, M. J.; Lindvall, R. E.; Kersting, A. B. Mobilization of actinides by dissolved organic compounds at the Nevada Test Site. *Appl. Geochem.* **2011**, *26*, 308–318.

(25) Wall, J.; Krumholz, L. Uranium reduction. *Annu. Rev. Microbiol.* **2006**, *60*, 149–166.

(26) Farrell, J.; Bostick, W. D.; Jarabek, R. J.; Fiedor, J. N. Uranium Removal from Ground Water Using Zero Valent Iron Media. *Ground Water* **1999**, *37*, 618–624.

(27) Fiedor, J. N.; Bostick, W. D.; Jarabek, R. J.; Farrell, J. Understanding the Mechanism of Uranium Removal from Groundwater by Zero-Valent Iron Using X-ray Photoelectron Spectroscopy. *Environ. Sci. Technol.* **1998**, *32*, 1466–1473.

(28) Gu, B; Liang, L; Dickey, M. J.; Yin, X; Dai, S Reductive precipitation of uranium(VI) by zero-valent iron. *Environ. Sci. Technol.* **1998**, *32*, 3366–3373.

(29) Powell, B. A.; Kersting, A.; Zavarin, M.; Zhao, P. Development of a Composite Non-Electrostatic Surface Complexation Model Describing Plutonium Sorption to Aluminosilicates., LLNL-TR-408276, Livermore, CA: Lawrence Livermore National Laboratory, Jan. 2011, p 77.

(30) Geckeis, H.; Lützenkirchen, J.; Polly, R.; Rabung, T.; Schmidt, M. Mineral Water Interface Reactions of Actinides. *Chem. Rev.* **2013**, *113*, 1016–1062.

(31) Brown, G. E.; Henrich, V. E.; Casey, W. H.; Clark, D. L.; Eggleston, C.; Felmy, A.; Goodman, D. W.; Grtzel, M.; Maciel, G.; McCarthy, M. I.; Nealson, K. H.; Sverjensky, D. A.; Toney, M. F.; Zachara, J. M. Metal Oxide Surfaces and Their Interactions with Aqueous Solutions and Microbial Organisms. *Chem. Rev.* **1999**, *99*, 77–174.

(32) Catalano, J. G.; Brown Jr., G. E. Uranyl adsorption onto montmorillonite: Evaluation of binding sites and carbonate complexation. *Geochim. Cosmochim. Acta* **2005**, *69*, 2995–3005.

(33) Keeney-Kennicutt, W. L.; Morse, J. W. The redox chemistry of $Pu(V)O_2^+$ interaction with common mineral surfaces in dilute solutions and seawater. *Geochim. Cosmochim. Acta* **1985**, *49*, 2577–2588.

(34) Sanchez, A. L.; Murray, J. W.; Sibley, T. H. The adsorption of plutonium IV and V on goethite. *Geochim. Cosmochim. Acta* **1985**, *49*, 2297–2307.

(35) Powell, B. A.; Fjeld, R. A.; Kaplan, D. I.; Coates, J. T.; Serkiz, S. M. $Pu(V)O_2^+$ Adsorption and Reduction by Synthetic Hematite and Goethite. *Environ. Sci. Technol.* **2005**, *39*, 2107–2114.

(36) Powell, B. A.; Fjeld, R. A.; Kaplan, D. I.; Coates, J. T.; Serkiz, S. M. $Pu(V)O_2^+$ Adsorption and Reduction by Synthetic Magnetite (Fe_3O_4). *Environ. Sci. Technol.* **2004**, *38*, 6016–6024.

(37) Shaughnessy, D. A.; Nitsche, H.; Booth, C. H.; Shuh, D. K.; Waychunas, G. A.; Wilson, R. E.; Gill, H.; Cantrell, K. J.; Serne, R. J. Molecular Interfacial Reactions between Pu(VI) and Manganese Oxide Minerals Manganite and Hausmannite. *Environ. Sci. Technol.* **2003**, *37*, 3367–3374.

(38) Powell, B. A.; Duff, M. C.; Kaplan, D. I.; Fjeld, R. A.; Newville, M.; Hunter, D. B.; Bertsch, P. M.; Coates, J. T.; Eng, P.; Rivers, M. L.; Serkiz, S. M.; Sutton, S. R.; Triay, I. R.; Vaniman, D. T. Plutonium Oxidation and Subsequent Reduction by Mn(IV) Minerals in Yucca Mountain Tuff. *Environ. Sci. Technol.* **2006**, *40*, 3508–3514.

(39) Morgenstern, A; Choppin, G. Kinetics of the oxidation of Pu(IV) by manganese dioxide. *Radiochim. Acta* **2002**, *90*, 69–74.

(40) Kaplan, D. I.; Powell, B. A.; Demirkanli, D. I.; Fjeld, R. A.; Molz, F. J.; Serkiz, S. M.; Coates, J. T. Influence of Oxidation States on Plutonium Mobility during Long-Term Transport through an Unsaturated Subsurface Environment. *Environ. Sci. Technol.* **2004**, *38*, 5053–5058.

(41) Hixon, A. E.; Arai, Y.; Powell, B. A. Examination of the effect of alpha radiolysis on plutonium(V) sorption to quartz using multiple plutonium isotopes. *J. Colloid Interface Sci.* **2013**, *403*, 105–112.

(42) Lu, N.; Reimus, P. W.; Parker, G. R.; Conca, J. L.; Triay, I. R. Sorption kinetics and impact of temperature, ionic strength and colloid concentration on the adsorption of plutonium-239 by inorganic colloids. *Radiochim. Acta* **2003**, *91*, 713–720.

(43) Yucca Mountain Science and Engineering Report Rev. 1., Report No. DOE/RW-0539-1, North Las Vegas, NV: U.S. Department of Energy, Office of Civilian Radioactive Waste Management, 2002.

(44) Luo, Y.-R.; Byrne, R. H. Carbonate complexation of yttrium and the rare earth elements in natural waters. *Geochim. Cosmochim. Acta* **2004**, *68*, 691–699.

(45) Rodda, D. P.; Johnson, B. B.; Wells, J. D. Modeling the Effect of Temperature on Adsorption of Lead(II) and Zinc(II) onto Goethite at Constant pH. *J. Colloid Interface Sci.* **1996**, *184*, 365–377.

(46) Angove, M. J.; Johnson, B. B.; Wells, J. D. The Influence of Temperature on the Adsorption of Cadmium(II) and Cobalt(II) on Kaolinite. *J. Colloid Interface Sci.* **1998**, *204*, 93–103.

(47) Tertre, E.; Berger, G.; Simoni, E.; Castet, S.; Giffaut, E.; Loubet, M.; Catalette, H. Europium retention onto clay minerals from 25 to 150 ℃: Experimental measurements, spectroscopic features and sorption modelling. *Geochim. Cosmochim. Acta* **2006**, *70*, 4563–4578.

(48) Quinn, K. A.; Byrne, R. H.; Schijf, J. Sorption of yttrium and rare earth elements by amorphous ferric hydroxide: Influence of temperature. *Environ. Sci. Technol.* **2007**, *41*, 541–546.

(49) Horn, J. R.; Russell, D.; Lewis, E. A.; Murphy, K. P. van't Hoff and calorimetric enthalpies from isothermal titration calorimetry: Are there significant discrepancies? *Biochem.* **2001**, *40*, 1774–1778.

(50) Christensen, J. J.; Ruckman, J.; Eatough, D. J.; Izatt, R. M. Determination of equilibrium constants by titration calorimetry: Part I. Introduction to titration calorimetry. *Thermochim. Acta* **1972**, *3*, 203–218.

(51) Fang, L.; Huang, Q.; Wei, X.; Liang, W.; Rong, X.; Chen, W.; Cai, P. Microcalorimetric and potentiometric titration studies on the adsorption of copper by extracellular polymeric substances (EPS), minerals and their composites. *Bioresour. Technol.* **2010**, *101*, 5774–5779.

(52) Romanchuk, A. Y.; Kalmykov, S. N.; Aliev, R. A. Plutonium sorption onto hematite colloids at femto- and nanomolar concentrations. *Radiochim. Acta* **2011**, *99*, 137–144.

(53) Zavarin, M.; Powell, B. A.; Bourbin, M.; Zhao, P.; Kersting, A. B. Np(V) and Pu(V) Ion Exchange and Surface-Mediated Reduction Mechanisms on Montmorillonite. *Environ. Sci. Technol.* **2012**, *46*, 2692–2698.

(54) Bauer, A.; Rabung, T.; Claret, F.; Schfer, T.; Buckau, G.; Fanghnel, T. Influence of temperature on sorption of europium onto smectite: The role of organic contaminants. *Appl. Clay Sci.* **2005**, *30*, 1–10.

(55) Bargar, J. R.; Reitmeyer, R.; Lenhart, J. J.; Davis, J. A. Characterization of U(VI)-carbonato ternary complexes on hematite: EXAFS and electrophoretic mobility measurements. *Geochim. Cosmochim. Acta* **2000**, *64*, 2737–2749.

(56) Arai, Y.; Moran, P. B.; Honeyman, B. D.; Davis, J. A. In Situ Spectroscopic Evidence for Neptunium(V)-Carbonate Inner-Sphere and Outer-Sphere Ternary Surface Complexes on Hematite Surfaces. *Environ. Sci. Technol.* **2007**, *41*, 3940–3944.

(57) Kirsch, R.; Fellhauer, D.; Altmaier, M.; Neck, V.; Rossberg, A.; Fanghnel, T.; Charlet, L.; Scheinost, A. C. Oxidation State and Local Structure of Plutonium Reacted with Magnetite, Mackinawite, and Chukanovite. *Environ. Sci. Technol.* **2011**, *45*, 7267–7274.

(58) Sverjensky, D. A. Europium redox equilibria in aqueous solution. *Earth Planet. Sci. Lett.* **1984**, *67*, 70–78.

(59) *Multiple bonds between metal atoms*, 3rd ed.; Cotton, F. A., Murillo, C. A., Walton, R. A., Eds.; Springer: 2005.

(60) Schwertmann, U.; Cornell, R. M., *Iron Oxides in the Laboratory: Preparation and Characterization*; VCH: New York, NY, 1991.

(61) Fokkink, L. G. J; Keizer, A de; Lyklema, J Temperature dependence of the electrical double layer on oxides: Rutile and hematite. *J. Colloid Interface Sci.* **1989**, *127*, 116–131.

(62) Noh, J. S.; Schwarz, J. A. Estimation of the point of zero charge of simple oxides by mass titration. *J. Colloid Interface Sci.* **1989**, *130*, 157–164.

(63) Cristiano, E.; Hu, Y.-J.; Siegfried, M.; Kaplan, D.; Nitsche, H. A Comparison of Point of Zero Charge Measurement Methodology., en *Clays Clay Miner.* **2011**, *59*, 107–115.

(64) Herbelin, A.; Westall, J. C. FITEQL. A computer program for the determination of chemical equilibrium constants from experimental data., Corvallis, OR, USA, 1999.

(65) Hiemstra, T; Van Riemsdijk, W. H; Bolt, G. H Multisite proton adsorption modeling at the solid/solution interface of (hydr)oxides: A new approach: I. Model description and evaluation of intrinsic reaction constants. *J. Colloid Interface Sci.* **1989**, *133*, 91–104.

(66) Hiemstra, T.; Van Riemsdijk, W. H. A Surface Structural Approach to Ion Adsorption: The Charge Distribution (CD) Model. *J. Colloid Interface Sci.* **1996**, *179*, 488–508.

(67) Dzombak, D.; Morel, F. M. M., *Surface complexation modeling: Hydrous ferric oxide.* Wiley: New York, NY, 1990.

(68) Wang, Z.; Giammar, D. E. Mass Action Expressions for Bidentate Adsorption in Surface Complexation Modeling: Theory and Practice. *Environ. Sci. Technol.* **2013**, *47*, 3982–3996.

(69) Sverjensky, D. A. Standard states for the activities of mineral surface sites and species. *Geochim. Cosmochim. Acta* **2003**, *67*, 17–28.

(70) Rabung, T.; Geckeis, H.; Kim, J.-I.; Beck, H. P. Sorption of Eu(III) on a Natural Hematite: Application of a Surface Complexation Model. *J. Colloid Interface Sci.* **1998**, *208*, 153–161.

(71) Sverjensky, D. A.; Sahai, N. Theoretical prediction of single-site enthalpies of surface protonation for oxides and silicates in water. *Geochim. Cosmochim. Acta* **1998**, *62*, 3703–3716.

(72) Schlegel, M. L.; Pointeau, I.; Coreau, N.; Reiller, P. Mechanism of Europium Retention by Calcium Silicate Hydrates: An EXAFS Study. *Environ. Sci. Technol.* **2004**, *38*, 4423–4431.

(73) Thompson, A.; Attwood, D.; Gullikson, E.; Howells, M.; Kim, K.-J.; Kirz, J.; Kortright, J.; Lindau, I.; Liu, Y.; Pianetta, P.; Robinson, A.; Scofield, J.; Underwood, J.; Williams, G.; Winick, H., *X-Ray Data Booklet*, Third; Lawrence Berkeley National Laboratory, University of California: Berkeley, CA, Sept. 2009.

(74) Klementev, K. V. Deconvolution problems in X-ray absorption fine structure spectroscopy., en *J. Phys. D: Appl. Phys.* **2001**, *34*, 2241.

(75) Borowski, M.; Bowron, D. T.; De Panfilis, S. High-energy X-ray absorption spectroscopy at ESRF BM29., en *J. Synchrotron Radiat.* **1999**, *6*, 179–181.

(76) Rehr, J. J.; Albers, R. C.; Zabinsky, S. I. High-order multiple-scattering calculations of x-ray-absorption fine structure. *Phys. Rev. Lett.* **1992**, *69*, 3397–3400.

(77) Hanic, F.; Hartmanov, M.; Knab, G. G.; Urusovskaya, A. A.; Bagdasarov, K. S. Real structure of undoped Y_2O_3 single crystals. *Acta Crystallogr.* **1984**, *B40*, 76–82.

(78) Webb, S. M. SIXpack: a graphical user interface for XAS analysis using IFEFFIT., en *Phys. Scr.* **2005**, *2005*, 1011–1014.

(79) Kosmulski, M.; Matysiak, J.; Szczypa, J. Standard enthalpies of proton adsorption on hematite in various solvent systems. *Bull. Pol. Acad. Sci., Chem.* **1993**, *41*, 333–337.

(80) Sverjensky, D. A. Prediction of surface charge on oxides in salt solutions: Revisions for 1:1 (M+L) electrolytes. *Geochim. Cosmochim. Acta* **2005**, *69*, 225–257.

(81) Kosmulski, M. pH-dependent surface charging and points of zero charge: III. Update. *J. Colloid Interface Sci.* **2006**, *298*, 730–741.

(82) Kosmulski, M. Compilation of PZC and IEP of sparingly soluble metal oxides and hydroxides from literature. *Adv. Colloid Interface Sci.* **2009**, *152*, 14–25.

(83) Zeng, H.; Singh, A.; Basak, S.; Ulrich, K.-U.; Sahu, M.; Biswas, P.; Catalano, J. G.; Giammar, D. E. Nanoscale Size Effects on Uranium(VI) Adsorption to Hematite. *Environ. Sci. Technol.* **2009**, *43*, 1373–1378.

(84) In *CRC Handbook of Chemistry and Physics*, Haynes, W. M., Ed., 93rd Edition (Internet Version 2013); CRC Press/Taylor and Francis: Boca Raton, FL, 2013, pp 6–7 –6–8.

(85) Bandura, A. V.; Lvov, S. N. The Ionization Constant of Water over Wide Ranges of Temperature and Density. *J. Phys. Chem. Ref. Data* **2006**, *35*, 15–30.

(86) Ishida, K.; Saito, T.; Aoyagi, N.; Kimura, T.; Nagaishi, R.; Nagasaki, S.; Tanaka, S. Surface speciation of Eu3+ adsorbed on kaolinite by time-resolved laser fluorescence spectroscopy (TRLFS) and parallel factor analysis (PARAFAC). *J. Colloid Interface Sci.* **2012**, *374*, 258–266.

(87) Naveau, A.; Monteil-Rivera, F.; Dumonceau, J.; Boudesocque, S. Sorption of europium on a goethite surface: influence of background electrolyte. *J. Contam. Hydrol.* **2005**, *77*, 1–16.

(88) Kurbatov, M. H.; Wood, G. B.; Kurbatov, J. D. Isothermal Adsorption of Cobalt from Dilute Solutions. *J. Phys. Chem.* **1951**, *55*, 1170–1182.

(89) Waite, T. D.; Davis, J. A.; Payne, T. E.; Waychunas, G. A.; Xu, N. Uranium(VI) adsorption to ferrihydrite: Application of a surface complexation model. *Geochim. Cosmochim. Acta* **1994**, *58*, 5465–5478.

(90) Rojo, I.; Seco, F.; Rovira, M.; Giménez, J.; Cervantes, G.; Martí, V.; Pablo, J. de Thorium sorption onto magnetite and ferrihydrite in acidic conditions. *J. Nucl. Mater.* **2009**, *385*, 474–478.

(91) Dardenne, K.; Schäfer, T.; Denecke, M. A.; Rothe, J.; Kim, J. I. Identification and characterization of sorbed lutetium species on 2-line ferrihydrite by sorption data modeling, TRLFS and EXAFS. *Radiochim. Acta* **2001**, *89*, 469.

(92) Ridley, M. K.; Machesky, M. L.; Wesolowski, D. J.; Palmer, D. A. Surface complexation of neodymium at the rutile-water interface: A potentiometric and modeling study in NaCl media to 250C. *Geochim. Cosmochim. Acta* **2005**, *69*, 63–81.

(93) Ridley, M. K.; Hiemstra, T.; Machesky, M. L.; Wesolowski, D. J.; Riemsdijk, W. H. van Surface speciation of yttrium and neodymium sorbed on rutile: Interpretations using the charge distribution model. *Geochim. Cosmochim. Acta* **2012**, *95*, 227–240.

(94) Zhang, Z. et al. Ion Adsorption at the RutileWater Interface: Linking Molecular and Macroscopic Properties. *Langmuir* **2004**, *20*, 4954–4969.

(95) Allen, P. G.; Bucher, J. J.; Shuh, D. K.; Edelstein, N. M.; Craig, I. Coordination Chemistry of Trivalent Lanthanide and Actinide Ions in Dilute and Concentrated Chloride Solutions. *Inorg. Chem.* **2000**, *39*, 595–601.

(96) Kimura, T.; Kato, Y. Luminescence study on the inner-sphere hydration number of lanthanide(III) ions in concentrated aqueous salt solutions in fluid and frozen states. *J. Alloys Compd.* **1998**, *278*, 92–97.

(97) Marmodée, B.; Jahn, K.; Ariese, F.; Gooijer, C.; Kumke, M. U. Direct Spectroscopic Evidence of 8- and 9-fold Coordinated Europium(III) Species in H_2O and D_2O. *J. Phys. Chem. A* **2010**, *114*, 13050–13054.

(98) In *CRC Handbook of Chemistry and Physics*, Haynes, W. M., Ed., 93rd Edition (Internet Version 2013); CRC Press/Taylor and Francis: Boca Raton, FL, 2013, pp 5–196 –5–198.

(99) Stumpf, T.; Bauer, A.; Coppin, F.; Fanghnel, T.; Kim, J.-I. Inner-sphere, outer-sphere and ternary surface complexes: ATRLFS study of the sorption process of Eu(III) onto smectite and kaolinite. *Radiochim. Acta* **2002**, *90*, 345–349.

(100) Tian, G.; Edelstein, N. M.; Rao, L. Spectroscopic Properties and Hydration of the Cm(III) Aqua Ion from 10 to 85 ℃. *J. Phys. Chem. A* **2011**, *115*, 1933–1938.

(101) Kimura, T.; Nagaishi, R.; Arisaka, M.; Ozaki, T.; Yoshida, Z. Instrumental development for spectroscopic speciation of f-elements in hydrothermal solutions: luminescence properties of lanthanide(III) ions. *Radiochim. Acta* **2002**, *90*, 715–719.

(102) Estes, S. L.; Arai, Y.; Becker, U.; Fernando, S.; Yuan, K.; Ewing, R. C.; Zhang, J.; Shibata, T.; Powell, B. A. A self-consistent model describing the thermodynamics of Eu(III) adsorption onto hematite. *Geochim. Cosmochim. Acta* **2013**, *122*, 430–447.

(103) Gans, P.; Sabatini, A.; Vacca, A. Simultaneous Calculation of Equilibrium Constants and Standard Formation Enthalpies from Calorimetric Data for Systems with Multiple Equilibria in Solution., en *J. Solution Chem.* **2008**, *37*, 467–476.

(104) Freire, E.; Mayorga, O. L.; Straume, M. Isothermal titration calorimetry. *Anal. Chem.* **1990**, *62*, 950A–959A.

(105) Zanonato, P.; Di Bernardo, P.; Bismondo, A.; Liu, G.; Chen, X.; Rao, L. Hydrolysis of Uranium(VI) at Variable Temperatures (10 to 85 ℃). *J. Am. Chem. Soc.* **2004**, *126*, 5515–5522.

(106) Fang, L.; Cai, P.; Li, P.; Wu, H.; Liang, W.; Rong, X.; Chen, W.; Huang, Q. Microcalorimetric and potentiometric titration studies on the adsorption of copper by P. putida and B. thuringiensis and their composites with minerals. *J. Hazard. Mater.* **2010**, *181*, 1031–1038.

(107) Morel, J.-P.; Marmier, N.; Hurel, C.; Morel-Desrosiers, N. Effect of temperature on the acid–base properties of the alumina surface: Microcalorimetry and acid–base titration experiments. *J. Colloid Interface Sci.* **2006**, *298*, 773–779.

(108) Morel, J.-P.; Marmier, N.; Hurel, C.; Morel-Desrosiers, N. Effect of temperature on the sorption of europium on alumina: Microcalorimetry and batch experiments. *J. Colloid Interface Sci.* **2012**, *376*, 196–201.

(109) Martell, A. E.; Smith, R. M.; Motekaitis, R. J. NIST Critically Selected Stability Constants of Metal Complexes., Gaithersburg, MD, USA, 2004.

(110) Dean, R. B.; Dixon, W. J. Simplified Statistics for Small Numbers of Observations. *Anal. Chem.* **1951**, *23*, 636–638.

(111) Rorabacher, D. B. Statistical treatment for rejection of deviant values: critical values of Dixon's "Q" parameter and related subrange ratios at the 95% confidence level. *Anal. Chem.* **1991**, *63*, 139–146.

(112) Hsi, C.-k. D.; Langmuir, D. Adsorption of uranyl onto ferric oxyhydroxides: Application of the surface complexation site-binding model. *Geochim. Cosmochim. Acta* **1985**, *49*, 1931–1941.

(113) Wazne, M.; Korfiatis, G. P.; Meng, X. Carbonate Effects on Hexavalent Uranium Adsorption by Iron Oxyhydroxide. *Environ. Sci. Technol.* **2003**, *37*, 3619–3624.

(114) Hiemstra, T.; Riemsdijk, W. H. V.; Rossberg, A.; Ulrich, K.-U. A surface structural model for ferrihydrite II: Adsorption of uranyl and carbonate. *Geochim. Cosmochim. Acta* **2009**, *73*, 4437–4451.

(115) Dong, W. M.; Brooks, S. C. Determination of the formation constants of ternary complexes of uranyl and carbonate with alkaline earth metals (Mg^{2+}, Ca^{2+}, Sr^{2+}, and Ba^{2+}) using anion exchange method. *Environ. Sci. Technol.* **2006**, *40*, 4689–4695.

(116) Moyes, L. N.; Parkman, R. H.; Charnock, J. M.; Vaughan, D. J.; Livens, F. R.; Hughes, C. R.; Braithwaite, A. Uranium Uptake from Aqueous Solution by Interaction with Goethite, Lepidocrocite, Muscovite, and Mackinawite: An X-ray Absorption Spectroscopy Study. *Environ. Sci. Technol.* **2000**, *34*, 1062–1068.

(117) Rossberg, A.; Ulrich, K.-U.; Weiss, S.; Tsushima, S.; Hiemstra, T.; Scheinost, A. C. Identification of Uranyl Surface Complexes on Ferrihydrite: Advanced EXAFS Data Analysis and CD-MUSIC Modeling. *Environ. Sci. Technol.* **2009**, *43*, 1400–1406.

(118) Reich, T; Moll, H; Arnold, T; Denecke, M. A; Hennig, C; Geipel, G; Bernhard, G; Nitsche, H; Allen, P. G; Bucher, J. J; Edelstein, N. M; Shuh, D. K An EXAFS study of uranium(VI) sorption onto silica gel and ferrihydrite. *J. Electron Spectrosc. Relat. Phenom.* **1998**, *96*, 237–243.

(119) Sherman, D. M.; Peacock, C. L.; Hubbard, C. G. Surface complexation of U(VI) on goethite ($\alpha-$FeOOH). *Geochim. Cosmochim. Acta* **2008**, *72*, 298–310.

(120) Missana, T.; García-Gutiérrez, M.; Maffiotte, C. Experimental and modeling study of the uranium (VI) sorption on goethite. *J. Colloid Interface Sci.* **2003**, *260*, 291–301.

(121) Jang, J.-H.; Dempsey, B. A.; Burgos, W. D. A Model-Based Evaluation of Sorptive Reactivities of Hydrous Ferric Oxide and Hematite for U(VI). *Environ. Sci. Technol.* **2007**, *41*, 4305–4310.

(122) In *CRC Handbook of Chemistry and Physics*, Haynes, W. M., Ed., 95th Edition (Internet Version 2015); CRC Press/Taylor and Francis: Boca Raton, FL, 2014, pp 6–1 –6–4.

(123) Allen, P. G.; Bucher, J. J.; Shuh, D. K.; Edelstein, N. M.; Reich, T. Investigation of Aquo and Chloro Complexes of UO_2^{2+}, NpO_2^+, Np^{4+}, and Pu^{3+} by X-ray Absorption Fine Structure Spectroscopy. *Inorg. Chem.* **1997**, *36*, 4676–4683.

(124) Tsushima, S; Suzuki, A Hydration numbers of pentavalent and hexavalent uranyl, neptunyl, and plutonyl. *J. Mol. Struct.: THEOCHEM* **2000**, *529*, 21–25.

(125) Trivedi, P.; Axe, L. Predicting Divalent Metal Sorption to Hydrous Al, Fe, and Mn Oxides. *Environ. Sci. Technol.* **2001**, *35*, 1779–1784.

(126) Santschi, P. H.; Roberts, K. A.; Guo, L. Organic Nature of Colloidal Actinides Transported in Surface Water Environments. *Environ. Sci. Technol.* **2002**, *36*, 3711–3719.

(127) Clark, D. L.; Hecker, S. S.; Jarvinen, G. D.; Neu, M. P. en In *The Chemistry of the Actinide and Transactinide Elements*, Morss, L. R., Edelstein, N. M., Fuger, J., Eds., 4th; Springer: Dordrecht, The Netherlands, Jan. 2011; Vol. 2, pp 813–1264.

(128) Neu, M. P.; Hoffman, D. C.; Roberts, K. E.; Nitsche, H.; Silva, R. J. Comparison of Chemical Extractions and Laser Photoacoustic Spectroscopy for the Determination of Plutonium Species in Near-Neutral Carbonate Solutions. *Radiochim. Acta* **1994**, *66/67*, 251–258.

(129) Kobashi, A.; Choppin, G.; Morse, J. A study of techniques for separating plutonium in different oxidation states. *Radiochim. Acta* **1988**, *43*, 211–215.

(130) Choppin, G. R.; Rao, L. F. Complexation of Pentavalent and Hexavalent Actinides by Fluoride. *Radiochim. Acta* **1984**, *37*, 143–146.

(131) Teterin, A. Y.; Maslakov, K. I.; Teterin, Y. A.; Kalmykov, S. N.; Ivanov, K. E.; Vukcevic, L.; Khasanova, A. B.; Shcherbina, N. S. Interaction of neptunyl with goethite ($\alpha-FeOOH$), maghemite ($\gamma-Fe_2O_3$), and hematite ($\alpha-Fe_2O_3$) in water as probed by X-ray photoelectron spectroscopy., en *Russ. J. Inorg. Chem.* **2006**, *51*, 1937–1944.

(132) Kohler, M.; Honeyman, B. D.; Leckie, J. O. Neptunium(V) sorption on hematite ($\alpha-Fe_2O_3$) in aqueous suspension: The effect of CO_2. *Radiochim. Acta* **1999**, *85*, 33–48.

(133) Rand, M.; Fuger, J.; Grenthe, I.; Neck, V.; Rai, D., *Chemical Thermodynamics of Thorium*; Mompean, F. J., Perrone, J., Illemassne, M., Eds.; Chemical Thermodynamics, Vol. 11; OECD Nucelar Energy Agency: Issy-les-Moulineaux, France, 2007.

(134) Kersting, A. B. Plutonium Transport in the Environment., en *Inorg. Chem.* **2013**, *52*, 3533–3546.

(135) Clark, D. L.; Hobart, D. E.; Neu, M. P. Actinide carbonate complexes and their importance in actinide environmental chemistry. *Chem. Rev.* **1995**, *95*, 25–48.

(136) Rai, D.; Hess, N. J.; Felmy, A. R.; Moore, D. A.; Yui, M.; Vitorge, P. A thermodynamic model for the solubility of PuO_2 (am) in the aqueous K^+-HCO_3-OH-H_2O system. *Radiochim. Acta* **1999**, *86*, 89–99.

(137) Davis, J. A.; James, R. O.; Leckie, J. O. Surface Ionization and Complexation at the Oxide/Water Interface. I. Computation of Electrical Double-Layer Properties in Simple Electrolytes. *J. Colloid Interface Sci.* **1978**, *63*, 480–499.

(138) Wang, P.; Anderko, A.; Turner, D. R. Thermodynamic Modeling of the Adsorption of Radionuclides on Selected Minerals. I: Cations. *Ind. Eng. Chem. Res.* **2001**, *40*, 4428–4443.

(139) Girvin, D. C.; Ames, L.; Schwab, A. P.; McGarrah, J. E. Neptunium Adsorption on Synthetic Amorphous Iron Oxyhydroxide. *J. Colloid Interface Sci.* **1991**, *141*, 67–78.

(140) Nakayama, S.; Sakamoto, Y. Sorption of Neptunium on Naturally-Occurring Iron-Containing Minerals. *Radiochim. Acta* **1991**, *52/53*, 153–157.

(141) Müller, K.; Foerstendorf, H.; Brendler, V.; Bernhard, G. Sorption of Np(V) onto TiO_2, SiO_2, and ZnO: An in Situ ATR FT-IR Spectroscopic Study. *Environ. Sci. Technol.* **2009**, *43*, 7665–7670.

(142) Gückel, K.; Rossberg, A.; Müller, K.; Brendler, V.; Bernhard, G.; Foerstendorf, H. Spectroscopic Identification of Binary and Ternary Surface Complexes of Np(V) on Gibbsite. *Environ. Sci. Technol.* **2013**, *47*, 14418–14425.

(143) Cromières, L.; Moulin, V.; Fourest, B.; Guillaumont, R.; Giffaut, E. Sorption of Thorium onto Hematite Colloids. *Radiochim. Acta* **1998**, *82*, 249–256.

(144) Murphy, R. J.; Lenhart, J. J.; Honeyman, B. D. The sorption of thorium (IV) and uranium (VI) to hematite in the presence of natural organic matter. *Colloids Surf., A* **1999**, *157*, 47–62.

(145) Jakobsson, A.-M. Measurement and Modeling of Th Sorption onto TiO_2. *J. Colloid Interface Sci.* **1999**, *220*, 367–373.

(146) Östhols, E.; Manceau, A.; Farges, F.; Charlet, L. Adsorption of Thorium on Amorphous Silica: An EXAFS Study. *J. Colloid Interface Sci.* **1997**, *194*, 10–21.

(147) Seco, F.; Hennig, C.; Pablo, J. d.; Rovira, M.; Rojo, I.; Martí, V.; Giménez, J.; Duro, L.; Grivé, M.; Bruno, J. Sorption of Th(IV) onto Iron Corrosion Products: EXAFS Study. *Environ. Sci. Technol.* **2009**, *43*, 2825–2830.

(148) Herr, S. M. Describing Plutonium Contamination Issues in Hanford Soils: Development of a Thermodynamic Surface Complexation Model., Master of Science Thesis, Clemson, SC: Clemson University, 2013.

(149) Nitsche, H.; Edelstein, N. M. Solubilities and speciation of selected trans-uranium ions: A comparison of a non-complexing solution with a groundwater from the Nevada Tuff site. *Radiochim. Acta* **1985**, *39*, 23–33.

(150) Nitsche, H; Lee, S.; Gatti, R. Determination of plutonium oxidation states at trace levels pertinent to nuclear waste disposal. *J. Nucl. Radioanal. Chem.* **1988**, *124*, 171–185.

(151) Banik, N. L.; Buda, R. A.; Brger, S.; Kratz, J. V.; Trautmann, N. Sorption of tetravalent plutonium and humic substances onto kaolinite. *Radiochim. Acta* **2009**, *95*, 569–575.

(152) Choppin, G. R. Utility of Oxidation State Analogs in the Study of Plutonium Behavior. *Radiochim. Acta* **1999**, *85*, 89–95.

(153) Wilson, R. E. Structural Periodicity in Plutonium(IV) Sulfates. *Inorg. Chem.* **2011**, *50*, 5663–5670.

(154) Shannon, R. D. Revised effective ionic radii and systematic studies of interatomic distances in halides and chalcogenides. *Acta Crystallogr.* **1976**, *A32*, 751–767.

(155) Lützenkirchen, J. Ionic Strength Effects on Cation Sorption to Oxides: Macroscopic Observations and Their Significance in Microscopic Interpretation. *J. Colloid Interface Sci.* **1997**, *195*, 149–155.